Doctoral theses at NTNU, 2023:420

Ida Kristine Kure

Interfacial Mass Transfer and Bubble Hydrodynamics in Bubble Columns

Doctoral thesis

NTNU
Norwegian University of Science and Technology
Thesis for the Degree of
Philosophiae Doctor
Faculty of Natural Sciences
Department of Chemical Engineering

NTNU
Norwegian University of
Science and Technology

Ida Kristine Kure

Interfacial Mass Transfer and Bubble Hydrodynamics in Bubble Columns

Thesis for the Degree of Philosophiae Doctor

Trondheim, December 2023

Norwegian University of Science and Technology
Faculty of Natural Sciences
Department of Chemical Engineering

NTNU
Norwegian University of
Science and Technology

NTNU
Norwegian University of Science and Technology

Thesis for the Degree of Philosophiae Doctor

Faculty of Natural Sciences
Department of Chemical Engineering

ISBN 978-82-326-7540-1 (printed ver.)
ISBN 978-82-326-7539-5 (electronic ver.)
ISSN 1503-8181 (printed ver.)
ISSN 2703-8084 (online ver.)

Doctoral theses at NTNU, 2023:420

Printed by NTNU Grafisk senter

Abstract

In processes concerning gas–liquid or gas–liquid–solid interactions, e.g., distillation, absorption, chemical reactors, and bioreactors, the process performance depends on the interfacial mass transfer between the relevant phases. The volumetric mass transfer coefficient, $k_{\mathrm{L}}a$, characterizes the rate of interfacial mass transfer. The quantity of $k_{\mathrm{L}}a$ has significant importance in process design and for the process performance. However, complex physical and mechanical factors contribute to the liquid-side mass transfer coefficient, k_{L}, and the interfacial area, a, and their effects cannot easily be predicted when lumped into $k_{\mathrm{L}}a$. The objective of this dissertation is therefore to enhance the understanding of interfacial mass transfer by examining the individual effects of k_{L} and a.

This dissertation is concerned with the investigation of the interfacial mass transfer phenomena in two experimental facilities. In such, the work is twofold where the first part focuses on the interfacial mass transfer from single bubbles, and the second part focuses on the interfacial mass transfer in bubble swarms. The project involves the design and construction of two experimental facilities, generation of experimental data, and processing and analysis of the experimental data. The first part of this work considers single CO_2 bubbles in the diameter range of $d_{\mathrm{b}} \in [0.7 - 3.0]$ mm, rising in a vertical column containing stagnant deionized water. The design and construction of the experimental facility hold two critical aspects. Firstly, individual bubbles should be generated, and secondly, the experimental facility should be constructed such that it can adapt to the bubble velocity and allow for continuous image recording during the bubble ascent. To fulfill these requirements, several glass needles were constructed for bubble generation, and two high-speed cameras were mounted to a sliding movable platform which was located opposing the bubble column. The mechanical components were operated in LabVIEW by an in-house code written for this project. An image analysis algorithm was developed to extract information on the bubble size, position, and their time derivatives. k_{L} was computed from the data obtained from the recorded images. The results from the single bubble interfacial mass transfer study showed that k_{L} was a function of the initial bubble diameter and bubble–liquid exposure time. A maximum value of k_{L} was obtained for bubbles of size $d_{\mathrm{b}} \in [2.1 - 2.3]$ mm. For bubbles with a mean $d_{\mathrm{b}} \leq 2.8$

mm, the mean k_L decreased with decreasing mean d_b. Here, the mean d_b and k_L were calculated as average values from t=0 to the time k_L attained a steady value. A Lagrangian model description was used with various k_L-correlations to perform numerical simulations of the change in bubble volume during the bubble ascent. The different k_L-correlations gave very different simulations results of the change in bubble volume with time, and the k_L-correlations failed to accurately predict the experimentally obtained change in bubble volume with time.

The second part of this work focuses on the interfacial mass transfer of bubble swarms in liquids exhibiting Newtonian and non-Newtonian rheological behaviour. A vertical rectangular bubble column was constructed, where three different gas spargers were employed for dispersing the gaseous phase as bubbles into the liquid phase. The sparger designs were selected to allow for generation of bubbles with a narrow bubble size distribution, or close to mono-sized bubbles. A high-speed camera allowed for image recording of the bubble swarms in the different liquid solutions (water, glycerol, and Xanthan Gum) and under different operating conditions. The images were processed with an image analysis algorithm using an Artificial Neural Network to determine the bubble size. The effects of liquid rheology, gas flow rate, and sparger design on the interfacial mass transfer and bubble hydrodynamics were analyzed. The results from the work showed that k_L decreased with an increase in the superficial gas velocity and with an increase in the viscosity. The change in k_La was mainly attributed to the change in a. Furthermore, bubble clusters were formed in the non-Newtonian liquids but for the given operating conditions in this study, the bubble cluster formation did not have a prominent effect on the interfacial mass transfer.

Acknowledgements

I would like to thank the Department of Chemical Engineering at NTNU, for the financial grant provided for this research project. A special thanks for the additional financial support that gave me the opportunity to participate in the teaching of the Reactor Technology course and the communication and dissemination group at the department.

I would like to express my sincere gratitude to my supervisor Prof. Jannike Solsvik for the trust and the freedom to organize, structure, and manage this research project. Managing the lab has pushed my limits to places I didn't know existed, and the personal and scientific growth I've experienced over these past years will forever hold great value. Jannike, your determination, knowledge, eagerness, and devotion to science are truly impressive, and have been, and will continue to be, a great inspiration. I would also like to thank my co-supervisor Prof. Hugo A. Jakobsen for contributing with his immense knowledge. Hugo, thank you for all the laughs we have shared, both during my master's and my PhD training.

The single bubble experiments would not have been feasible without the great LabVIEW programming skills of Nicolas La Forgia at the Department of Chemical Engineering and Inge Sandaunet at the Department of Psychics. Nicolas, I will never forget the hours, days, and weeks we spent in the lab engaged in intense discussions, attempts, failures, but ultimately achieving success. A large thanks to Sebastian Bete at the glassblowing workshop at NTNU for making the glass needles, and for the discussions and his engagement to overcome the challenges of producing single bubbles.

I would like to thank my colleagues, especially Sindre, Eirik, Marcin, Mathias, Tore, and Nicolas, for the coffee breaks and the invaluable talks. They have included a lot of laughs and good memories which I will forever remember.

A special thank you goes to my great family and friends. I am fortunate to have such extraordinary individuals in my life. I would like to express my gratitude to Julie, Marie, Oda, Cathrine, and Natasha for their support and care during these years. Lastly, thanks to my mom, dad, bonus-dad Jan Vidar, and Anders for being my pillars of love and providing safety and unwavering support.

List of Publications and Presentations

Publications in Journals

Paper I I. Kure, H. A. Jakobsen, N. L. Forgia, J. Solsvik, Experimental investigation of single bubbles rising in stagnant liquid: Statistical analysis and image processing, Physics of Fluids 33, 103611 (2021)
https://doi.org/10.1063/5.0061581

CRediT: **Kure, I. K.**: Conceptualization, Data curation, Formal analysis, Investigation, Methodology, Software, Writing – original draft. **Solsvik, J.** Conceptualization, Supervision, Writing – review & editing. **Jakobsen, H. A.** Conceptualization, Supervision, Writing – review & editing. **La Forgia, N.** Software.

Paper II I. Kure, H. A. Jakobsen, J. Solsvik, Experimental Study of Interfacial Mass Transfer from Single CO_2 Bubbles Ascending in Stagnant Water.
Submitted for review in Chemical Engineering Science.

CRediT: **Kure, I. K.**: Conceptualization, Data curation, Formal analysis, Investigation, Methodology, Software, Writing – original draft. **Solsvik, J.** Conceptualization, Supervision, Writing – review & editing. **Jakobsen, H. A.** Conceptualization, Supervision, Writing – review & editing

Paper III I. Kure, H. A. Jakobsen, J. Solsvik, Interface mass transfer and properties of bubbly flows in a column with Newtonian and non-Newtonian liquids, Chemical Engineering Science 277 (2023) 118828
https://doi.org/10.1016/j.ces.2023.118828

CRediT: **Kure, I. K.**: Conceptualization, Data curation, Formal analysis, Investigation, Methodology, Software, Writing – original draft. **Solsvik, J.** Conceptualization, Supervision, Writing – review & editing. **Jakobsen, H. A.** Conceptualization, Supervision, Writing – review & editing.

Presentations at Conferences

Key Note Presentation Kure. I. K., Bioreactor technology and plant design for meat production. 4th International Scientific Conference on Cultured Meat, Maastricht, Nederland, December 2–4, 2018.

Presentation Kure, I. K., Jakobsen, H. A., Solsvik, J., Experimental investigation of a single bubble rising in a stagnant liquid, 24th International Congress of Chemical and Process Engineering CHISA, Prague, Czech Republic, Virtual conference, March 15–18, 2021.

Contents

Nomenclature

The following nomenclature applies to the chapters of this thesis. In the attached papers, the nomenclature may be differing, but it is clearly defined therein.

Abbreviations

ANN	artificial neural network
DO	dissolved oxygen

Greek letters

δ	film thickness, [m]
$\dot{\gamma}$	shear rate, [1/s]
η	apparent viscosity, [Pa·s]
λ	fitting parameter, [-]
μ	dynamic viscosity, [Pa·s]
ϕ	generalized function
τ	shear stress, [Pa]
$\tau^{'}$	average exposure time of fluid element, [s]

Latin letters

ΔV	electric potential, [V]
a	interfacial area per unit volume, [m^{-1}]
C	concentration, [mol/m^3]
D	diffusion coefficient, [m^2/s]
d	diameter, [m]
H	Henry's constant, different units
I	current, [A]
J	mass transferred by diffusion, [$mol/(m^2s)$]

K	overall mass transfer coefficient, [m/s]
k	mass transfer coefficient, [m/s]
N	rate of mass transfer, [mol/(m^{3}s)]
N'	mass flux, [mol/(m^{2}s)]
R	resistance to mass transfer, [s]
s	rate of surface renewal, [1/s]
t	time, [s]
z	axial direction, [m]
Eo	Eötvos number
Ga	Galilei number
Gr	Grashof number
Re	Reynolds number
Sc	Schmidt number
Sh	Sherwood number

Superscripts

$*$	concentrations with Henry's constant
b	fitting parameter
m	fluid consistency index
n	flow behavior index

Subscripts

∞	infinite shear rate viscosity
0	zero shear rate viscosity
B	bulk
b	bubble
e	exposure
G	gas phase

I	interface
i	component
L	liquid phase

Chapter 1

Introduction

1.1 Background

The average global temperatures on Earth have increased by 1.2°C since 1880, and most of the warming has particularly occurred in the late 20th century (United Nations, 2023). Reports by the Intergovernmental Panel on Climate Change (IPCC) steadily points out the disturbing effects of human activities on the warming of the atmosphere, ocean, and land (Intergovernmental Panel on Climate Change, 2023). To enable adaptive responses to climate change, the Sustainable Development Goals (United Nations, 2023), the global call of action to achieve sustainability and resilience for both the humanity and the planet, are closely linked with climate (United Nations, 2023). This dissertation can be considered relevant for several of the sustainability goals, as increased understanding of the phenomena of interfacial mass transfer is crucial for process design and optimization, which is important for continued development of circular economy and a sustainable process industry.

The interaction between gas–liquid or gas–liquid–solid phases exhibit complexity which for years have lead researchers to study the intrinsic mechanisms involved. One important branch within multi-phase flow is the interfacial mass transfer which takes place between the relevant phases. A variety of industrial processes depend on the interfacial mass transfer between gas bubbles and the liquid phase in which the bubbles are dispersed. Relevant processes include distillation, absorption, fermentation, sewage treatment, chemical reactors, and bioreactors. The performance of these processes depends on the rate of interfacial mass transfer, which is characterized by the volumetric mass transfer coefficient, $k_{\mathrm{L}}a$. There are many parameters which may influence $k_{\mathrm{L}}a$; bubble size, bubble hydrodynamics, gas flow rate, temperature, and liquid properties, e.g., viscosity and surface tension. Interfacial mass transfer phenomena have commonly been investigated by studying $k_{\mathrm{L}}a$ in bubble swarms (Akita and Yoshida, 1973; Vandu et al., 2004; Scargiali et al., 2010; Muroyama et al., 2013; Zednikova et al., 2018). Complex physical and mechanical

factors contribute to both the liquid-side mass transfer coefficient, k_L, and the interfacial area, a, and k_La measurements are not sufficient to comprehend the involved mechanisms. Studying the individual contributions of k_L and a on k_La can therefore provide valuable information which is necessary for optimal process performance.

With increased focus on climate and sustainability, the field of biochemical engineering is receiving more attention. In bioprocesses such as fermentation, the viscosity of the fermentation fluids is affected by the presence of cells, substrate, and product concentrations (Doran, 2013). A variety of fermentation processes therefore involve highly viscous liquids and liquids which possess non-Newtonian rheological behavior (Badino et al., 1976; Blanch and Bhavaraju, 1976). The bubble hydrodynamics and the interfacial mass transfer are affected by the liquid rheology, which can led to reduced process performance. k_L and a are mainly studied in Newtonian liquids (Vasconcelos et al., 2003; Sastaravet et al., 2020; Bouaifi et al., 2001), and there are limited studies on k_L and a in non-Newtonian liquids (Augier and Raimundo, 2021). Furthermore, formation of bubble clusters is observed in fluids represented in the bioprocess industry (Vélez-Cordero and Zenit, 2011; Vélez-Cordero et al., 2012). The existing literature on bubble clusters mainly focuses on the formation and velocity of the bubble clusters (Vélez-Cordero and Zenit, 2011). To further increase the understanding of bubble clusters, it is of interest to establish knowledge on the interfacial mass transfer from bubble cluster.

The splitting of k_La into k_L and a requires data on the bubble size and gas hold-up, which are not as readily available as the quantity of k_La. An alternative approach to bubble swarms is to study a single bubble in either a stagnant liquid (Baird and Davidson, 1962; Bischof et al., 1991; Deindoerfer and Humphrey, 1961; Calderbank and Lochiel, 1964; Zieminski and Raymond, 1968; Hosoda et al., 2014; Aoki et al., 2015), or in a counter-current flow (Hosoda et al., 2014; Vasconcelos et al., 2002; Olsen et al., 2017). For a single bubble rising in stagnant liquid, the bubble size and position can be monitored during the bubble ascent by, e.g., image acquisition, and the acquired data can be used to compute k_L and a. The study of individual bubbles serves as foundation for the study of bubble swarms.

1.2 Research Objectives

The main goal of this dissertation is to elucidate the phenomena of interfacial mass transfer. The interfacial mass transfer and the bubble hydrodynamics are experimentally studied for single bubbles and in bubble swarms in two bubble columns.

Investigating k_L and a is emphasized to enhance the understanding of the interfacial mass transfer phenomena. From the experimentally obtained data, the effects of bubble size, bubble velocity, bubble trajectory, liquid rheology, gas flow rate, and sparger design on the interfacial mass transfer are investigated. The following sub-objectives are required to achieve the outlined main goal:

Single bubble experiments:

- Investigate the interfacial mass transfer from a single bubble rising in stagnant water by designing and constructing an experimental facility. Install high-speed cameras on a sliding movable platform to allow for continuous recording of the transient evolution of the bubble as it ascends through the bubble column and exposes to the interfacial mass transfer phenomena and hydrostatic pressure gradient. Construct glass needles with different inner diameters to enable production of bubbles within a range of initial bubble sizes. Develop an algorithm to control the system components, including a glass needle connected to a syringe pump, a sliding movable platform, and two high-speed cameras. The algorithm should enable the sliding movable platform to adapt to the transient bubble velocity. Establish a procedure for preparing the liquid phase such that the dissolved gas concentration is negligible and reproducible

- Extract information from the recorded images on the bubble size, position, trajectory, and velocity by developing an image analysis algorithm. Process the images by using the image analysis algorithm, and analyze the processed data to elucidate the interfacial mass transfer phenomena.

Bubble swarm experiments:

- Investigate the effects of liquid rheology and operating conditions on the interfacial mass transfer in bubble swarms by designing and constructing an experimental facility. The design of the experimental facility should allow for image recording of the bubbles by a high-speed camera. Construct gas spargers (based on the original design in the work by Vélez-Cordero and Zenit (2011)) that allow for generation of bubbles with a narrow bubble size distribution or close to mono-sized bubbles. Choose liquid solutions with the properties of low and high viscous Newtonian and non-Newtonian rheological behavior, with the purpose of examining liquids commonly found in the process industry. Establish a procedure for preparing the liquid solutions such that the liquid properties are reproducible. Select a method for measuring the interfacial mass

transfer in bubble swarms.

- Extract information on the bubble sizes of multiple bubbles in low and high viscous Newtonian liquids, as well as liquids exhibiting non-Newtonian rheological behavior by developing a procedure for processing the recorded images. The procedure should enable determination of a mean bubble size, calculated from a narrow bubble size distribution to increase the statistical accuracy. Conduct experiments with different sparger designs, flow conditions, and liquid solutions, to elucidate the interfacial mass transfer phenomena in bubble swarms.

1.3 Dissertation Outline

The dissertation is organized into four chapters. Chapter 2 provides an introduction to the phenomena of interfacial mass transfer. Different experimental set-ups used in interfacial mass transfer studies on single bubbles and bubble swarms are outlined in chapter 3. In chapter 4, the published papers and the results from the dissertation are presented. Paper I establishes an experimental facility with the ability to continuously track and acquire images of a single bubble during its ascent in a vertical bubble column containing stagnant liquid. The design and technical details on the automatization of the experimental facility, including the control system and processing of the data, are covered. Paper II focuses on the interfacial mass transfer from single bubbles rising in stagnant liquid. The interfacial mass transfer study is carried out in the experimental facility established in Paper I. The changes in bubble size and velocity due to the interfacial mass transfer are determined by the photographic method using a high-speed camera. Paper III investigates the interfacial mass transfer phenomena in bubble swarms in a vertical bubble column containing Newtonian and non-Newtonian liquids. The interfacial mass transfer is measured by the dynamic method. The bubbles are recorded by a high-speed camera, and the bubble sizes are calculated by an image analysis algorithm using an artificial neural network (ANN). Finally, concluding remarks and suggestions for further work are given in chapter 5.

Chapter 2

Interfacial Mass Transfer Phenomena

Diffusion is the movement of molecules and ions from regions with high concentrations to regions with low concentrations. The process can be described with Fick's law and a diffusion coefficient, or it can be described in terms of a mass transfer coefficient (Cussler, 1997). In this dissertation, the description using a mass transfer coefficient is selected. Although diffusion can be described in terms of a mass transfer coefficient, the scenario of solely diffusive contributions to the mass transfer flux is a highly idealized case (Cussler, 1997), and a variety of mass transfer coefficient correlations therefore include both diffusive and convective contributions. To understand the importance of the mass transfer coefficient, one should start out with understanding the fundamental theory of interfacial mass transfer taking place between two phases. Furthermore, this section presents theories of interfacial mass transfer mechanisms which consider diffusive and convective contributions to the mass transfer coefficient.

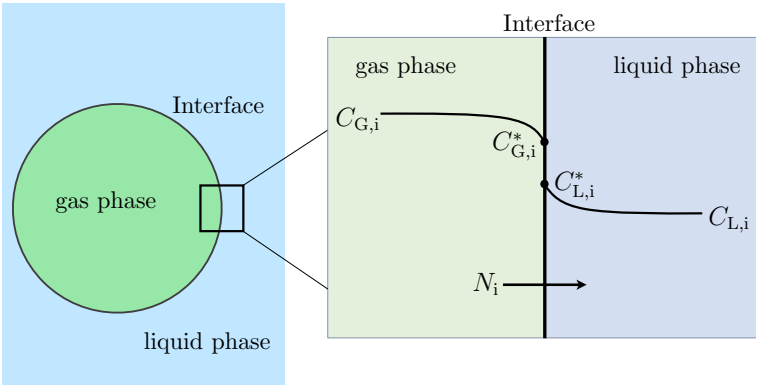

Figure 2.1: An illustration of the phenomena of interfacial mass transfer.

Interfacial mass transfer includes the transfer of a component i over an interface which separates the two phases. Figure 2.1 illustrates a gas phase in contact

with a liquid phase which are separated by a gas–liquid interface. In general, the driving force for transfer of a component i over an interface may rise from one or several of the following non-equilibrium phenomena; concentrations gradients, pressure gradients, thermal gradients, or external forces (Jakobsen, 2014). In figure 2.1, the driving force for mass transfer is the concentration difference of component i between the two phases, which can be written as:

$$\Delta C_{\mathrm{i}} = C_{\mathrm{G,i}} - C_{\mathrm{L,i}} \tag{2.1}$$

where $C_{\mathrm{G,i}}$ and $C_{\mathrm{L,i}}$ denote the molar based concentration of component i in the bulk of the gas and liquid phase, respectively. The definition of interfacial mass transfer is based on empirical arguments (Cussler, 1997), and for the gas in contact with the liquid in figure 2.1 $C_{\mathrm{G,i}} > C_{\mathrm{L,i}}$ resulting in component i being transferred out of the gas phase into the liquid phase with a mass flux, $N_{\mathrm{i}}^{'}$:

$$N_{\mathrm{i}}^{'} = K_{\mathrm{i}}(C_{\mathrm{G,i}} - C_{\mathrm{L,i}}) \tag{2.2}$$

where K_{i} denotes the overall mass transfer coefficient of component i. Determining the mass transfer coefficient has been attempted through various theories which are based on different hydrodynamic phenomena with varying complexity; the one and two-film theories (Whitmand and Keats, 1922), the penetration theory (Higbie, 1935), the surface renewal theory (Danckwerts, 1951), and the laminar and turbulent boundary layer theories (see e.g., Bird et al. (1960) for the boundary layer theories). The two-film theory, the penetration theory, and the surface renewal theory are presented in the following subsections.

Two-Film Theory

In the two-film theory, illustrated in figure 2.2, it is assumed that two stagnant films exist on the liquid and gas side of the interface, respectively. It is further assumed that all the resistance to mass transfer resides in the liquid and gas film of thickness δ_{L} and δ_{G}, respectively. In analogy with Ohm's law ($I \cdot R = \Delta V$, where I is the current and ΔV the electric potential), the resistance to mass transfer, R, can be defined as (Stamatiou and Muller, 2019; Doran, 2013)

$$R = \frac{\Delta C_{\mathrm{i}}}{N_{\mathrm{i}}} \tag{2.3}$$

where N_i denotes the rate of mass transfer of component i. The bulk phases are assumed to be perfectly mixed and concentration gradients occur only over the films. The mass transfer flux is described as a steady diffusion flux where thermodynamic equilibrium is assumed to prevail at the interface.

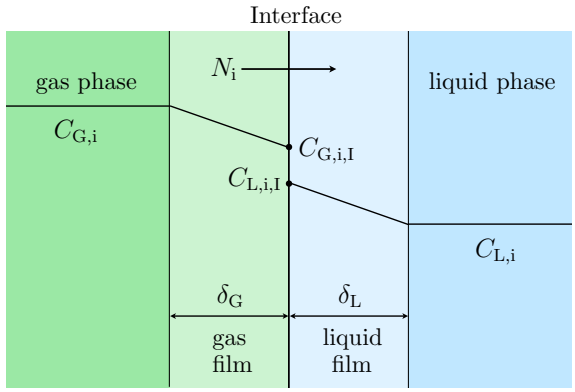

Figure 2.2: An illustration of the two-film model.

For the scenario with a steady diffusive mass transfer flux across a stagnant film, the species mole balance is

$$-\frac{\mathrm{d}J_\mathrm{i}}{\mathrm{d}z} = 0 \tag{2.4}$$

where J_i denotes the mass transferred by diffusion and z the axial direction perpendicular to the interface. Fick's law (Fick, 1855) for binary diffusion is given by

$$J_\mathrm{i} = -D_\mathrm{i}\frac{\mathrm{d}C_\mathrm{i}}{\mathrm{d}z} \tag{2.5}$$

where D_i denotes the diffusion coefficient of component i. Inserting equation (2.5) into equation (2.4) yields

$$-D_\mathrm{i}\frac{\mathrm{d}^2C_\mathrm{i}}{\mathrm{d}z^2} = 0 \tag{2.6}$$

Equation (2.6) can be solved with the boundary conditions:

$$C_\mathrm{i} = C_{\mathrm{i,B}},\ z = 0 \tag{2.7}$$

$$C_\mathrm{i} = C_{\mathrm{i,I}},\ z = \delta \tag{2.8}$$

where the subscripts B and I denote the bulk phase and the interface, respectively. Integrating equation (2.6) and using the appropriate boundary conditions in equa-

tions (2.7) and (2.8) give

$$C_{\mathrm{i}} = C_{\mathrm{i,B}} + \frac{1}{\delta}(C_{\mathrm{i,I}} - C_{\mathrm{i,B}})z \tag{2.9}$$

The diffusive flux can be found by inserting equation (2.9) into equation (2.5):

$$J_{\mathrm{i}} = -D_{\mathrm{i}}\frac{\mathrm{d}C_{\mathrm{i}}}{\mathrm{d}z} = \frac{D_{\mathrm{i}}}{\delta}(C_{\mathrm{i,B}} - C_{\mathrm{i,I}}) \tag{2.10}$$

An expression for the mass transfer coefficient can be obtained by comparing the diffusive flux in equation (2.10) with equation (2.2):

$$k_{\mathrm{i}} = \frac{D_{\mathrm{i}}}{\delta} \tag{2.11}$$

Sherwood number, Sh, includes the mass transfer coefficient and determines the ratio between the mass transfer and diffusion rates (Jakobsen, 2014):

$$\mathrm{Sh} = \frac{k_{\mathrm{i}}\delta}{D_{\mathrm{i}}} \tag{2.12}$$

In mass transfer problems, the Sherwood number is commonly expressed in terms of dimensionless groups such as the Reynolds number (Re) and Schmidt number (Sc); Sh = ϕ(Re, Sc), the Galilei number (Ga) and Schmidt number; Sh = ϕ(Ga, Sc), or the Grashof number (Gr) and Schmidt number; Sh = ϕ(Gr, Sc) (see table 2.1). From equations (2.11) and (2.12) it follows that based on the two-film theory, Sh = 1. In a system where the transport of mass arises due to both diffusive and convective contributions, Sh $\neq$ 1, and equation (2.11) cannot be used to compute the mass transfer coefficient.

Penetration Theory

Attempting to more accurately describe the physical phenomena involved during interfacial mass transfer, Higbie (1935) formulated the penetration theory. Figure 2.3 illustrates the penetration theory where the liquid phase consists of small fluid elements which are transported to the interface by the turbulent properties of the flow. A fluid element arriving at the interface exchanges mass with the gas phase due to diffusion for a fixed time before it is transported from the interface to the liquid bulk. Subsequently, a new fluid element is transported to the interface and mass is exchanged. The interface exposure time is assumed equal for all the fluid elements and the total mass transfer is obtained by integrating over the exposure

time. The bulk phases are assumed to be perfectly mixed. Based on the penetration theory, the mass transfer coefficient and the diffusion coefficient can be related as (Jakobsen, 2014)

$$k_{\mathrm{i}} = 2\sqrt{\frac{D_{\mathrm{i}}}{\pi t_{\mathrm{e}}}} \tag{2.13}$$

where t_{e} denotes the exposure time of the fluid element which is a fitting parameter into which the details of the fluid dynamics are lumped (Jakobsen, 2014).

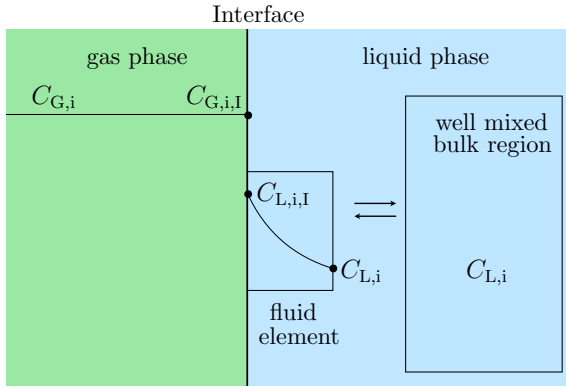

Figure 2.3: An illustration of the penetration theory.

Surface Renewal Model

To further improve the penetration theory, Danckwerts (1951) formulated the surface renewal model where the constant exposure time was replaced with an average exposure time, $\tau^{'}$, obtained from an exposure time distribution. The mass transfer coefficient based on the surface renewal model can be expressed as (Jakobsen, 2014)

$$k_{\mathrm{i}} = \sqrt{\frac{D_{\mathrm{i}}}{\tau^{'}}} = \sqrt{D_{\mathrm{i}} s} \tag{2.14}$$

where $s = 1/\tau^{'}$ is the rate of surface renewal. From equation (2.14) it is seen that despite the attempt of Danckwerts (1951) to improve the physical description of the interfacial mass transfer, the mass transfer coefficient still holds the same dependency of the diffusion coefficient. The laminar and turbulent boundary theories are other rigorous models which attempt to improve the hydrodynamic characteristics of the interfacial mass transfer phenomena. Table 2.1 provides correlations for k_{L} which are empirical correlations or based on the presented theories.

Table 2.1: Correlations for k_L. The correlations are implemented in a Lagrangian model (described by Solsvik (2018)) in Paper II to simulate the change in bubble volume with time.

Reference	k_L	Range d_b
Higbie (1935)	$2\pi^{-1/2}\mathrm{Re_b}^{1/2}\mathrm{Sc}^{1/2}(D/d_b)$	
Fröessling (1938)	$0.6\mathrm{Re_b}^{1/2}\mathrm{Sc}^{1/3}(D/d_b)$	
Calderbank and Moo-Young (1961)	$0.31\mathrm{Gr}^{1/3}\mathrm{Sc}^{1/3}(D/d_b)$	$d_b < 2.5$ mm
Calderbank and Moo-Young (1961)	$0.42\mathrm{Gr}^{1/3}\mathrm{Sc}^{1/2}(D/d_b)$	$d_b > 2.5$ mm
Baird and Davidson (1962)	$0.975\mathrm{Ga}^{1/4}\mathrm{Sc}^{1/2}(D/d_b)$	8 mm $< d_b <$ 42 mm
Garner and Suckling (1958)	$(2+0.95\mathrm{Re_b}^{1/2}\mathrm{Sc}^{1/3})(D/d_b)$	
Clift et al. (1978)	$0.45\mathrm{Gr}^{0.3}\mathrm{Sc}^{1/3}(D/d_b)$	$d_b > 0.1$ mm
Brauer (1979)	$(2+0.015\mathrm{Re_b}^{0.89}\mathrm{Sc}^{0.7})(D/d_b)$	
Bird et al. (1960)	$(4+1.21\mathrm{Re_b}^{2/3}\mathrm{Sc}^{2/3})^{1/2}(D/d_b)$	
Clift et al. (1978), modified in Olsen et al. (2017)	$2\pi^{-1/2}(1-2.89/\max[2.89,\sqrt{\mathrm{Re_b}}])^{1/2}\mathrm{Re_b}^{1/2}\mathrm{Sc}^{1/2}(D/d_b)$	

The rate of mass transfer of component i from the gas-phase bulk to the interface, $N_{G,i}$, and from the interface to the liquid-phase bulk, $N_{L,i}$, can be expressed by equations (2.15) and (2.16):

$$N_{G,i} = k_{G,i}a(C_{G,i} - C_{G,i,I}) \tag{2.15}$$

$$N_{L,i} = k_{L,i}a(C_{L,i,I} - C_{L,i}) \tag{2.16}$$

where $k_{G,i}$ and $k_{L,i}$ denote the gas and liquid-side mass transfer coefficient of component i, respectively, and $C_{G,i,I}$ and $C_{L,i,I}$ the concentrations of component i at the interface. According to the definition of mass transfer resistance in equation (2.3), the resistances to mass transfer in equations (2.15) and (2.16) are $1/(k_{G,i}a)$ and $1/(k_{L,i}a)$, respectively. It is assumed that there is no accumulation of mass at the interface, i.e., $N_{G,i} = N_{L,i} = N_i$, and that gas–liquid equilibrium prevails at the interface, i.e., $C_{G,i,I} = H_i C_{L,i,I}$, where H_i is the Henry's constant of component i. Substituting $C_{G,i,I} = H_i C_{L,i,I}$ into equations (2.15) and (2.16) yield

$$N_i = k_{G,i}a(C_{G,i} - H_i C_{L,i,I}) \tag{2.17}$$

$$N_i = k_{L,i}a\Big(\frac{C_{G,i,I}}{H_i} - C_{L,i}\Big) \tag{2.18}$$

Equation (2.16) is multiplied by H_i and the result is substituted into equation (2.17), leading to:

$$N_i = K_{G,i}a(C_{G,i} - H_i C_{L,i}) \tag{2.19}$$

where the overall mass transfer coefficient, $K_{G,i}$, is defined as $1/(K_{G,i}a) = 1/(k_{G,i}a) + H_i/(k_{L,i}a)$. Equation (2.15) is multiplied by $1/H_i$ and the result is substituted into

equation (2.18), which gives:

$$N_{\mathrm{i}} = K_{\mathrm{L,i}}a\Big(\frac{C_{\mathrm{G,i}}}{H_{\mathrm{i}}} - C_{\mathrm{L,i}}\Big) \tag{2.20}$$

where the overall mass transfer coefficient, $K_{\mathrm{L,i}}$, is defined as $1/(K_{\mathrm{L,i}}a) = 1/(H_{\mathrm{i}}k_{\mathrm{G,i}}a) + 1/(k_{\mathrm{L,i}}a)$. A conventional notation is to denote $H_{\mathrm{i}}C_{\mathrm{L,i}}$ in equation (2.19) by $C^*_{\mathrm{G,i}}$, and let $C_{\mathrm{G,i}}/H_{\mathrm{i}}$ in equation (2.20) be denoted by $C^*_{\mathrm{L,i}}$. The resistance to mass transfer occurs on both sides of the interface and expressions for the mass transfer coefficient for both phases should be derived. However, for the case where a component i is poorly soluble in the liquid phase, the main resistance to mass transfer resides on the liquid side, i.e., $k_{\mathrm{G,i}}a >> k_{\mathrm{L,i}}a$. Thus, $K_{\mathrm{L,i}}a$ can be approximated by $k_{\mathrm{L,i}}a$, and the following expression can be used for the rate of mass transfer:

$$N_{\mathrm{i}} = k_{\mathrm{L,i}}a(C^*_{\mathrm{L,i}} - C_{\mathrm{L,i}}) \tag{2.21}$$

If a component i is highly soluble in the liquid phase, the main resistance to mass transfer is on the gas side, i.e., $k_{\mathrm{L,i}}a >> k_{\mathrm{G,i}}a$. Thus, $K_{\mathrm{G,i}}a$ can be approximated by $k_{\mathrm{G,i}}a$, and the rate of mass transfer can be expressed as

$$N_{\mathrm{i}} = k_{\mathrm{G,i}}a(C_{\mathrm{G,i}} - C^*_{\mathrm{G,i}}) \tag{2.22}$$

In this dissertation, it is assumed that the main resistance to mass transfer resides on the liquid side, and the rate of mass transfer is therefore expressed according to equation (2.21). When a is known, an expression for k_{L} is necessary to compute N_{i} from equation (2.21). k_{L} cannot be calculated reliably by first principles as the hydrodynamics of most practical systems are not easily characterized (Doran, 2013). k_{L} is therefore either computed based on correlations or experimentally determined. In Paper II, an expression for k_{L} is derived in a Lagrangian framework allowing for computation of k_{L} from the experimentally measured quantities (review Paper II for the complete derivation). Furthermore, the k_{L}-correlations in table 2.1 are implemented in a Lagrangian model (described by Solsvik (2018)) to simulate the change in bubble volume with respect to time. The simulation results of the change in bubble volume with respect to time using the k_{L}-correlations in table 2.1 are compared to the simulation results of the change in bubble volume with time using the k_{L}-correlation derived in the Lagrangian framework (computed from the experimentally obtained data).

Chapter 3

Experimental Set-Ups, Measurement Methods, and Fluid Rheology

The interfacial mass transfer phenomena are studied in a variety of experimental apparatuses, including common contactors such as the stirred tank (Bouaifi and Roustan, 1998; Bouaifi et al., 2001; Alves et al., 2004; Linek et al., 2005; Cappello et al., 2020; Ali and Solsvik, 2020, 2021) and the bubble column (Bouaifi et al., 2001; Linek et al., 2005; Zednikova et al., 2018; Sastaravet et al., 2020; Augier and Raimundo, 2021; Kure et al., 2023). The contactors hold different desirable features and are commonly selected based on the system of consideration, e.g., for a system including microbial cells sensitive to shear, a bubble column might be favorable over a stirred tank due to the mechanical parts of the latter contactor. The bubble column (or the bubble column reactor for reaction processes) is widely used in gas–liquid industrial processes and is in its simplest form a vertical column with a gas distributor at the inlet (Jakobsen, 2014). The simple construction and lack of operational parts characterize the bubble column. In this dissertation, the interfacial mass transfer phenomena are investigated for single bubbles and in bubble swarms in two bubble columns. The section therefore presents common methods for measuring the interfacial mass transfer from single bubbles and from bubble swarms in bubble columns. Furthermore, the section provides an overview of commonly used sparger designs for dispersing the gaseous phase as bubbles into the liquid phase. A brief introduction to fluid rheology is given to provide a basic understanding of the rheological behavior of the different liquid solutions considered in this dissertation.

3.1 Interfacial mass Transfer from Single Bubbles

In single bubble interfacial mass transfer studies, two experimental approaches are commonly used; (i) a bubble rising in stagnant liquid (Deindoerfer and Humphrey,

1961; Calderbank and Lochiel, 1964; Koide et al., 1985; Motarjemi and Jameson, 1978; Zieminski and Raymond, 1968; Merker et al., 2017), or (ii) a bubble released in a counter-current liquid flow and kept stationary by balancing the forces acting upon it (Alves et al., 2006; Vasconcelos et al., 2002; Hosoda et al., 2014; Olsen et al., 2017). The counter-current liquid flow approach is favorable when the interfacial mass transfer is slow, and the bubble should be examined over a long time frame. The stagnant liquid approach is emphasized in this section for its relevance to the work in Paper II.

The investigation of interfacial mass transfer between a single bubble and the surrounding liquid requires an experimental facility with the ability to generate a single bubble and measure the interfacial mass transfer as the bubble ascends through the column. The device used for bubble generation is crucial for several reasons: (i) the bubble generation device should enable production of single bubbles with similar size as the interfacial mass transfer, bubble velocity, and bubble trajectory are highly depending on the initial bubble size, and (ii) if two or more bubbles are generated at once then the entailing bubble(s) may interfere and affect the interfacial mass transfer. Figure 3.1 shows three commonly used devices for bubble generation. A needle, capillary, or an orifice have been used in a number of single bubble studies (Leonard and Houghton, 1963; Garbarini and Tien, 1969; Kure et al., 2021; Nock et al., 2015; Merker et al., 2017). Here, a bubble is formed by, e.g., filling a syringe with gas, after which the gas is transferred to the bubble generation device through tubes by using a pump (Merker et al., 2017; Kure et al., 2021). Despite the apparently simple design of a needle, its construction should be given attention as it is challenging to produce individual bubbles with equal size and to avoid formation of gas jets. Another device is the rotating cup (Baird and Davidson, 1962; Hori et al., 2017; Aoki et al., 2015), where gas is injected underneath a cup and then rotated to release the bubble. With this device an approximately fixed bubble size can be obtained by quickly rotating the cup. However, a drawback with this approach in interfacial mass transfer studies is the exposure of the gas phase to the liquid phase prior to the rotation of the cup and the release of the bubble. This may highly influence the measured initial bubble size and interfacial mass transfer.

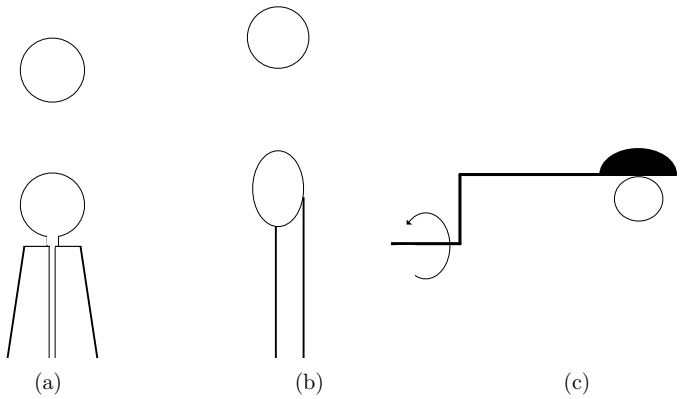

Figure 3.1: Illustration of bubble generation devices: (a) needle, (b) capillary, and (c) rotating cup. The bubble generation device shown in (a) is employed in Paper I and II.

For the approach of a single bubble rising in stagnant liquid, the interfacial mass transfer is commonly measured based on four techniques; the photographic method, the pressure based technique, the concentration based method, and the laser-induced florescence method. In the photographic method, information on the change in bubble size and position is acquired by, e.g., a high-speed camera, as the bubble ascends through the column. The recorded images can then be used for computation of k_{L} from the measured quantities of bubble volume, surface area, vertical position in the bubble column, velocity, and their time derivatives. For two-dimensional image recording of larger bubbles, the accuracy of the data may be reduced due to large surface oscillations and thus fluctuations in the projected area (Bao et al., 2020).

In the pressure based technique, the interfacial mass transfer can be measured from the pressure difference between the bubble releasing point and the liquid free surface (Calderbank and Lochiel, 1964; Garbarini and Tien, 1969). This method is however restricted to bubbles with diameter > 6 mm as the pressure change will not be observable for smaller bubbles, and the increased liquid turbulence may lead to fluctuations of the measurements (Bao et al., 2020).

Gas chromatography can be used as a concentration based technique to determine the change in gas mixture composition in the bubble column (Bischof et al., 1991). Here, a sample of gas bubbles of known size is collected in a diver located in the top of the bubble column. The sample, which should contain a high number of bubbles to obtain statistical significance and to obtain a sufficient gas sample volume, is then analyzed in a gas chromatograph (Bischof et al., 1991).

Another approach is the laser-induced florescence method, where the concentration field around the bubble surface is measured using a laser imaging technique (Kong et al., 2018; Francois et al., 2011; Saito and Toriu, 2015). It includes absorption of a laser photon followed by emission of a fluorescence photon from the excited state (LaVision, 2023). Specific florescence is chosen depending on the gas and liquid properties. This method has strict requirements for the florescence and laser source, e.g., the laser may disturb bubble visualization due to high luminous intensity and bubble surface reflection, and some florescence may act as surfactants and thus influence the interfacial mass transfer (Bao et al., 2020). The photographic method using a high-speed camera is employed in the work in Paper I and II.

3.2 Interfacial Mass Transfer from Bubble Swarms

For bubble swarms in a bubble column, the gas phase is dispersed as bubbles into the liquid phase by a gas distributor, usually located at the inlet of the column. The design of the gas distributor vary and includes, e.g., the perforated metal plate (Koide et al., 1985; Augier and Raimundo, 2021; Vandu et al., 2004) and capillary banks (Vélez-Cordero and Zenit, 2011; Vélez-Cordero et al., 2012; Kure et al., 2023). Figure 3.2 illustrates different configurations of capillary banks. An advantage of the capillary bank is the construction which avoids generation of gas jets (Vélez-Cordero and Zenit, 2011) and enables production of bubbles with a narrow bubble size distribution (Kure et al., 2023).

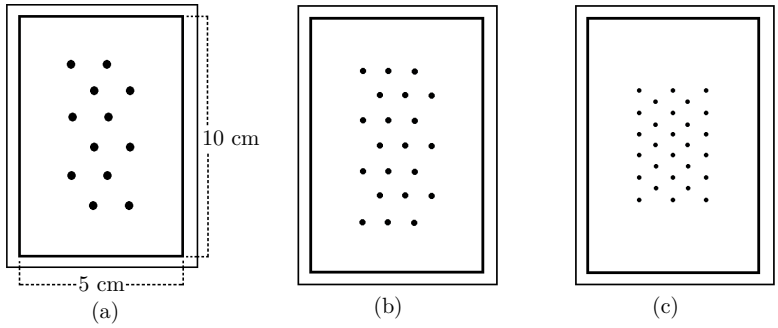

Figure 3.2: (a-c) Illustration of capillary bank configurations.

In bubble swarms, the bubble size is commonly measured by, e.g., the photographic method using a (high-speed) camera (Koide et al., 1985; Bouaifi et al., 2001; Vasconcelos et al., 2003; Sastaravet et al., 2020; Kure et al., 2023) or an endoscopic probe (Ali and Solsvik, 2020, 2021). A disadvantage with the photographic method using a high-speed camera described in section 3.1, is the potential limitation to systems with low gas volume fractions. That is, for higher gas volume fractions it is challenging to determine the bubble size based on the recorded images. With the development of artificial intelligence, ANN allows for evaluation of larger data-sets. By processing sufficiently large data-sets, statistically significant data may be obtained. Another photographic method is the photo-optical endoscope probe, where a probe is inserted into the multiple bubble system (Ali and Solsvik, 2020, 2021). The lens and illumination of the endoscopic probe ensure clear visualization of dense bubble dispersions. A drawback of the endoscopic probe is that it may interrupt the flow and affect the bubble properties (Ali and Solsvik, 2020). Furthermore, for systems including bubble aggregates, the area of the probe where the recording of the bubbles takes place may be too small for the aggregates to enter.

In bubble columns with bubble swarms, $k_{\mathrm{L}}a$ is commonly measured based on the so called dynamic method, the pressure based method, or chemical techniques. In the dynamic method, $k_{\mathrm{L}}a$ is measured by monitoring the change in the dissolved oxygen (DO) concentration in the liquid phase which occur due to a sudden change of the inlet gas phase, e.g., from N_2 to air, while the gas flow rate is kept constant (Vasconcelos et al., 2003; Doran, 2013; Kure et al., 2023). The DO concentration in the liquid phase is measured by means of an oxygen probe. A challenge with the dynamic method is the potential effect of probe response time on the measured $k_{\mathrm{L}}a$. If the time characteristics of the oxygen transport is of the same order as the response time of the probe, then it is necessary to introduce a correction to the interfacial

mass transfer model (Garcia-Ochoa and Gomez, 2009). The probe response time was measured for the considered system and operating conditions in Paper III, and the probe response time was found to be much smaller than the characteristic time of mass transfer and thus the dynamics of the oxygen probes could be neglected. Furthermore, a drawback of the dynamic method is the neglection of the gas-phase dynamics (Doran, 2013). Gas hold-up and gas mixing have a significant influence in most applications of the dynamic method (Doran, 2013), and thus this measurement method is most suitable for smaller vessels and not recommended for large scale bioreactors (Gogate and Pandit, 1999).

In the dynamic pressure method (Linek et al., 1989, 1993; Zednikova et al., 2018), a step-change in the oxygen concentration is introduced by a step-change of the pressure in the contactor while the gas flow rate is kept constant (Linek et al., 1989). The pressure method leads to a simultaneous change in the oxygen concentration for all the dispersed bubbles. An advantage of this method is that it suppresses the influence of non-ideal mixing of the gas phase on $k_{\mathrm{L}}a$ (Linek et al., 1989). A drawback of the method is that it can only be used for physical absorption (Zednikova et al., 2018). Furthermore, the probe signal of the dissolved oxygen probes measuring the change in oxygen concentration is sensitive to membrane movement, which can occur when introducing the pressure step change (Fujasová et al., 2007). For processes including chemical/biochemical reactions, a reaction enhancement factor should be considered in the mass transfer models (Zednikova et al., 2018; Garcia-Ochoa et al., 2010). In the dynamic pressure method, air can be used for the absorption of oxygen which nullifies the effects of non-ideal mixing of the dispersed phase (Gogate and Pandit, 1999) This is an advantage of the pressure based method and suggests that it may be well used for measurements of the mass transfer in industrial scale bioreactors (Gogate and Pandit, 1999).

Several chemical methods have been proposed for measuring $k_{\mathrm{L}}a$, such as sodium sulfite oxidation and CO_2 absorption. In the chemical methods, a reaction is necessary to reduce the DO concentration to a level lower than the saturation concentration (Garcia-Ochoa and Gomez, 2009). In the sodium sulfite oxidation method, sodium sulfite works as a reducing agent and reacts with the dissolved oxygen to produce sulfate in the presence of a catalyst (Garcia-Ochoa and Gomez, 2009). Within a specific concentration range of sodium sulfite, the reaction is very fast, and the oxygen concentration can be assumed zero. The reaction rate is much faster than the transfer rates of oxygen, and thus the rate of oxidation is mass transfer controlled (Garcia-Ochoa and Gomez, 2009). By measuring the overall rate, the in-

terfacial mass transfer can be determined. A drawback of the chemical methods is the addition of chemicals which can affect the liquid properties and thus the bubble hydrodynamics and the interfacial mass transfer. The dynamic method is employed for measurements of $k_{\mathrm{L}}a$ in bubble swarms in Paper III.

3.3 Fluid Rheology

Fluids include the phases of liquids and gases and can be classified according to their response to an externally applied pressure or according to their response to a shear stress (Chhabra and Richardson, 2008). The response of a fluid to an externally applied pressure leads to the characterization of being compressible or incompressible. Generally, gases are compressible while liquids are regarded as incompressible. An incompressible Newtonian fluid is a fluid that follows Newton's law of friction (Irgens, 2014). The shear stress, τ, is proportional to the shear rate, $\dot{\gamma}$, and the constant of proportionality is the dynamic viscosity, μ, according to equation (3.1):

$$\tau = \mu\dot{\gamma} \tag{3.1}$$

For a Newtonian fluid, μ is independent of τ and $\dot{\gamma}$, and depends only on the material and its temperature and pressure. Fluids that show a non-linear response to an applied stress is classified as non-Newtonian fluids, where the apparent viscosity, η, is defined as

$$\eta(\dot{\gamma}) = \frac{\tau}{\dot{\gamma}} \tag{3.2}$$

Most fluids are non-Newtonian in nature, including polymer solutions, drilling fluids, paints, fresh concrete, sewage sludge, toothpaste, and biological fluids, e.g., blood and saliva (Chhabra and Richardson, 2008). The non-Newtonian fluid models can be classified as: viscoelastic, time-dependent, or time-independent (Chhabra and Richardson, 2008). Viscoelasticity is characterized by concurrence of viscous and elastic response when subjected to deformation. The behavior of a time-dependent fluid is such that for a constant $\dot{\gamma}$ and at constant temperature, τ either increases or decreases monotonically with time towards an asymptotic value (Irgens, 2014). For these time-dependent fluids, the initial properties are regained some time after $\dot{\gamma}$ has returned to zero. The time independent fluids include shear-thickening, shear-thinning, and viscoplastic fluids. Shear-thickening rheological behavior is characterized by an increase in η with an increase in $\dot{\gamma}$. The behavior of viscoplastic fluids is characterized by the existence of a yield stress that must be exceeded before

the fluids deform. The shear-thinning rheological behavior is the most common and perhaps the most important response for many engineering applications (Bird et al., 1960; Chhabra and Richardson, 2008), and in contrast to the shear-thickening behavior, η decreases with increased $\dot{\gamma}$. Figure 3.3 illustrates the response to simple shear stress for Newtonian, shear-thinning, and shear-thickening rheological behavior.

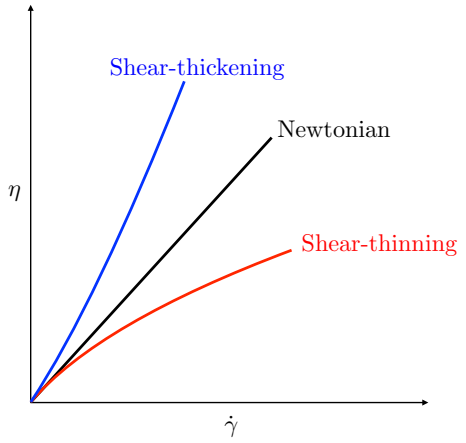

Figure 3.3: Illustration of the response to a simple shear stress for Newtonian (black), shear-thinning (red), and shear-thickening (blue) rheological behavior

Figure 3.3 shows that for the Newtonian behavior, the shear stress–shear rate is linear in accordance with equation (3.1), whereas the shear-thinning and shear-thickening fluids responses are non-linear. Several mathematical models with varying complexity are proposed to model the apparent viscosity of a shear-thinning fluid. The following models are most commonly used:

- The power-law model (de Waele, 1923; Ostwald, 1925). This model relates η to a power of $\dot{\gamma}$:

$$\eta(\dot{\gamma}) = m\dot{\gamma}^{n-1} \tag{3.3}$$

  where m and n denote the fluid consistency index and the power-law or flow behaviour index, respectively, and are empirical fitting parameters. For $n = 1$, the fluid shows Newtonian behavior, for $n < 1$, the fluid shows shear-thinning behavior, whereas for $n > 1$, shear-thickening behavior is observed. The power-law model offers the simplest representation of a shear-thinning fluid; however it has limitations such as application over a limited range of shear rates, i.e., the fitting parameter values of m and n depend on the considered range of shear rates. Moreover, it is not applicable for zero and infinite

shear viscosities. Despite its shortcomings, the power-law model is widely used in the literature concerning process engineering applications (Chhabra and Richardson, 2008).

- The Carreau-Yasuda model (Carreau, 1968; Yasuda, 1979).

$$\frac{\eta - \eta_\infty}{\eta_0 - \eta_\infty} = [1 + (\lambda\dot{\gamma})^b]^{(n-1)/b} \tag{3.4}$$

where η_0 and η_∞ denote the zero shear rate viscosity and the infinite shear rate viscosity, respectively. λ and b are fitting parameters. The model accounts for the limiting viscosity values (η_0 and η_∞) which are not captured by the power-law model. When $b = 2$ in equation (3.4), the model is known as the Carreau model (Bird et al., 1960).

Chapter 4

Journal Publications

The work within this dissertation has resulted in three journal articles given in the following sections as Paper I, Paper II, and Paper III. Paper I establishes an experimental facility with the ability to continuously track a single bubble during its ascent in stagnant liquid. The design and the technical details of the experimental set-up, the automatization including the control system and the processing of the data, are presented. Furthermore, the work includes investigation of bubble hydrodynamics. Here, the effects of bubble size and bubble trajectory on the terminal velocity are assessed. The experimental data are evaluated against literature data obtained in water of different quality and with different methods of bubble formation. A thorough evaluation of the statistical data analysis of the experimental data is provided. The work demonstrates the functionality of the experimental facility for its further use in single bubble interfacial mass transfer studies.

Paper II elucidates the phenomena of interfacial mass transfer for single bubbles rising in stagnant liquid. The experiments are carried out in the facility which was designed and constructed in the work of Paper I. The derivation of an expression for k_{L} is provided. Emphasis is placed on generating new experimental data of k_{L}, and to evaluate the effects of initial bubble diameter and bubble–liquid exposure time on k_{L}. Furthermore, k_{L}-correlations are implemented in a Lagrangian model description of a single bubble rising in stagnant water, and the numerical simulation results are compared with the experimentally obtained data.

Paper III contains the work on interfacial mass transfer from bubble swarms in an experimental facility designed and constructed for this purpose. Emphasis is placed on the effects of bubble size, liquid rheology, sparger design, and gas flow rate on the interfacial mass transfer. The individual effects of k_{L} and a on $k_{\mathrm{L}}a$ are evaluated in both Newtonian and non-Newtonian solutions, as few studies have studied the individual contributions of k_{L} and a in non-Newtonian solutions. The influence of bubble cluster formation on the interfacial mass transfer is investigated, which to the authors' knowledge, has not been experimentally examined prior to

this work. An image analysis algorithm using ANN (trained with annotated raw images obtained in this work) establishes a method for calculating an average bubble diameter from a bubble size distribution.

4.1 Paper I: Bubble Hydrodynamics of Single Bubbles

Physics of Fluids ARTICLE scitation.org/journal/phf

Experimental investigation of single bubbles rising in stagnant liquid: Statistical analysis and image processing

Cite as: Phys. Fluids 33, 103611 (2021); doi: 10.1063/5.0061581
Submitted: 28 June 2021 · Accepted: 27 September 2021 ·
Published Online: 19 October 2021

Ida K. Kure,[a] Hugo A. Jakobsen, Nicolas La Forgia, and Jannike Solsvik[b]

AFFILIATIONS

Department of Chemical Engineering, Norwegian University of Science and Technology (NTNU), N-7491 Trondheim, Norway

[a]Author to whom correspondence should be addressed: ida.k.kure@ntnu.no
[b]Electronic mail: jannike.solsvik@ntnu.no

ABSTRACT

Despite the large effort devoted to the study of single bubbles rising in a stagnant liquid, the complex phenomena involved have resulted in a large scatter in the terminal velocity. Providing new experimental data where the statistical uncertainty is thoroughly evaluated is therefore necessary. Single bubble experiments were conducted in a tall vertical column containing stagnant liquid at ambient conditions. To track the bubbles over the spatial range, high-speed cameras were mounted on a linear unit drive. The tall column allowed us to study the effect of hydrostatic pressure and late developed bubble dynamics on the bubble motion. The bubble properties, i.e., the bubble velocity, size, shape, and trajectory, were evaluated using an image analysis processing method. The analysis includes a quantitative evaluation of important parameters involved in the handling of the raw data. Several of the existing correlations for the terminal velocity were validated against the experimental data. The data are well predicted by the correlation proposed by Tomiyama *et al.* ["Terminal velocity of single bubbles in surface tension force dominant regime," Int. J. Multiphase Flow **28**, 1497–1519 (2002)]. The uncertainty in the experimental data has been emphasized, providing a quantitative evaluation based on several statistical methods. The number of experimental events necessary to obtain statistical significance was evaluated using a 95% confidence interval. Satisfying precision is found to be fulfilled for 10–15 bubble rise events. For bubbles of comparable size, the statistically significant terminal velocity data were found to exhibit a small scatter.

I. INTRODUCTION

Many industrial processes involve gas–liquid interactions, including systems such as chemical reactors (e.g., bubble column, slurry column),[1–3] biochemical reactors (e.g., stirred tanks),[4,5] distillation, fermentation, waste-water treatment, nuclear engineering,[6,7] and metallurgical bubble column reactors.[8]

Interfacial heat and mass transfer are important phenomena involved in gas–liquid systems, and these phenomena are largely affected by key properties such as the bubble size, shape, trajectory, and velocity. Although most industrial processes concerning gas–liquid interactions involve swarms of bubbles, the understanding of a single bubble phenomenon is crucial as it serves as a basis for more complex multiple bubble systems. A common approach in single bubble experiments is to inject a volume of gas into a stagnant continuous phase and determine the bubble properties after steady conditions are attained. The terminal velocity, i.e., the steady bubble rise velocity, is an important property associated with the analysis of bubbles. It is included as an approximation in dimensionless groups such as the bubble Reynolds number (Re_b) and the Weber number. Moreover, the terminal velocity is embedded in the steady drag coefficient. Accurate mathematical models predicting the terminal velocity are thus of great importance from a process design point of view.

A. Literature review: Terminal velocity of single bubbles

A variety of theoretical and experimental studies exist on freely rising single bubbles.[9–26] Spherical bubbles at $Re_b < 1$ can be evaluated based on the theory of Stokes[9] or Hadamard[11]–Rybczynski.[12] The model by Stokes[9] is applicable for contaminated systems, whereas the model by Hadamard[11]–Rybczynski[12] can be employed for clean systems. The terminal velocity of large spherical cap bubbles can be evaluated by the correlation of Davies and Taylor.[27] Recent models on the terminal velocity include the correlation proposed by Baz-Rodrígues

et al.,[23] and the correlation by Tomiyama *et al.*[18] given as a function of the bubble aspect ratio.

An overview of early experimental data on the terminal velocity of air bubbles in water is provided in the textbook of Clift *et al.*[28] The terminal velocities presented by Clift *et al.*[28] reveal a large scatter in the literature values. Generally, the large scatter in the terminal velocities has been attributed to the presence of surfactants, which accumulate on the bubble surface and influence the bubble properties.[28–30] While the presence of surfactants in the continuous phase has been shown to result in a decreasing bubble rise velocity for smaller bubbles ($d_b < 1.34$ mm),[29] the bubble rise velocities obtained in an ultra-pure water system are reported to be constant and attain higher values compared to what is obtained in a contaminated system.[22,31,32]

More recently, the large scatter in the terminal velocity data has been attributed to the influence of the method of bubble formation.[18,19] In the studies of Tomiyama *et al.*,[18] Okawa *et al.*,[19] Celata *et al.*,[21] and Liu *et al.*[25] bubbles were produced with small and large bubble shape deformations by changing the inner diameter of the bubble formation device. The bubbles produced with initially large bubble shape deformations were found to attain higher terminal velocities compared to the bubbles produced with initially small bubble shape deformations. Tomiyama *et al.*[18] observed a tendency toward a zigzag bubble rise path when the bubbles were produced with initially small bubble shape deformations, whereas initially large bubble shape deformations were found to enhance the transition from a zigzag to a helical bubble rise path.

Experimental data on the terminal velocity have commonly been obtained in vertical columns with a limited spatial range. A summary of the column geometries employed in previous studies are provided in Table I, where the majority have been performed in limited column heights. Except in the work by Merker *et al.*,[33] all the cameras reported in Table I were restricted to a fixed position. Merker *et al.*[33] designed a traverse system at which two high-speed cameras were attached to continuously record the bubbles during the bubble ascent. The two high-speed cameras provided a three-dimensional view of the bubble shape and trajectory. Most of the studies reported in Table I have employed one camera (one-sided image acquisition), where the bubble size has been calculated from the projected area using the bubble axes. In some cases, an additional camera has been employed for several experimental runs to validate the calculated bubble diameter, shape, and trajectory based on the one-sided image recordings.[21,25] In pure water, Celata *et al.*[21] found the difference in the volume equivalent bubble diameter based on image acquisition from two sides of the bubble to be 0.3%. Okawa *et al.*[19] and Liu *et al.*[25] found the calculated bubble diameter obtained by employing one- and two-high speed cameras to agree within an error of $\pm 10\%$.

The main results from several experimental works on bubble velocity, size, shape, and trajectory are summarized in Table II, including an overview of the reported statistical and image analysis. The statistical analysis is commonly limited to reporting on the uncertainties without further discussion on the obtained statistics or providing a description of the uncertainty calculation approach. While few studies are providing the statistics along with the statistical methodology employed,[20] in some studies the experimental uncertainty is absent.[22,32] Except from a stepwise description of the conversion from an original to a binary image in the work of Liu *et al.*,[24] the image analysis and processing reported in the studies in Table II are found limited.

B. Novel contribution

Limited studies on single bubbles exist where both the method of bubble formation is known and in which a detailed statistical analysis is provided. Commonly, the average value along with the standard deviation is given without a quantitative discussion on the uncertainty. A large number of experimental data on the terminal velocity have been provided in the last decades in the studies of Tomiyama *et al.*,[18] Okawa *et al.*,[19] Celata *et al.*,[21] Celata *et al.*,[20] and Liu *et al.*[25] The terminal velocities reported by Tomiyama *et al.*,[18] Okawa *et al.*,[19] Celata *et al.*,[21] and Celata *et al.*[20] represent individual bubble measurements, and not statistical averages. Except from the more detailed description of the uncertainty given by Celata *et al.*,[20] the analysis is commonly limited to reporting the final values of the error.

Employing an image acquisition technique, such as in the previously presented studies,[14,15,18–22,24,25,29] is an advantage due to the method being non-intrusive. Despite the large application of the image acquisition technique, evaluation of the statistical uncertainty associated with image processing and analysis is limited to more recent work. A minimal discussion is found on the choice of threshold values used in the image analysis and the influence of the threshold on the calculated data. Commonly, only the applied value of the threshold is reported in the literature.

Experimental data acquisition is often very time-consuming. The statistical validity is often attributed and limited to the number of experiments. Regardless of this, few studies are found to attempt defining the minimal number of experimental events needed to obtain statistical significance.

This paper will provide new experimental data on the terminal velocity of single air bubbles in stagnant water at ambient temperature, in which it is explicitly reported on the method of bubble formation. The reported values will be average values calculated based on several single bubble events. A thorough evaluation will be given on the statistical uncertainty in the experimental data. The evaluation will be based on several statistical methods. Additionally, an evaluation will be given on the number of necessary bubble events to ensure data of statistical significance.

Unlike most previous studies, an experimental facility with the ability to continuously track the bubble was constructed in this study to generate experimental data of a rising bubble over a long vertical distance. The design and control of the dynamic facility will enable rapid changes in the mechanical parts involved, adapting to the transient motion of the bubble. High-resolution image acquisition over a longer vertical distance allows for investigation of potentially late developed bubble dynamics, in addition to the influence of the hydrostatic pressure. Contributing to the limited literature, a detailed description will be outlined on the system control of the dynamic facility.

The image processing method will be described in detail. The choice of important parameters influencing the calculated quantities will be emphasized. Such an important parameter is the threshold value used in the binarization of the original images. A sensitivity analysis will be given in which the bubble velocity and size are calculated considering several threshold values.

TABLE I. A summary of the experimental setups applied in previous publications.

Reference	Column	Camera setup	Bubble formation	Bubble diameter (mm)	Gas	Liquid	Temperature	Measured quantity
Aybers and Tapucu[29]	$17 \times 17 \times 100\,cm^3$	One camera, partly movable	Glass capillary	0.8–7.1	Air	Water	18 °C–39.1 °C	Bubble size, velocity, trajectory, shape
Duineveld[31]	$50 \times 50 \times 50\,cm^3$	One camera, fixed	⋯	0.7–1.9	Air	Ultrapure water ($\geq$ 18 MΩ cm)	19.6 ± 0.2 °C	Bubble size, velocity, shape
Wu and Gharib[32]	$15 \times 15 \times 61\,cm^3$	One camera, fixed	Glass capillary	1.0–2.1	Air	Deionized + distilled water, Ultrapure water ($\geq$ 18 MΩ cm)	22 ± 0.3 °C	Bubble size, velocity, path, shape
Tomiyama *et al.*[18]	$10 \times 20 \times 20\,cm^3$	Two cameras, fixed	Nozzle	0.6–11	Air	Distilled water, distilled water w/ 0.000 75% soap	Ambient	Bubble size, velocity, trajectory, shape
Okawa *et al.*[19]	$25 \times 30 \times 40\,cm^3$	Two cameras, fixed	Glass and sst pipe	0.7–3.7	Air	Distilled water	15 °C–90 °C	Bubble size, velocity, shape
Celata *et al.*[21]	$10 \times 10 \times 30\,cm^3$	One camera, fixed	Nozzle	0.5–6	N_2	Distilled-, de-ionized-, tap water, pure FC-72	Ambient	Bubble size, velocity, trajectory, shape
Celata *et al.*[20]	$10 \times 10 \times 30\,cm^3$	One camera, fixed	Glass nozzle, orifice in flat brass	0.5–4	N_2	Deionized water, refrigerant FC-72	Ambient	Bubble size, velocity, shape
Liu *et al.*[25]	$15 \times 15 \times 50\,cm^3$	One camera, fixed	Sst nozzle, flat top	0.5–11	Air	Water, glycerin aqueous solution	8 °C–29 °C	Bubble size, velocity, trajectory, shape
Sanada *et al.*[22]	⋯	One camera, fixed	Orifice in nylon tube	0.4–1.7	N_2	Ultrapure water ($\geq$ 18 MΩ cm)	23 °C–25.4 °C	Bubble size, velocity, shape
Merker *et al.*[33]	$7.5 \times 200\,cm^2$	Two cameras, movable	Capillary	0.9–2.8	Air,	CO_2,NO	Ultrapure water (0.055μ S cm^{-1})	25 °C
Bubble size, velocity, trajectory, shape, mass transfer coefficient								
Current work	$4 \times 4 \times 200\,cm^3$	One camera, movable	Glass needle	0.8–1.9	Air	Deionized water	23±0.5°C	Bubble size, velocity, trajectory, shape

TABLE II. A summary of the main results from the studies in the literature review.

Reference	Main results	Image analysis	Statistical analysis
Tomiyama *et al.*[18]	Strong dependency between the initial bubble shape deformations, terminal velocity, and trajectory. Small initial bubble shape deformations resulted in low terminal velocity and high bubble aspect ratio. Initial small bubble shape deformations commonly result in a zigzag rise path. Large initial bubble shape deformations resulted in higher terminal velocities and lower bubble aspect ratio. Terminal velocity of contaminated bubbles agreed with clean bubbles with small initial shape deformations.	Illustrations of original and binarized images	Uncertainty in bubble velocity based on the spatial resolution of the images.
Okawa *et al.*[19]	At normal temperature, the bubble velocity and onset to path oscillations were affected by the method of formation. Bubbles with initial large shape deformations are well predicted by terminal velocity correlations for pure systems. Terminal velocity correlations for contaminated systems are suitable for bubbles with initial small shape deformations. At high temperatures, a dependency between the terminal velocity and the bubble formation method was observed.	No detailed description.	Velocity: estimated error ± 2 mm/s.
Celata *et al.*[21]	Large scatter in terminal velocity data for both pure and contaminated liquids. Large initial bubble shape deformations observed when the bubble diameter exceeded the nozzle diameter. Initial large bubble shape deformations resulted in higher terminal velocities than with initial small bubble shape deformations. Best model predictions: $d_b > 1.3$ mm: Tomiyama *et al.*[18] in both contaminated and pure water, $d_b < 1.3$ mm: Peebles and Garber[13] for pure water and Ishii and Chawla[34] for contaminated water.	No detailed description.	Bubble position: estimated error ± 0.1 mm Uncertainties: Terminal velocity: $\pm 5.2\%$, Bubble diameter: average error $\pm 5.2\%$, with values ranging from $\pm[3.4, 7.9]\%$. Bubble shape: mean error $\pm 10\%$ with values ranging from $\pm[7.0, 15.0]\%$.
Celata *et al.*[20]	Best model prediction for the terminal velocity given by the correlation of Tomiyama *et al.*[18] Model predictions found to exhibit an error up to $\pm 50\%$.	No detailed description.	Instantaneous bubble velocity: $\pm[1.7, 15.4]\%$, terminal velocity: $\pm[0.7, 2.0]\%$ (unknown if water or FC-72). Bubble diameter: $\pm 2.9\%$, ranging from $\pm[1.0, 11.0]\%$ in water, $\pm 4.3\%$, ranging from $\pm[2.0, 9.0]\%$ in FC-72. Bubble aspect ratio: $\pm 6.6\%$, ranging from $\pm[0.4, 20.0]\%$ in water, $\pm 6.2\%$, ranging from $\pm[0.6, 20.0]\%$ in FC-72.
Liu *et al.*[25]	Higher terminal velocity and lower bubble aspect ratio with helical rise path.		Uncertainties: Terminal velocity: $\pm[0.04, 4.65]\%$, bubble diameter: $\pm[2.0, 8.3]\%$ for $d_b \in (0.5, 1.0)$ mm, $\pm[1.6, 4.0]\%$ for $d_b \in (1.0, 2.5)$ mm.
Liu *et al.*[24]	Further evaluation of the data obtained by Liu *et al.*[25] Best model prediction: Tomiyama *et al.*[18] in water. Moreover, the data were well predicted by the proposed correlation of Ishii and Chawla.[34]	Description of the stepwise conversion from an original to a binary image.	

TABLE II. (Continued.)

Reference	Main results	Image analysis	Statistical analysis
Wu and Gharib[32]	Bubble shape, velocity, and rise path are influenced by the inner diameter of the capillary. Inner diameter of the capillary exceeding the bubble diameter resulted in lower terminal velocities than obtained when the bubble diameter exceeded the capillary inner diameter. Terminal velocity data for bubbles produced with direct injection of air (pinch-off method) coincided with the data obtained when the capillary inner diameter was smaller than the bubble diameter.	No description.	No statistical analysis.
Sanada *et al.*[22]	Critical bubble Reynolds number was found susceptible to the height of observation. The height of onset to path oscillations decreased for increasing bubble Reynolds number, while the height at which a terminal velocity was reached remained approximately unchanged. Discrepancy between the experimental data and the theoretical correlations for the bubble aspect ratio.	Limited discussion	No statistical analysis.

Finally, the accuracy of existing correlations for the terminal velocity will be assessed for bubbles in the size range $d_b \in [0.8, 1.9]$ mm. An attempt will be made to identify the most suitable correlation for the bubble shape, expressed in terms of dimensionless numbers.

II. BUBBLE HYDRODYNAMICS

A. Terminal velocity

A single bubble ascending in stagnant liquid rises under the influence of gravity. The main forces governing the bubble motion are buoyancy and drag. From the momentum balance formulation,[35] generally referred to as Newton's second law, the bubble velocity at which it rises can be determined:

$$\frac{d}{dt}(m_b v_b) = \rho_l g V_b - m_b g - \frac{1}{2}\rho_l C_D A_b^p |v_b| v_b + \dot{m} v_b S_b, \quad (1)$$

where m_b denotes the mass of the bubble, v_b the bubble velocity, ρ_l the liquid density, g the acceleration of gravity, V_b the bubble volume, C_D the drag coefficient, $A_b^p = S_b/4$ the projected area of the bubble, $S_b = \pi d_b^2$ the bubble surface, d_b the volume equivalent bubble diameter, and $\dot{m}$ the mass flux over the bubble interface. The LHS of (1) is the rate of change of linear momentum, the first and second terms on the RHS correspond to the body forces resulting from hydrostatic pressure and gravity, respectively, and the third term denotes the steady drag. Note that history-, lift-, and virtual mass forces have been neglected. The fourth term represents a source/sink term due to interfacial mass transfer. When there is net-zero transfer of mass across the bubble interface, $\dot{m} = 0$ and the fourth term vanishes.

When the buoyancy, gravity, and drag forces are balanced, a terminal velocity, v_T, is reached. By specifying the drag coefficient, the terminal velocity can be computed from the force balance in Eq. (2), or vice versa. It should be noted that the viscous and surface tension forces are implicitly expressed through the drag coefficient in Eq. (2),

$$v_T = \sqrt{\frac{4 d_b (\rho_l - \rho_g) g}{3 \rho_l C_D}}, \quad (2)$$

where ρ_g denotes the density of the gas.

The wake, which resides behind a rising bubble, plays an important role in the flow dynamics. When the relative velocity between an ascending bubble and the surrounding liquid is very low, the flow adjacent to the bubble will follow closely to the bubble surface. That is, for small bubble Reynolds numbers. As the bubble Reynolds number increases, the flow starts to separate from the bubble surface and the streamlines rejoin behind the bubble, forming a wake.[36] Determining the terminal velocity of an ascending bubble in a quiescent liquid is challenging due to the complex bubble dynamics and phenomena involved.

The terminal velocity is largely influenced by the bubble size, shape, and trajectory, the method of bubble formation, the fluid properties, and the degree of liquid contamination. A common approach when analyzing the terminal velocity is to distinguish between three regimes.[28] The regimes are: (1) the spherical regime ($d_b < 1$ mm), (2) the ellipsoidal regime (1 mm $< d_b <$ 18 mm), and (3) the spherical cap regime (18 $< d_b$ mm).

In the spherical regime (1), viscosity and buoyancy forces dominate the bubble motion. The bubbles are of spherical or close to a

spherical shape, the rise path is rectilinear, and the terminal velocity increases with increasing bubble size.

In the ellipsoidal regime (2), surface tension and inertia forces dominate the bubble motion. The bubble shape varies from the oblate ellipsoidal, spherical cap, or ellipsoidal-cap with surface wobbling. The terminal velocity may increase, stay constant, or decrease, depending on the bubble size. As the bubble size increases above $d_b = 1$ mm, a transition from a rectilinear to an oscillating rise path is observed. Here, the bubbles may take helical, zigzag, or rectilinear with rocking paths.[28] A wide scatter in available terminal velocity data is observed in the ellipsoidal regime.[18,28,36] Previously, the scatter has been attributed to the presence of surfactants. Surfactants in the continuous phase have been shown to significantly impact the bubble dynamics.[29,30,37] Frumkin and Levich[38] suggested the reduction in the terminal velocity with the presence of impurities to be explained by surfactant concentration gradients on the bubble surface, forming a stagnant cap (for illustration see, e.g., Alves *et al.*[30]). Surfactants in the front of the bubble are dragged to the rear end due to surface advection by the main flow. A surface tension gradient is formed, causing a tangential stress (the Marangoni effect), which opposes the viscous stress at the surface.[37] The surface mobility is affected, and the drag coefficient increases toward that of a rigid sphere.[30] Griffith[37] found the surface tension of smaller bubbles to cause the surface to become saturated. The saturation of the surface resulted in the bubble velocity decelerating more rapidly. Bubbles of size $d_b = 1.34$ mm reached a terminal velocity at which they rose for a longer time. Griffith[37] argued that the lack of negative effects of impurities on the terminal velocity of larger bubbles was due to their fast ascent. With a fast bubble ascent, the shearing forces on the bubble surface increase. As the shearing forces exceed the surface tension forces, impurities are not able to accumulate at the surface. More recently, Tomiyama *et al.*[18] and Okawa *et al.*[19] found scattering in the surface tension dominated regime to be caused by the bubble injection method, which influences the initial bubble shape deformation, the trajectory, and the terminal velocity. Tomiyama *et al.*[18] and Okawa *et al.*[19] observed bubbles with initially small bubble shape deformations to take a zigzag motion. On the contrary, large initial bubble shape deformations resulted in an enhanced transition from a zigzag to a helical rise path. Confirming the earlier observations by Saffman[39] and Ellingsen and Risso,[40] the transition from a zigzag to a helical path occurred, while the opposite was never observed. The bubbles formed with initial large shape deformations were found by Tomiyama *et al.*[18] and Okawa *et al.*[19] to take higher terminal velocities compared to the bubbles produced with initially small shape deformations. Wu and Gharib[32] and Liu *et al.*[25] reported on similar trends where higher terminal velocities were achieved when the bubbles were produced with initially large shape deformations compared to initially small shape deformations.

There is still no complete understanding of the phenomena causing the scattering in the terminal velocity data. At present, the scatter is attributed to either differences in the initial bubble shape deformations, concentration of surfactants, or wake evolution.[20,21]

In the spherical cap regime (3), the bubbles take spherical cap form, and the inertia- and buoyancy forces dominate the bubble motion. The terminal velocity is observed to increase with increasing bubble diameter. Despite the suggested limits separating the three regimes by Clift *et al.*,[28] there are no clear transition criteria in the literature.[20] Recently reported terminal velocity data by Liu *et al.*[24] are significantly different from the data obtained by Bryn,[41] Gorodetskaya,[42] Davies and Taylor,[43] and Napier *et al.*,[44] that are reported in the textbook of Clift *et al.*[28] Liu *et al.*[24] suggested that the differences in the observed regime limits are caused by the sensitivity of the terminal velocity to the bubble shape.

Several correlations have been proposed for the explicit computation of the terminal velocity. A summary of the proposed correlations is given in Table III. Stokes[9] and Hadamard[11]–Rybczynski[12] proposed correlations for spherical bubbles at $Re_b < 1$. The correlation by Stokes[9] is applicable for bubbles with immobile surfaces, while the correlation by Hadamard[11]–Rybczynski[12] is applicable for bubbles with mobile surfaces. Using boundary-layer theory, Levich[10] developed an expression, which is valid for spherical bubbles at $50 < Re_b < 500$. The correlations suggested by Stokes,[9] Hadamard[11]–Rybczynski,[12] and Levich[10] differ only by a constant. Based on the hydrodynamic theory of waves, Mendelson[16] proposed an expression for explicit computation of the terminal velocity of intermediate-sized bubbles in pure liquids. Fan and Tsuchiya[36] suggested an expression for the terminal velocity which is applicable for both pure and contaminated systems. Depending on the choice of coefficients, the expression by Fan and Tsuchiya[36] can be adjusted to predict a specific system. Proposed values of the coefficients are given in Table III. Other recommended values can be found in the textbook by Fan and Tsuchiya.[36] The correlation by Fan and Tsuchiya[36] includes two terms. The first term equals the correlation by Mendelson,[16] and the second term equals the correlation by Stokes,[9] Hadamard[11]–Rybczynski,[12] or Levich.[10] The coefficient applied for the second term depends on the specific system.

Tomiyama *et al.*[18] observed a dependency of the terminal velocity on the bubble aspect ratio, where the terminal velocity was pointed out to be a decreasing function of the bubble aspect ratio, E, defined as

$$E = \frac{b}{a}, \tag{3}$$

where b is the horizontal (major) bubble axis and a is the vertical (minor) bubble axis. For a spherical bubble, $a = b$, and the bubble aspect ratio in Eq. (3) will equal to unity. Tomiyama *et al.*[18] formulated a correlation to predict the terminal velocity in the ellipsoidal regime. The correlation is a function of the bubble aspect ratio, the vertical line angel, ϕ, and the distortion factor, $\gamma = 2/(1+\beta)$ (for illustration see, e.g., Tomiyama *et al.*[18]), where β is the ratio between the short and long part of the minor axis in a distorted oblate spheroidal bubble. The model is derived under the assumption of spheroidal bubbles with the distortion factor ranging from unity for ellipsoidal bubbles to a value of 2 for cap bubbles. Assuming spheroidal bubbles and the potential flow to be valid only in the vicinity of the bubble nose (Tomiyama *et al.*[18]), the model reduces to that given in Table III.

B. Drag coefficient

The drag force is an important force governing the bubble motion. Much effort has been devoted to develop accurate models for the drag coefficient.[17,26,34,46] The drag coefficient is commonly expressed in terms of dimensionless groups: Morton number [$Mo = (\rho_l - \rho_g) g \mu_l^4 / \sigma^3 \rho_l^2$], Eötvös number [$Eo = g d_b^2 (\rho_l - \rho_g)/\sigma$], bubble Reynolds number ($Re_b = \rho_l v_b d_b / \mu_l$), and Weber number ($We = \rho_l v_b^2 d_b / \sigma$). Only three of these numbers are independent, as the Eötvös number can be expressed as $Eo = Re_b^4\, Mo / We^2$.[3]

TABLE III. Correlations for the terminal velocity.

Reference	Correlation	Remarks
Stokes,[9] Hadamard[11]-Rybczynski[12]	$v_T = \frac{1}{K_b}\frac{(\rho_l - \rho_g)gd_b^2}{\mu_l}$	Spherical bubbles, immobile surfaces $Re_b < 1$, $K_b = 18, 12$ for Stokes and Hadamard–Rybczynski, respectively
Haberman and Morton[14]	$v_T = \frac{1}{18}\frac{\Delta\rho g d_b^2}{\mu_l}\left[\frac{3\mu_l + 3\mu_g}{2\mu_l + 3\mu_g}\right]$	Small bubbles
Levich (1962), referred by Ref. 36	$v_T = \frac{1}{36}\frac{(\rho_l - \rho_g)gd_b^2}{\mu_l}$	Spherical bubbles, $50 < Re_b < 500$
Mendelson[16]	$v_T = \sqrt{\frac{2\sigma}{\rho_l d_b} + \frac{gd_b}{2}}$	Intermediate to large bubbles, pure liquids
Fan and Tsuchiya[36]	$v_T = (v_{b1}^{-n} + v_{b2}^{-n})^{-1/n}$	Pure and contaminated systems
	$v_{b1} = \frac{\rho_l g d_b^2}{K_b \mu_l}$	$K_{b0} = 14.7$ (aqueous solutions)
		$K_{b0} = 10.2$ (organic solutions)
	$v_{b2} = \sqrt{\frac{2c\sigma}{\rho_l d_b} + \frac{gd_b}{2}}$	$c = 1.2$ (mono-component liquid)
		$c = 1.4$ (multi-component liquid)
	$K_b = \max(12, K_{b0} Mo^{-0.038})$	$n = 1.6$ (clean system)
		$n = 0.8$ (contaminated system)
Mendelson[45]	$v_T = \frac{v_H v_M}{\sqrt{v_H^2 + v_M^2}}$	v_H and v_M are correlations proposed by Haberman and Mendelson, respectively
Tomiyama *et al.*[18]	$v_T = \frac{\sin^{-1}\sqrt{1-E^2} - E\sqrt{1-E^2}}{1-E^2}\sqrt{\frac{8\sigma E^{4/3}}{\rho_l d} + \frac{\Delta\rho g d}{2\rho_l}\frac{E^{2/3}}{1-E^2}}$	Pure and contaminated Newtonian liquids
Baz-Rodrígues *et al.*[23]	$v_T = \frac{1}{\sqrt{(v_{T1}^2 + v_{T2}^2)^{-1}}}$	Pure liquids
	$v_{T,pot} = \frac{1}{36}\frac{\Delta\rho g d_b^2}{\mu_l}$	
	$v_{T1} = v_{T,pot}[1 + 0.73667(gd_b)^{1/2} v_{T,pot}^{-1}]^{1/2}$	
	$v_{T2} = \sqrt{\frac{3\sigma}{\rho_l d_b} + \frac{\Delta\rho g d_b}{2\rho_l}}$	

Henceforth, the bubble Reynolds number will be referred to as the Reynolds number. Table IV presents the correlations for the drag coefficient employed in the analyses of the terminal velocity in this work. All of the forces governing within each of the terminal velocity regimes, presented in Sec. II A, are involved in the proposed drag coefficients in Table IV.

Tomiyama *et al.*[17] developed a general correlation for the drag coefficient, taking into account the effects of fluid properties, gravity, bubble diameter, and contamination level characterized as clean, partly contaminated, and contaminated systems. Distilled water corresponds to a clean system, tap water corresponds to a contaminated system, and water with purity in between these categories corresponds to a partly contaminated system. It should be noted that the correlations by Ishii and Chawla[34] and Peebles and Garber[13] in Table IV are not given in their original formulations. Tomiyama *et al.*[17] rewrote the correlations by Ishii and Chawla[34] and Peebles and Garber[13] in terms of the Eötvös and Morton numbers. The drag coefficient by Peebles and Garber[13] in Table IV was rewritten by Celata *et al.*[21] in terms of the Eötvös and Weber numbers.

In a recent study by Yan *et al.*,[26] a correlation applicable for non-spherical bubbles was proposed. The existing correlations considered by Yan *et al.*[26] were found to over- or underestimate the drag coefficient when dealing with periodically fluctuating velocities. Yan *et al.*[26] proposed a new correlation for the drag coefficient, based on that by Schiller and Naumann,[47] involving the Reynolds, Weber, and Eötvös numbers for non-spherical bubbles, i.e., taking into account the bubble shape deformations. For spherical bubbles, Yan *et al.*[26] recommended the drag correlation by Tomiyama *et al.*[17] for contaminated bubbles.

TABLE IV. Correlations for the drag coefficient.

Reference	Correlation	System
Ishii and Chawla[34]	$C_D = \max\left\{\frac{24}{Re_b}\left(1+0.2Re_b^{0.75}\right), \min\left[\frac{2}{3}\sqrt{Eo}, \frac{8}{3}\right]\right\}$	
Peebles and Garber[13]	$C_D = \max\left\{\max\left(\frac{24}{Re_b}, \frac{18.7}{Re_b^{0.68}}\right), \min(0.0275EoWe^2,\ 0.82Eo^{0.25}We^{0.5})\right\}$	
Tomiyama *et al.*[17]	$C_D = \max\left\{\min\left[\frac{16}{Re_b}\left(1+0.15Re_b^{0.687}\right), \frac{48}{Re_b}\right], \frac{8}{3}\frac{Eo}{Eo+4}\right\}$	Clean
Tomiyama *et al.*[17]	$C_D = \max\left\{\min\left[\frac{24}{Re_b}(1+0.15Re_b^{0.687}), \frac{72}{Re_b}\right], \frac{8}{3}\frac{Eo}{Eo+4}\right\}$	Partly contaminated
Tomiyama *et al.*[17]	$C_D = \max\left\{\frac{24}{Re_b}(1+0.15Re_b^{0.687}), \frac{8}{3}\frac{Eo}{Eo+4}\right\}$	Contaminated
Yan *et al.*[26]	$C_D = \max\left\{\min\left(\frac{24}{Re_b}(.\ 1+0.15Re_b^{0.678}), \frac{72}{Re_b}\right), \frac{24}{Re_b}(1+0.15Re_b^{0.687})\frac{Re_b^{0.55}Eo^{0.95}We^{-1.10}}{12.6}\right\}$	

The predictability of the correlation for spherical bubbles in clean water is therefore questionable.

C. Bubble aspect ratio

A common approach is to correlate the bubble aspect ratio by dimensionless numbers, such as the Eötvös, Weber, and Tadaki numbers. Table V presents correlations for the bubble aspect ratio in terms of the Eötvös and Weber numbers. Tomiyama *et al.*[48] observed a strong correlation between the bubble aspect ratio and the Weber number. Formulations on the basis of the Eötvös number have been stated to be inaccurate due to the dependency of the detachment condition, i.e., the initial bubble deformations. Close to spherical bubbles deform to a smaller extent and are less affected by the detachment condition. Okawa *et al.*[19] argued that formulations for the bubble aspect ratio in terms of the Eötvös number should be restricted to smaller bubbles. For a close to spherical bubble, rising under the assumption of inviscid flow around the bubble surface, Moore[49] derived the following correlation:

$$We = 4\chi^{-4/3}\frac{(\chi^3+\chi-2)\left[\chi^2\sin^{-1}\chi-\chi\sqrt{\chi^2-1}\right]^2}{(\chi^2-1)^{-3}}, \quad (4)$$

where χ is the reciprocal of the bubble aspect ratio.

For low-viscosity liquids, $Mo < 2.5\times10^{-4}$, Tadaki and Maeda[51] proposed the following correlations for the bubble aspect ratio based on a dimensionless group, later referred to as the Tadaki number, $Ta = ReMo^{0.23}$.[28]

$$\frac{d_b}{b} = \begin{cases} 1, & Ta < 2, \quad (5a)\\ 1.14Ta^{-0.176}, & 2 < Ta < 6, \quad (5b)\\ 1.36Ta^{-0.28}, & 6 < Ta < 16.5, \quad (5c)\\ 0.62, & 16.5 < Ta, \quad (5d)\end{cases}$$

TABLE V. Correlations for the bubble aspect ratio based on the Eötvös and Weber numbers.

Reference	Correlation	Note
Wellek *et al.*[50]	$E = \frac{1}{1+0.163Eo^{0.757}}$	Non-oscillating drops, contaminated liquid
Okawa *et al.*[19]	$E = \frac{1}{1+0.163Eo^{1.3}}$	Modification of Wellek
Sanada *et al.*[22]	$E = \frac{1}{1+6.5Eo^{1.925}}$	Fitted to experimental data
Moore[49]	$E = \frac{1}{1+\frac{9}{64}We}$	Approximation of Eq. (4)
Taylor and Acrivos	$E = \frac{1}{1+\frac{5}{32}We}$	Originally developed for creeping flow
Wellek *et al.*[50]	$E = \frac{1}{1+0.091We^{0.95}}$	Non-oscillating drops, fairly contaminated liquid

where $d_b/b = E^{1/3}$ for ellipsoidal bubbles.

Vakhrushev and Efremov[52] modified the correlation by Tadaki and Maeda:[51]

$$E = \begin{cases} 1, & \mathrm{Ta} < \mathrm{Ta}_1, \quad (6a) \\ c_1 + c_2 \tanh\left[c_3(c_4 - \log_{10})\mathrm{Ta}\right]\}^2, & \mathrm{Ta}_1 < \mathrm{Ta} < \mathrm{Ta}_2, \quad (6b) \\ c_5, & \mathrm{Ta}_2 < \mathrm{Ta}, \quad (6c) \end{cases}$$

where, for pure water, Fan and Tsuchiya[36] suggested the following parameter values: $c_1 = 0.77$, $c_2 = 0.24$, $c_3 = 1.19$, $c_4 = 0.40$, $c_5 = 0.30$, $\mathrm{Ta}_1 = 0.3$, and $\mathrm{Ta}_2 = 20$.

III. EXPERIMENTAL SETUP

Single bubble experiments are carried out in a vertical column with dimensions $200 \times 4 \times 4$ cm^3, as illustrated in Fig. 1. Column walls made of plexiglass allow for image recording of the single bubble as it rises through the column. An individual single bubble is generated through a glass needle using a syringe pump (KdScientific Legato200). By varying the nozzle size, the initial size of the bubble can be varied. To capture the evolution of a bubble during its rise through the column, a high-speed camera (Photron FASTCAM MINI AX100) with a lens (Navitar 6.5× zoom with 12 mm fine focus, and a 1× F-mount adapter) is installed on a linear unit drive (ISEL LES5, Controller MC 1–20) parallel to the column. Images are recorded at a frame rate of 1000 fps and shutter speed in the range of 1/12 000–1/18 000 s. Henceforth, this camera is referred to as *camera I*. Depending on the bubble size injected, the images capture a physical space between 20×20 and 28×28 mm^2 of the column (image resolution is 1024×1024 px^2). Images recorded by camera I are locally stored in the memory of the camera during the bubble rise event and thus not available for analysis in the computer software during this time. To allow for real-time analyses of images, a second high-speed camera (AOS PROMON U750) is installed on the linear unit drive, similar to camera I. This high-speed camera, which is referred to as *camera II*, transfers real-time recorded images to the computer for analysis of the bubble position, which in turn is used to adjust the velocity of the linear unit drive. Camera II is operated at a frame rate of 25 fps and exposure time 300 ms. A light-emitting diode (LED) (MultiLed QT+, GSVitec, with luminous flux white, 12 000 lumen, and power 150 W) is located opposing the cameras, and a diffusion paper attached to the associated wall ensures homogeneous light distribution and elimination of reflections from the bubble surface or the column walls. The LED diode is connected to a multiLED G8 controller (GSVitec).

Deionized water at room temperature of 23° C is used as the continuous phase. The inlet water is purified by a purification system (pretreatment (Progard) and Millipore RiOS150), removing 95%–99% of the ions and 99% of dissolved organic substances, microorganisms, and particles. The liquid phase oxygen concentration is measured using dissolved oxygen probes (METTLER TOLEDO InPro6860i). Three dissolved oxygen probes are installed on the column. The probes are used to ensure that the water is saturated with air, i.e., that there is a net-zero mass transfer between the bubble and the continuous phase. The system components, that is, the syringe pump, the linear unit drive, and the two high-speed cameras, are controlled through the software National Instruments LabVIEW. An outline of the working principles of the system control is given in Sec. IV. The description of the system control includes the image processing by camera II and the system control of the linear unit drive. The analysis of the images obtained by camera I, used for evaluation of the bubble properties, is outlined in Sec. V.

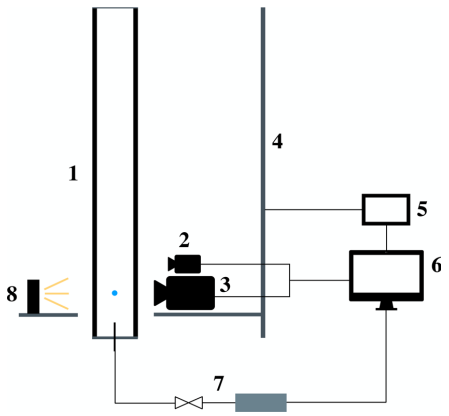

FIG. 1. The experimental facility is composed of (1) liquid column, (2) camera II, (3) camera I, (4) linear unit drive, (5) controller, (6) computer, (7) syringe pump, (8) LED panel.

IV. AUTOMATION OF THE EXPERIMENTAL SETUP

A. Image analysis to determine the linear unit drive velocity—Camera II

To adapt the linear unit drive to the velocity of a bubble rising in the column, images from camera II are continuously processed in LabVIEW. An original image recorded by camera II is shown in Fig. 2. The bars present on the LHS of the column in Fig. 2 are used as a reference of length to estimate the position and velocity of the linear unit drive. The bars on the RHS are used by camera I in the image processing and analysis to determine the bubble properties, as described in Sec. V. Operated at a frame rate of 25 fps, camera II is not able to

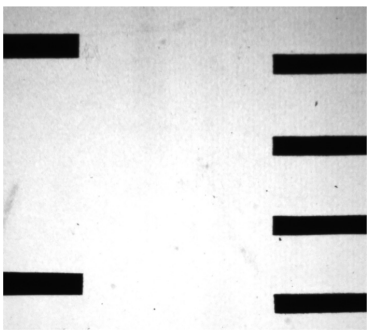

FIG. 2. Original image recorded by camera II.

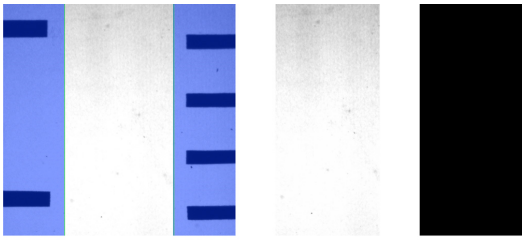

FIG. 3. (a) Original image including the selected region to be discarded, (b) cropped image, and (c) binarized image used in the bubble data processing.

process bars with a spatial distance less than 18 mm. Hence, two sets of bars are employed to meet the constraints by camera I and II.

Two regions of interest (ROI) are extracted from the image in Fig. 2. The blue/darker areas in Figs. 3(a) and 4(a) are the areas to be neglected from the original image in Fig. 2. Figures 3(b) and 4(b) show the resulting cropped ROIs. Prior to the binarization of the images in Figs. 3(b) and 4(b), threshold values are pre-selected. The threshold values are chosen to eliminate pixels not related to the bubble or the bars. The final binarized images of the two ROIs are shown in Figs. 3(c) and 4(c), where Fig. 3(c) captures the ascending bubble and Fig. 4(c) includes the bars, which are employed to calculate the velocity and position of the bubble and the linear unit drive.

B. System control—Bubble tracking and linear unit drive velocity

To adapt to the transient motion of an ascending bubble, the velocity of the linear unit drive is continuously updated. This is done by estimating the instantaneous bubble velocity from the images obtained by camera II. Henceforth, time (t), all velocities (v), and position (y, x) are given in units ms, cm/s, and px, respectively. The bubble velocity relative to camera II, $v_{\mathrm{rel,b}}$, is obtained by dividing the change in the bubble position between two consecutive images, Δx_{b}, by the time between the two recorded images, Δt:

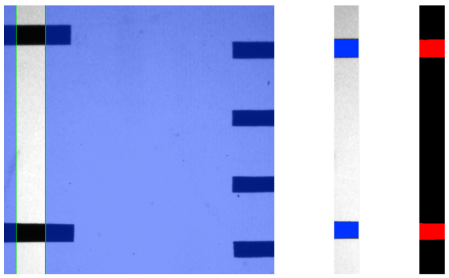

FIG. 4. (a) Original image including the selected region to be discarded, (b) cropped image, and (c) binarized image of the bars used in the linear unit drive velocity control.

$$v_{\mathrm{rel,b}} = \zeta \frac{\Delta x_{\mathrm{b}}}{\Delta \mathrm{t}}, \tag{7}$$

where ζ denotes the scaling factor from px to mm.

The absolute bubble velocity, v_{b}, is calculated as the sum of the relative bubble velocity and the velocity of the linear unit drive, v_{lud}:

$$v_{\mathrm{b}} = v_{\mathrm{rel,b}} + v_{\mathrm{lud}}. \tag{8}$$

The position of the linear unit drive, $\mathrm{x_l}$, and the scaling factor is obtained by using the bars fixed on the column wall, as shown in Fig. 4(c). By performing a linear regression, the position of the bars, y_{bar}, is obtained for each image:

$$y_{\mathrm{bar}} = \zeta m_{\mathrm{bar}} + \mathrm{x_l}, \tag{9}$$

where m_{bar} is the number of bars present in the image. ζ and $\mathrm{x_l}$ are obtained as the coefficients from the linear regression.

The velocity of the linear unit drive is calculated as the ratio between the change in the position of the linear unit drive and the time between two consecutive frames:

$$v_{\mathrm{lud}} = \zeta \frac{\Delta x_{\mathrm{l}}}{\Delta \mathrm{t}}. \tag{10}$$

There is a time delay in the command signal sent from the computer software to the linear unit drive, and the time at which the command is actuated by the linear unit drive. To compensate for the time delay, the change in the bubble velocity is anticipated. The compensating velocity, v_{++}, is obtained by linear regression where a fraction of the previous bubble velocity is used. The time delay is further elaborated in Sec. IV C. Due to the limited range of view of camera II, a bubble easily moves out of the ROI. In an attempt to tune the bubble toward the center of the image, a second compensating velocity, denoted centering velocity, is introduced. The centering velocity, v_{c}, is found by estimating the required change in the linear unit drive velocity in order to tune the bubble toward the center of the image. The final velocity sent to the linear unit drive, v_{sp}, is calculated by Eq. (11),

$$v_{\mathrm{sp}} = v_{\mathrm{b}} + k_1 v_{\mathrm{c}} + k_2 \Delta v_{++}, \tag{11}$$

where k_1 and k_2 are controller constants. k_1 affects the velocity at which the bubble will move toward the center of the image. k_2 affects the compensation of the delay in the linear unit drive.

C. Processed data

The presence of a delay in the experimental setup results in a delay in the initial movement of the linear unit drive. In addition, the delay is reflected in a late adaption of the linear unit drive to a new set velocity. The combined effects of the dynamic bubble ascent and the delay in the linear unit drive result in an intricate system. The system acquires the ability to rapidly adjust to changes in the bubble velocity. During a bubble rise event, a data set is generated through camera II. The data set contains preliminary information about the bubble position, velocity, and size, in addition to the velocity of the linear unit drive. The preliminary information can be used to assess the correspondence between the velocities v_{b}, v_{lud}, and v_{sp}. In addition, the preliminary information can be employed to study the effect of adjusting the controller parameters, k_1 and k_2.

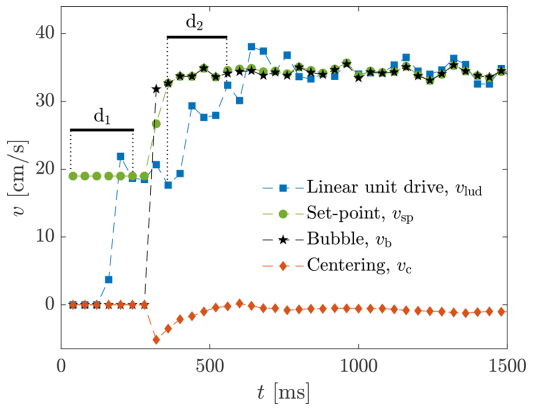

FIG. 5. Example of a delay in the actuation time of the linear unit drive, comparing the linear unit drive velocity, v_{lud}, the set velocity, v_{sp}, the centering velocity, v_c, and the velocity of the bubble, v_b.

Due to the delayed initial movement, the linear unit drive is activated prior to the injection of a bubble. In the example shown in Fig. 5, the linear unit drive is given an initial set velocity of $v_{sp} = 18$ cm/s. Note that the initial set velocity must be chosen depending on the initial bubble velocity. The velocity of the linear unit drive, v_{lud}, reaches the set-point velocity after six time-steps, noted by d_1 in Fig. 5. When the injected bubble reaches the ROI, the bubble velocity, v_b, is estimated, and a new set-point velocity is calculated. The set-point and bubble velocity are seen to correspond well in Fig. 5. The linear unit drive adapts to the new set-point velocity after six time-steps, noted by d_2 in Fig. 5. As the velocity of the linear unit drive increases above the bubble velocity, the centering velocity, v_c, is correcting by a negative value. To assess the average time delay in the adaption of the linear unit drive to the set-point velocity, 30 bubble rise events were evaluated. The average time delay is 250 ms. There is a significant correspondence between the bubble and set-point velocity, seen by the approximately overlapping velocities in Fig. 5. The delay in the actuation time of the linear unit drive is concluded to be mechanical.

V. IMAGE ANALYSIS OF BUBBLE PROPERTIES—CAMERA I

An in-house image processing algorithm in MATLAB (2020a) is used to determine the bubble properties from the images recorded by camera I. Prior to the computation of the bubble properties, the original images are processed. The image processing consists of the following steps: (1) image cropping, (2) subtraction of a background image, (3) binarization, (4) image filling, (5) image imcomplement, and (6) parameter extraction. The resulting images from the processing steps are shown in Fig. 6.

Image processing: Cropping (step 1)

The original grayscale image in Fig. 7(a) shows an ascending bubble, including the bars employed to determine the bubble velocity and position. A grayscale image contains pixels with values in the range of 0 to 255. An 8-bit representation is used, which means that the image is stored with 8 bits per sampled pixel.[53] In the first step of the image processing, the original image in Fig. 7(a) is cropped into two ROI. One ROI includes the bubble, shown in Fig. 7(b), and the second ROI includes the bars, shown in Fig. 7(c).

Image processing: Contrast enhancement (step 2)

All the elements that are not related to the bubble are removed. This is done by subtracting image (a) in Fig. 6 by a background image. The background image is calculated as the average of the bubble rise path. Figure 6(b) shows the result when the background image is subtracted by the current image. The complement of image (b) in Fig. 6 is computed using the MATLAB built-in function *imcomplement*. When complementing a grayscale image, the pixels are subtracted from the maximum pixel value. This results in the dark areas becoming brighter, and vice versa. The resulting complemented image is shown in Fig. 6(c).

Image processing: Binarization (step 3)

In a binary image, the pixels can take the value of 0 (black) or 1 (white). Prior to the binarization of a grayscale image, a threshold, T, is calculated. All the pixels with a value above the threshold are replaced by the value of 1, and all others are set to 0. In the present work, a threshold is calculated for each of the recorded images. For a bubble rise event containing 7000 images, 7000 corresponding threshold values are obtained. The thresholds are obtained by means of *graythresh*, a built-in MATLAB-function. *Graythresh* uses Otsu's method,[54] where the values are chosen to minimize the intraclass variance of black and white pixels. Conversion to a binary image is executed using the MATLAB built-in function *imbinarize*. The binarized image is shown in Fig. 6(d).

Determining a suitable threshold value is of crucial importance, as it determines the bubble edge. In Fig. 8(a), an original grayscale image of an ellipsoidal bubble is shown. To illustrate the transition from dark to brighter pixels on the bubble edge, an enlarged area of the ellipsoidal bubble is shown in Fig. 8(b). When an image is binarized, the threshold value will determine if a pixel on the bubble edge is associated with the bubble or the background. Figure 8(c) shows a bubble where the original (pink) and binarized (green) images have been joined, i.e., the binarized image is placed on top of the original. An enlarged part of the joined image is shown in Fig. 8(d). Comparing Figs. 8(b) and 8(d), the discarded pixels (pink) correspond to pixels which could be associated with both the bubble and the background. Assessing the discarded pixels on the bubble edge in Fig. 8(d), the major and minor axes lengths are well represented. The choice of threshold is further elaborated in Sec. V B.

Image processing: Filling (step 4)

Due to the illumination of the vertical column, a bright spot is present at the center of the bubble in Fig. 6(d). The spot is eliminated by setting all the relevant values to 0, using the MATLAB built-in function *bwareaopen*. *bwareaopen* removes all the connected objects, which contain less than a specific number of pixels. The resulting filled bubble is shown in Fig. 6(e).

Image processing: Imcomplement (step 5)

The bubble parameters are extracted by using the MATLAB built-in function *regionprops*. *regionprops* calculates the properties of an object by regarding connected pixels of value 1. The bubble in Fig. 6(e) is defined by zero-valued pixels. Thus, the image needs to be complemented prior to the extraction of the bubble parameters. Black and white areas in the binary image are switched by using the function *imcomplement*, as in step 2 of the image processing. The resulting image of a white bubble with a black background is shown in Fig. 6(f).

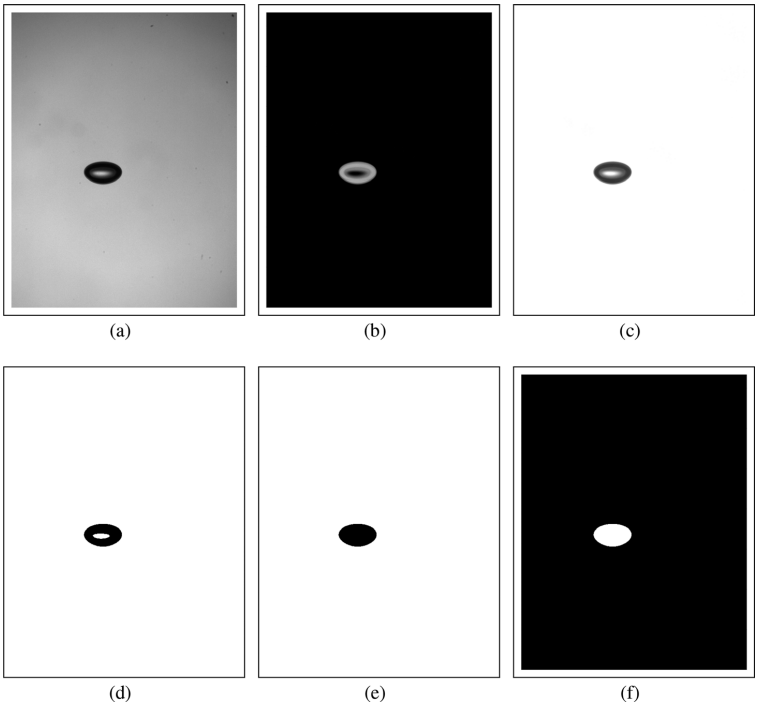

FIG. 6. Example of resulting images after handled by the image processing algorithm in MATLAB (2020a). Images (a)–(f) are obtained in image processing steps 1–6, respectively.

Image processing: Parameter extraction (step 6)

The bubble area (number of pixels defining the bubble), centroids (x,y-position), and major and minor axes lengths are calculated by using the function *regionprops*. For larger bubbles where the shape largely deviates from a spherical or ellipsoidal shape, determining the bubble diameter, aspect ratio, and the terminal velocity based on 2D images is challenging. This is particularly demanding when analyzing bubbles that exhibit significant bubble shape oscillations, and where the bubble rise paths are observed to be zigzag or helical. In the studies of Okawa *et al.*,[19] Celata *et al.*,[20] Liu *et al.*,[24] and Yan *et al.*,[26] bubble data obtained by image acquisition from one- and two sides of a bubble were compared. The bubble data generated from one side of the bubble were found to sufficiently approximate the actual process within an error of ±10%. The bubbles observed by Okawa *et al.*,[19] Celata *et al.*,[20] Liu *et al.*,[24] and Yan *et al.*[26] were equal or larger in size than those analyzed in the present work. Hence, evaluating the bubble properties based on images recorded from one direction is considered to be sufficient for the present experimental work.

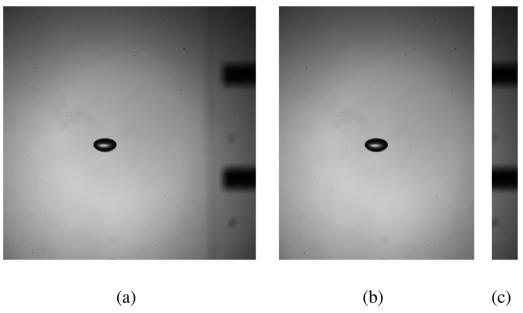

FIG. 7. (a) original image of an ellipsoidal air bubble in water, as recorded by camera I, (b) cropped ROI including the bubble, (c) cropped ROI including the bars.

A. Analysis of bubble properties: Bubble velocity

The bubble velocity is calculated by Eqs. (12)–(16),

$$v_{b,k} = \frac{\sqrt{(\Delta y_{bar} - \Delta y_b)^2 + (\Delta x_{bar} - \Delta x_b)^2}}{\Delta t}, \tag{12}$$

$$\Delta y_b = y_{b,k+1} - y_{b,k}, \tag{13}$$

$$\Delta x_b = x_{b,k+1} - x_{b,k}, \tag{14}$$

$$\Delta y_{bar} = y_{bar,k+1} - y_{bar,k}, \tag{15}$$

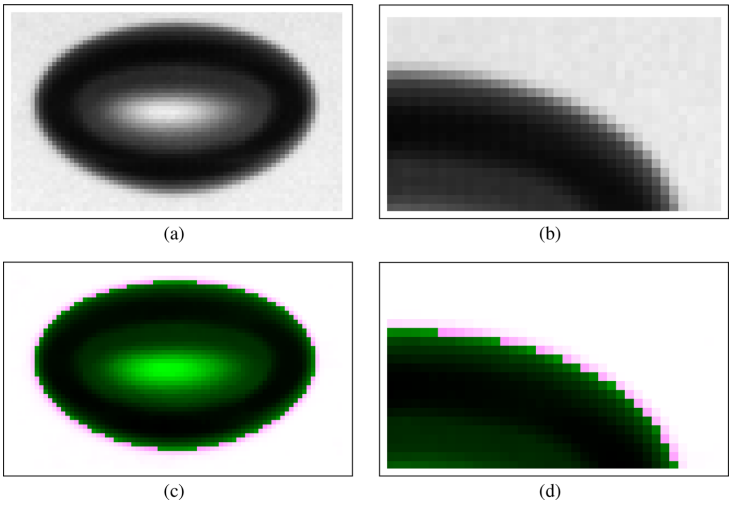

FIG. 8. (a) original image of an ellipsoidal bubble, (b) enlarged region of the original image, (c) joined original (pink) and binarized (green) image, (d) enlarged region of the joined original and binarized image.

$$\Delta x_{\mathrm{bar}} = x_{\mathrm{bar,k+1}} - x_{\mathrm{bar,k}}, \tag{16}$$

where Δy_{bar}, Δy_{b} and Δx_{bar}, Δx_{b} are the changes in the bar and bubble epicenter between two consecutive images in y- and x-direction, respectively. $\Delta t = t_{\mathrm{k+1}} - t_{\mathrm{k}}$ is the time step.

Figure 9 illustrates the change in position of the bars and the bubble between two consecutive images. Due to the mechanical delay in the linear unit drive, the adaption to a new set velocity may be delayed. This can result in the bubble moving away from the center or out of the image. Thus, the change in position of the bubble and bars in Fig. 9 depends both on the velocity of the bubble and the linear unit drive.

The procedure for calculating the terminal velocity is illustrated in Fig. 10. The term bubble velocity, denoted v_{b}, is used here for the instantaneous bubble velocity, whereas the term terminal velocity, denoted v_{T}, describes the time averaged bubble velocity in which only the vertical component of the velocity vector is considered. The presented experimental results on the terminal velocity are average values based on multiple bubble rise events. Typically, $N = 10$–20 bubble rise events are considered when calculating the average terminal velocity. The number of necessary bubble rise events is statistically evaluated in Sec. VII E. As a needle may produce bubbles of slightly different size, the bubbles are grouped according to their initial size. The bubble velocity in Fig. 10 is a mean value based on 22 independent bubble rise events, with a mean bubble diameter $d_{\mathrm{b}} = 1.15$ mm. Hence, the z-axis in Fig. 10 represents an approximated position for the mean bubble velocity. Instantly after the bubble detaches from the needle, it accelerates and an increase in the bubble velocity is observed. In this work, it is the terminal velocity that is of interest, and the first part of the bubble velocity profile in Fig. 10 is therefore neglected. When a force balance is obtained, the bubble reaches a terminal velocity, estimated by linear regression over the inspected time interval. Reaching the top of the column, the bubble moves out of the image. Hence, the bubble velocity data from the upper part of the column are neglected. The inspected time interval is manually determined for each of the bubble rise events.

B. Analysis of bubble properties: Bubble diameter

The volume equivalent bubble diameter, d_{b}, is calculated from the projected area and the minor and major axes of an ellipsoid, under the assumption of an oblate spheroid:

$$d_{\mathrm{b}} = \sqrt[3]{(2b)^2 \times (2a)}, \tag{17}$$

where $A = 2a$ and $B = 2b$ are the minor (vertical) axis and major (horizontal) axis, respectively. For a spherical bubble, the minor axis and major axis equals, and Eq. (17) reduces to that of a sphere.

A sensitivity analysis was performed to assess the influence of the threshold value on the calculated bubble diameter. In the sensitivity analysis, seven threshold values were evaluated. The influence of the threshold on the bubble diameter is illustrated in Fig. 11. Six values, $T \in [0.55, 0.90]$, were held constant for all time instants during the image processing. The relative difference in the calculated average bubble diameter when using $T = 0.55$ and $T = 0.9$ is 6 %. In addition, a threshold, denoted local threshold, was calculated for all time instants. A local threshold will capture potential changes in the illumination along the vertical column. The variation in the calculated local threshold as a function of time is shown in Fig. 11.

The original and binarized images for the various thresholds were joined, as illustrated in Fig. 8. Assessing the joined images revealed misrepresented pixels on the bubble edge. The bubble diameter was underestimated for $T = 0.55$ and overestimated for $T = 0.90$. When using $T = 0.90$, all the pixels associated with the bubble were

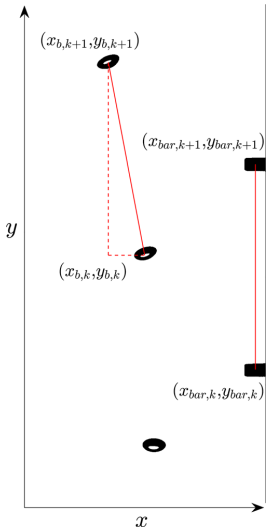

FIG. 9. Change in the vertical and horizontal position of the bars and the bubble between image k and $k+1$.

included. However, $T = 0.90$ resulted in the inclusion of pixels associated with shadows on the bubble edge due to curvature. Approximately the same values of the characteristic lengths of the bubble were obtained when using a local threshold and $T = 0.90$. However, pixels associated with shadows on the bubble edge were not included when using a locally calculated threshold. Based on the visual

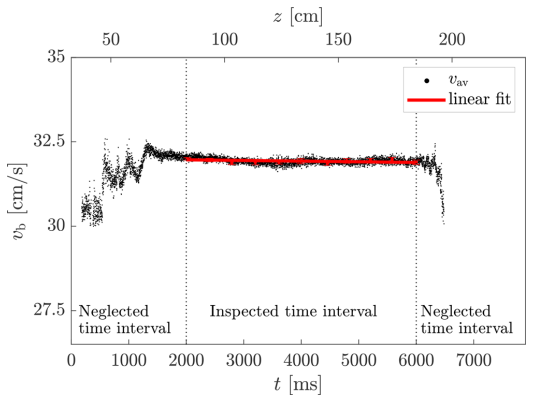

FIG. 10. Procedure for calculating the terminal velocity. The bubble velocity in the specific example is based on 22 bubble rise events, with a mean bubble diameter of $d_b = 1.15$ mm.

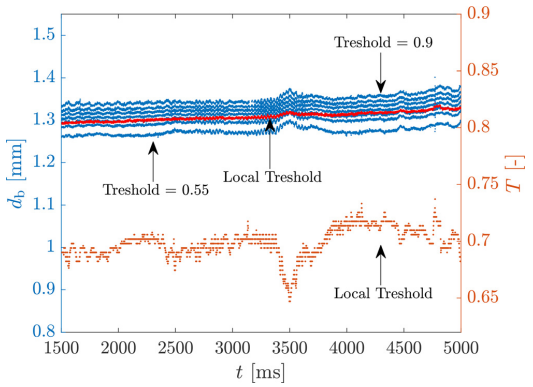

FIG. 11. Calculated volume equivalent bubble diameter as function of time, using $T \in [0.55, 0.90]$ and a local threshold.

inspection of the joined images, a local threshold gives the most accurate representation of the bubble edge. The uncertainties in the major axis and minor axis are assumed to be ± 1 px based on the visual assessment of the joined images.

C. Threshold bars

The images containing bars were given a separate threshold value in the binarization. Due to the bars being located at a focal plane out of focus, as shown in Fig. 7(c), an accurate representation of the bars' position is challenging. Calculating the threshold by use of the MATLAB built-in function *graytresh* gave an inaccurate representation of the bars. The *graytresh* function included regions that were not associated with the bars. When measuring the displacement between two consecutive images, the center position of the bars is being measured. The influence of the bars, being out of focus, on the measured center position was quantitatively and visually evaluated. If the gray tones were equally spaced above and below the bars, the measured center position was unaffected. This requirement was met by determining an appropriate threshold value. The value was chosen by assessing the original and binarized images when using various threshold values. Three independent experimental events were evaluated using seven different threshold values. Figure 12 illustrates the effect for one of the experimental events. Lower values, $T \in [0.65, 0.80]$, resulted in scattering bubble velocity data. The original and binarized images were joined when using $T \in [0.65, 0.80]$, which revealed the inclusion of darker areas not associated with the bars. Using higher values, $T \in [0.85, 0.95]$, parts of the gray-scale areas associated with the bars were discarded. The edges of the bars were defined and clear when using $T \in [0.85, 0.95]$. In the algorithm, a bar is evaluated when present within a certain vertical range. The vertical limits are chosen to ensure that at least one of the present bars is being evaluated. The presence of at least two bars in the image assures that a bar is always within the vertical range.

The calculated bubble velocity was compared at four heights along the vertical column, using $T = [0.85, 0.9, 0.95]$. The largest

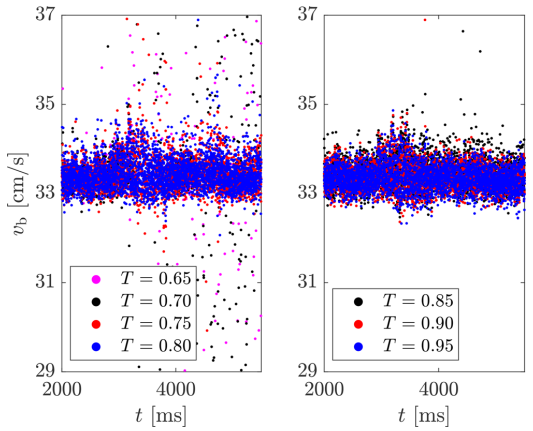

FIG. 12. Influence of varying threshold values used in the image processing of the bars on the calculated bubble velocity.

relative difference in the bubble velocity between the heights was 0.3% for $T = 0.85$, 0.3% for $T = 0.9$, and 0.2% for $T = 0.95$. In the present work, the bubble velocity range is $v_b \in [12, 39]$ cm/s. While $T \geq 0.85$, the choice of threshold value has negligible effect on the calculated bubble velocity.

VI. STATISTICAL DATA TREATMENT

The experimental data may be subject to several sources of error associated with the experimental setup and image analysis. Random errors are reflected in the standard deviation and the confidence interval of the experimental data.

When measurements can be repeated several times, and the associated uncertainties are known to be random, the uncertainty in a quantity can be estimated by examining the spread in the calculated data. In the present work, the calculated quantities are average values of multiple experimental events. The mean, $\bar{x}$, and the sample standard deviation, S, can be calculated by the general formulas given in Appendix B.[55]

Calculating the bubble velocity and diameter involves two steps. First, the quantities that are possible to measure, e.g., bubble position and axes lengths, are measured. Second, the quantities of interest, e.g., the terminal velocity and bubble diameter, are calculated based on the measurements. The uncertainty in the calculated quantity is a function of the uncertainties of the directly measured quantities. The uncertainties in the directly measured quantities propagate through the calculation to produce the uncertainty in the final calculated quantity (Taylor[55]). For a parameter Y, as function of n measured independent variables $(y_1, \ldots, y_n)$ whose uncertainties $\delta y_1, \ldots, \delta y_n$ are small, that is, $Y = f(y_1, y_2, \ldots, y_n)$, the uncertainty can be found by the multivariate propagation of error formula in Eq. (18) (Ref. 56),

$$(\delta Y)^2 = \left(\frac{\partial Y}{\partial y_1}\delta y_1\right)^2 + \left(\frac{\partial Y}{\partial y_2}\delta y_2\right)^2 + \cdots + \left(\frac{\partial Y}{\partial y_n}\delta y_n\right)^2, \quad (18)$$

where the uncertainty of each variable is represented by $\delta y_1, \ldots, \delta y_n$. Note that the variables in Eq. (18) are assumed to be independent, i.e., the covariances between the variables are zero. The uncertainty obtained by Eq. (18), δY, is the absolute uncertainty of Y. The relative uncertainty can be found by dividing δY by the value of Y.

If the uncertainty can be calculated by both the propagation of errors and by regarding the standard deviation of the mean from multiple experimental runs, both methods should be applied and compared (Taylor[55]). The two methods should give approximately the same values:

Terminal velocity

The instantaneous bubble velocity can be formulated as

$$v_{b,k} = \frac{s}{\Delta t}\sqrt{\left[(P_{ybar,k+1} - P_{ybar,k}) - (P_{yb,k+1} - P_{yb,k})\right]^2 + \left[(P_{xbar,k+1} - P_{xbar,k}) - (P_{xb,k+1} - P_{xb,k})\right]^2}, \quad (19)$$

where $s = h_{cal,m}/h_{cal,px}$ denotes the scaling factor from unit pixels to unit length, $h_{cal,m}$ and $h_{cal,px}$ are the widths in units of length and pixels, respectively, Δt the time step between two consecutive images, and $P_{ybar,k+1}$, $P_{ybar,k}$, $P_{yb,k+1}$, and $P_{yb,k}$ refer to the position in y-direction of the evaluated bar and bubble at image number $k+1$ and k. $P_{xbar,k+1}$, $P_{xbar,k}$, $P_{xb,k+1}$, and $P_{xb,k}$ refer to the position in x-direction of the evaluated bar and bubble at image number $k+1$ and k. P is given in unit of pixels.

The absolute random uncertainty in the terminal bubble velocity, $\delta v_{T,r}$, can be calculated from the propagation of error in Eq. (18) and the instantaneous bubble velocity in Eq. (19), where the latter equation is reduced to only contain the vertical component y. The relative uncertainty can be found by dividing Eq. (20) by the terminal velocity. The partial derivatives in Eq. (20) are derived in Appendix C.

$$\delta v_{T,r} = \left[\left(\frac{\partial v_b}{\partial P_{ybar,k+1}}\delta P_{ybar,k+1}\right)^2 + \left(\frac{\partial v_b}{\partial P_{ybar,k}}\delta P_{ybar,k}\right)^2 + \left(\frac{\partial v_{yb}}{\partial P_{yb,k+1}}\delta P_{yb,k+1}\right)^2 \left(\frac{\partial v_b}{\partial P_{yb,k}}\delta P_{yb,k}\right)^2 + \left(\frac{\partial v_b}{\partial \Delta t}\delta \Delta t\right)^2\right]^{1/2}, \quad (20)$$

where $\delta P_{ybar,k+1}$ and $\delta P_{ybar,k}$ are the uncertainties in the bar position in y-direction at image number $k+1$ and k, $\delta P_{yb,k+1}$ and $\delta P_{yb,k}$ the uncertainties in the bubble position in y-direction at image number $k+1$ and k, and $\delta \Delta t$ the uncertainty in the time step between two consecutive images.

The vertical displacement of the bubble and the bars in Eq. (20) are considered over the time interval over which the terminal velocity

is calculated. Thus, the displacement is considered over multiple images.

Bubble diameter

The absolute random uncertainty in the bubble diameter, $\delta d_{b,r}$, is calculated by Eq. (21). The relative random uncertainty can be obtained by dividing Eq. (21) by the bubble diameter. The partial derivatives in Eq. (21) are derived in Appendix C.

$$\delta d_{b,r} = \sqrt{\left(\frac{\partial d_b}{\partial A}\delta A\right)^2 + \left(\frac{\partial d_b}{\partial B}\delta B\right)^2}, \tag{21}$$

where δA and δB denote the uncertainties in the minor and major axes lengths, respectively.

Note that the minor and major axes lengths are taken to be mean values over the corresponding time interval over which the terminal velocity is calculated.

A. Uncertainty in the scaling factor

A rectangular glass pin marked with a horizontal line is used to obtain the scaling factor from unit pixels (px) to unit length (mm). The length of a pixel is calculated from the number of pixels and the width in unit length of the horizontal line on the glass pin. The uncertainty in the px-to-mm scaling factor arises from the uncertainty in the measurement of the calibration pin in unit pixels, $\delta h_{cal,px}$, and the uncertainty in the measurement in unit length, $\delta h_{cal,m}$. It is assumed an uncertainty of ± 0.5 px on each side of the rectangular pin, i.e., $\delta h_{cal,px} = \pm 1$ px. Digital equipment (Mitutoyo digital ABS Caliper CoolantProof IP67) was used to measure the width of the calibration pin in unit length. The uncertainty in the digital equipment is reported by the producer to be $\delta h_{cal,m} = \pm 0.02$ mm. The depth at which the calibration pin is measured corresponds to that at which the bubbles are produced.

The uncertainty in the px-to-mm scaling factor can be calculated from the propagation of error formula in Eq. (18).[55] The contribution from the uncertainty in the px-to-mm scaling factor to the absolute random uncertainty in the terminal velocity, $\delta v_{T,c}$, and the bubble diameter, $\delta d_{b,c}$, are given by Eqs. (22) and (23) as follows:

$$\delta v_{T,c} = \sqrt{\left(\frac{\partial v_b}{\partial h_{cal,m}}\delta h_{cal,m}\right)^2 + \left(\frac{\partial v_b}{\partial h_{cal,px}}\delta h_{cal,px}\right)^2}, \tag{22}$$

$$\delta d_{b,c} = \sqrt{\left(\frac{\partial d_b}{\partial h_{cal,m}}\delta h_{cal,m}\right)^2 + \left(\frac{d_b}{\partial h_{cal,px}}\delta h_{cal,px}\right)^2}. \tag{23}$$

The total random uncertainties in the terminal velocity and the bubble diameter are given by Eqs. (24) and (25):

$$\delta v_{T,tot} = \sqrt{\delta v_{T,r}{}^2 + \delta v_{T,c}{}^2}, \tag{24}$$

$$\delta d_{b,tot} = \sqrt{\delta d_{b,r}{}^2 + \delta d_{b,c}{}^2}. \tag{25}$$

It should be noted that the uncertainty in the px-to-mm scaling factor is explicitly accounted for when employing the propagation of error formula in Eq. (18), which is not the case when the uncertainty is calculated from the repeat of measurements in Eq. (33).

TABLE VI. Values used to calculate the uncertainties in the bubble velocity and diameter.

Parameter	Unit	Value
ΔP_{ybar}	px	9–18
ΔP_{yb}	px	0.3–0.6
Δt	s	10^{-3}
$h_{cal,m}$	mm	3.77
$h_{cal,px}$	px	154–194
A	px	38–61
B	px	39–111
δP_{bar}	px	± 1
δP_b	px	± 1
$\delta h_{cal,m}$	mm	± 0.02
$\delta h_{cal,px}$	px	± 1
$\delta \Delta t$	s	$\pm 10^{-6}$
δA	px	± 1
δB	px	± 1

The values applied to calculate the uncertainties in the terminal velocity and the bubble diameter are given in Table VI.

VII. RESULTS AND DISCUSSION

A. Bubble rise velocity

Instantly after a bubble detaches from the needle, the bubble accelerates until buoyancy, gravity, and drag forces are balanced, and the terminal velocity is reached. In Fig. 13, the bubble velocity as a function of time is plotted for bubbles of volume equivalent diameter $d_b = 1.15, 1.28,$ and 1.77 mm. Initially, there is a spatial distance between the two cameras and the injected bubble. This is due to the linear unit drive being activated prior to the injection of a bubble, as discussed in Sec. IV C. Additionally, there are small variations in the needle detachment time. The bubble is therefore captured by camera I

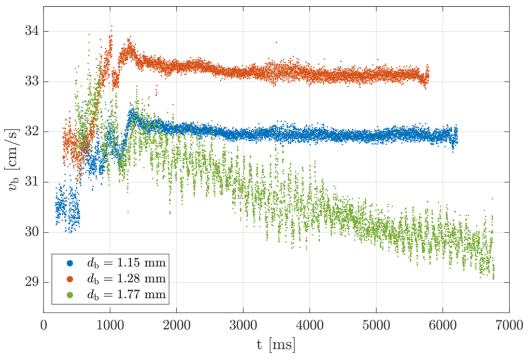

FIG. 13. Instantaneous bubble velocity vs rise time for bubbles of volume equivalent diameter $d_b = 1.15, 1.28, 1.77$ mm.

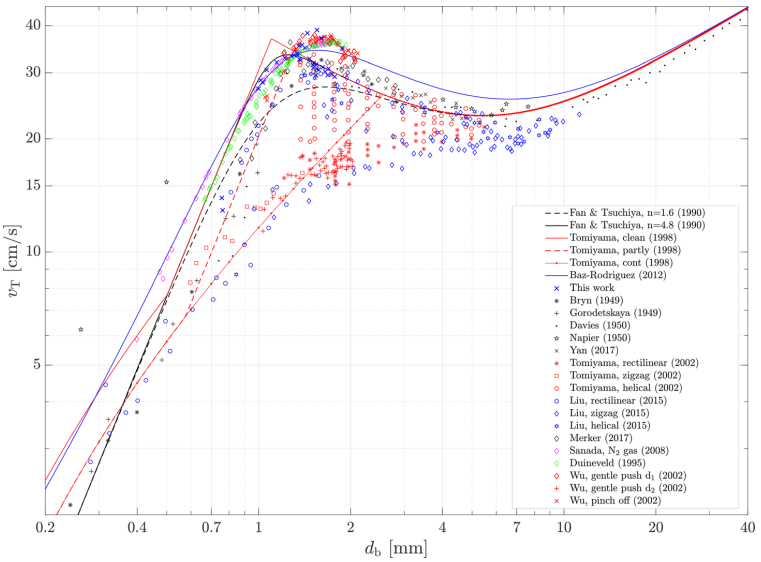

FIG. 14. Terminal velocity as function of bubble diameter, including experimental data and correlations found in the literature.

at $t > 0$, and the total bubble recording time varies for the individual bubble events. The bubbles with $d_b = 1.15$ and $d_b = 1.28$ mm in Fig. 13 are close to spherical in shape and rise in rectilinear paths. Due to the initial acceleration, the bubble velocities increase before reaching terminal values at approximately 1600 ms in both cases. As a result of the reduction in the hydrostatic pressure over the column height and a net-zero mass transfer, an increase in the bubble size is observed for all the bubble rise events. The ellipsoidal bubble of size $d_b = 1.77$ mm takes an oscillating rise path, resulting in a periodic fluctuating terminal velocity. Reflecting the increase in the bubble volume over the column, the amplitude of the path oscillations of $d_b = 1.77$ mm increases; hence, the terminal velocity decreases.

Including empirical data from the literature, Fig. 14 reveals a large scatter in the terminal velocities. As described in Sec. I A, the scatter has been attributed to both the purity of the liquid and the method of bubble formation. In the present work, a small scatter in the terminal velocities is observed for bubbles of comparable size. Comparing to the data by Tomiyama *et al.*,[18] Liu *et al.*,[25] and Wu and Gharib,[32] where bubbles have been produced by different methods, the small scatter in the present data indicates consistency in the method of bubble formation. This observation is of importance, as the needles are handmade and small variations in the design are unavoidable. With the inner diameter of the needle being smaller than the bubble diameter in all the experimental events, the bubbles are produced with large initial bubble shape deformations. For bubbles with a diameter smaller than the bubble formation device, the terminal velocity data obtained in this work coincide with the data by Tomiyama *et al.*,[18] Liu *et al.*,[25] and Wu and Gharib.[32] Second, the terminal velocities from the present work coincide with the data by Duineveld,[31] Sanada *et al.*,[22] and Wu and Gharib,[32] which have been obtained in ultra-purified water. This indicates that the de-ionized water employed in the present work can be regarded as pure.

As previously mentioned in Sec. II A, only the vertical bubble velocity component is considered when calculating the terminal

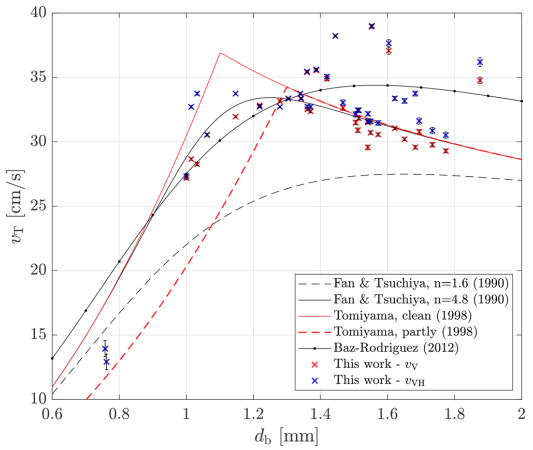

FIG. 15. Terminal velocity calculated by the vertical bubble velocity component, v_V, and the vertical and horizontal velocity component, v_{VH}, including the standard deviations and correlations found in the literature.

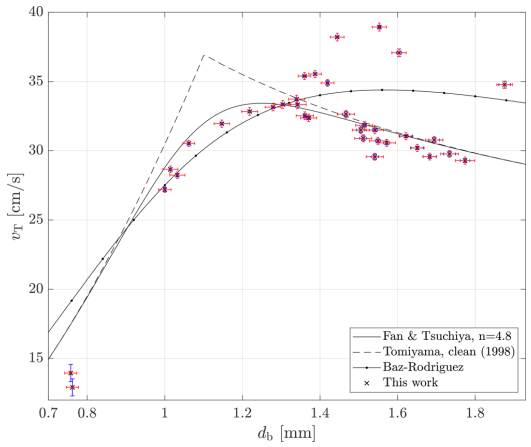

FIG. 16. Terminal velocity as function of bubble diameter, including experimental data, corresponding standard deviations, and correlations found in the literature. The standard deviations calculated from the propagation of error method are shown in red, and the standard deviations of the means are shown in blue.

velocity. Contradictory to most work reported in the literature, Liu *et al.*[25] and Yan *et al.*[26] (data are included in Fig. 14), considered both the vertical and the horizontal velocity components when calculating the terminal velocity. The different definitions used in the literature for the terminal velocity may contribute to the large data scatter in Fig. 14. Thus, to analyze the significance of including the horizontal velocity component in the calculation of the terminal velocity, both methods are considered in the present work and compared in Fig. 15. As expected, the terminal velocities calculated by the two methods are approximately equal for bubbles taking a rectilinear path. The onset to path oscillations is observed for bubbles in the size range $d_b \in [1.3, 1.56]$ mm, and thus, with increasing path oscillations, the influence of the horizontal velocity component becomes more significant which results in a larger terminal velocity than otherwise is obtained with the traditional definition of the terminal velocity. The maximum deviation between the two methods for computing the terminal velocity is 4% in the present work.

TABLE VII. Minimum and maximum standard deviations of the mean along with the terminal velocity and the bubble diameter.

	Terminal velocity (cm/s)	Bubble diameter (mm)
Min	35.4 ± 0.1	1.000 ± 0.001
Max	13.9 ± 0.6	1.68 ± 0.02

Figure 16 shows the terminal velocity as function of the bubble diameter, including the corresponding standard deviations, which have been calculated by both the propagation of error in Eq. (18) and the standard deviation of the mean in Eq. (B3). Comparing the uncertainties in Fig. 16, the two methods of calculation are seen to give close to equal values. This is in accordance with the textbook of Taylor.[55]

The minimum and maximum standard deviation of the mean, along with the terminal velocity and the bubble diameter, are given in Table VII. The deviation from the terminal velocity is in the range of $[0.3, 4]$%, and the deviation from the mean bubble diameter is in the range of $[0.1, 1]$%.

In three particular cases, specifically for $d_b = 1.44$, $d_b \in [1.55, 1.60]$, and $d_b = 1.88$ mm, the terminal velocities are considered to be high. Assessing the trajectories, a rectilinear rise path is observed for $d_b = 1.44$ mm, whereas oscillating rise paths are seen for $d_b \in [1.55, 1.60]$ and $d_b = 1.88$ mm. The calculated terminal velocities are based on 20, 10, and 12 bubble events, for $d_b = 1.44$, $d_b \in [1.55, 1.60]$, and $d_b = 1.88$ mm, respectively. Statistically, the three cases are found to be significant, shown by the low standard deviations in Fig. 16. In particular, for $d_b = 1.44$ mm, the standard deviation of the terminal velocity and the bubble diameter are 0.5 and 0.02, respectively. Assessing the original images and the calculated bubble properties reveals no obvious explanation for the relatively high values. At present, the higher data values are considered to be a result of the method of bubble formation.

TABLE VIII. Statistics of model performance on the terminal velocity, where the number of measurements $M = 35$.

	$d_b < 1.3$ mm			$d_b > 1.3$ mm			$d_b \in [0.76, 1.88]$ mm		
Correlation	ϵ	σ_e	c	ϵ	σ_e	c	ϵ	σ_e	c
Mendelson[16]	0.29	0.25	−0.98	0.05	0.07	0.24	0.11	0.17	−0.69
Fan, n = 1.6[36]	0.24	0.07	0.81	0.22	0.09	−0.34	0.23	0.09	−0.13
Fan, n = 4.8[36]	0.07	0.09	−0.89	0.05	0.07	0.24	0.06	0.08	−0.18
Jamialahmadi[45]	0.23	0.22	−0.97	0.06	0.08	0.26	0.10	0.15	−0.61
Baz-Rodriguez[23]	0.08	0.13	−0.85	0.07	0.04	0.68	0.07	0.07	−0.18
Tomiyama, clean[17]	0.13	0.07	−0.91	0.05	0.07	0.24	0.07	0.08	−0.39
Tomiyama, partly[17]	1.09	0.39	0.82	0.05	0.07	0.24	0.09	0.12	−0.50
Tomiyama, v = f(E)[18]	0.07	0.05	−0.69	0.06	0.08	0.22	0.06	0.07	−0.02

B. Analysis of correlations for the terminal velocity

The predictability of the correlations for the terminal velocity given in Tables III and IV was analyzed. This was done by comparing the relative error, e, the standard deviation of the error, σ_e, and the correlation factor, c, given by Eqs. (A1)–(A5) in Appendix A. In addition, the predictability was evaluated by using Figs. 22 and 23 in Appendix A, where the ratio of the predicted and the measured terminal velocity is plotted as a function of Eötvös number. The correlation factor, which indicates the strength of correlation between the experimental- and the correlation-based values, should be close to zero. A positive correlation factor indicates an overprediction, a negative correlation factor indicates an underprediction, whereas a zero-valued correlation factor indicates no linear relationship. Interpreted for this

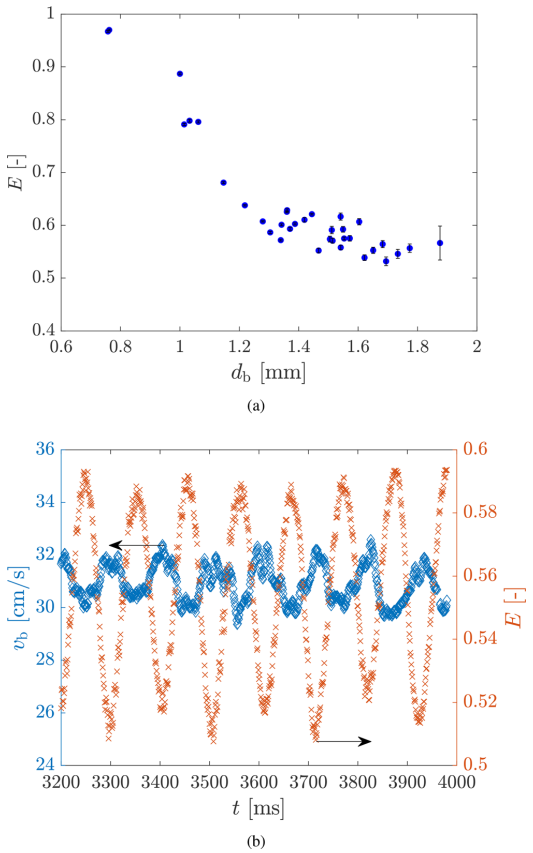

FIG. 17. (a) Bubble aspect ratio as function of bubble diameter, including standard deviations, (b) bubble velocity and aspect ratio as function of time for a bubble $d_b = 1.66$ mm.

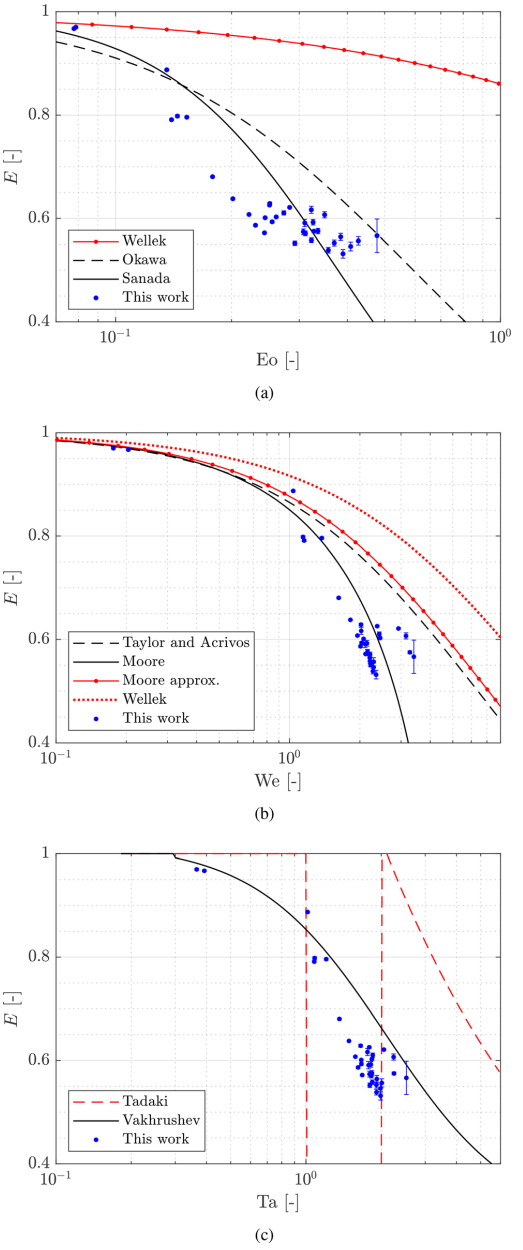

FIG. 18. Bubble aspect ratio as function of (a) Eötvos number, (b) Weber number, and (c) Tadaki number, including mean experimental values and available correlations.

specific case, a positive correlation factor indicates that the correlation tends to overpredict the experimental data with increasing bubble diameter, whereas the correlation tends to underpredict the data with decreasing bubble diameter. A negative correlation factor indicates the opposite. In Fig. 22, the correlation proposed by Mendelson[16] is seen to strongly overestimate the experimental data for Eo < 0.23. The correlation factor is $c = -0.98$. Statistical values of the correlations showing high predictability are given in Table VIII.

Large changes in the bubble dynamics are observed around the terminal velocity peak in Fig. 14. When validating correlations for the terminal velocity against experimental data, Celata *et al.*[21] suggested subdividing the evaluation into two size regions. Celata *et al.*[21] proposed the size regions $d_b < 1.3$ and $d_b > 1.3$ mm. The statistical values presented in Table VIII are calculated with and without subdividing the validation into the size regions suggested by Celata *et al.*[21] The number of experimental events used in the analysis is $M = 35$. Note that these values are average values based on N individual bubble rise events. Evaluating the bubbles with diameter $d_b < 1.3$ mm, the correlation by Tomiyama *et al.*,[18] given in Table III, gives the best prediction. The standard deviation and relative error when using the correlation by Tomiyama *et al.*[18] is $\sigma_e = 0.05$ and $\epsilon = 0.07$, respectively. The correlation by Fan and Tsuchiya[36] using n =4.8, given in Table III, predicts the experimental data well. The calculated standard deviation is $\sigma_e = 0.09$ and the relative error is $\epsilon = 0.07$. However, as seen in Fig. 22, the correlation by Fan and Tsuchiya[36] overestimates the data for Eo < 0.1.

For bubbles with diameter $d_b > 1.3$ mm, the correlations by Fan and Tsuchiya[36] (using n = 4.8), Tomiyama *et al.*,[17] Mendelson,[16] and Tomiyama *et al.*,[18] give good predictions. Except for a slightly higher correlation factor, the performance of the correlation proposed by Mendelson[16] is close to those by Fan and Tsuchiya,[36] Tomiyama *et al.*,[17] and Mendelson.[16] Regarding Figs. 22 and 23, the correlations by Fan and Tsuchiya,[36] Tomiyama *et al.*,[17] Mendelson,[16] Mendelson,[45] and Tomiyama *et al.*,[18] underestimate the same experimental data points. These data points are the high valued terminal velocities discussed in Sec. VII A.

The correlation by Tomiyama *et al.*[18] shows a high predictability when evaluating the experimental data without subdividing the evaluation into size regions. The statistical parameters when employing the correlation by Tomiyama *et al.*[18] were calculated to be $\sigma_e = 0.07$, $\epsilon = 0.06$, and $c = -0.02$.

C. Bubble aspect ratio

In Fig. 17(a), showing the bubble aspect ratio as a function of the bubble diameter, close to a linear decrease in the bubble aspect ratio is seen for $d_b < 1.3$ mm. Note that due to small values, some of the standard deviations plotted in Fig. 17(a) are not visible. For bubble diameter $d_b > 1.3$ mm, a spread in the bubble aspect ratio is observed. A similar trend was observed in the studies of Celata *et al.*,[21] Celata *et al.*,[20] and Liu *et al.*,[25] where a significant scatter in the bubble aspect ratio was observed for bubbles of size $d_b > 1$ mm. Reflecting the dynamic bubble behavior, Fig. 17(b) shows an inverse correlation between the instantaneous bubble velocity and the bubble aspect ratio for an oscillating bubble of size $d_b = 1.66$ mm. When the bubble velocity is high, the bubble aspect ratio is low, and vice versa. The observed dependency between the bubble velocity and aspect ratio confirms the earlier observations by Tomiyama *et al.*,[18] Celata *et al.*,[20,21] and Liu *et al.*[25]

The bubble aspect ratio was correlated as a function of the Eötvös, Weber, and Tadaki numbers. The correlations employed are

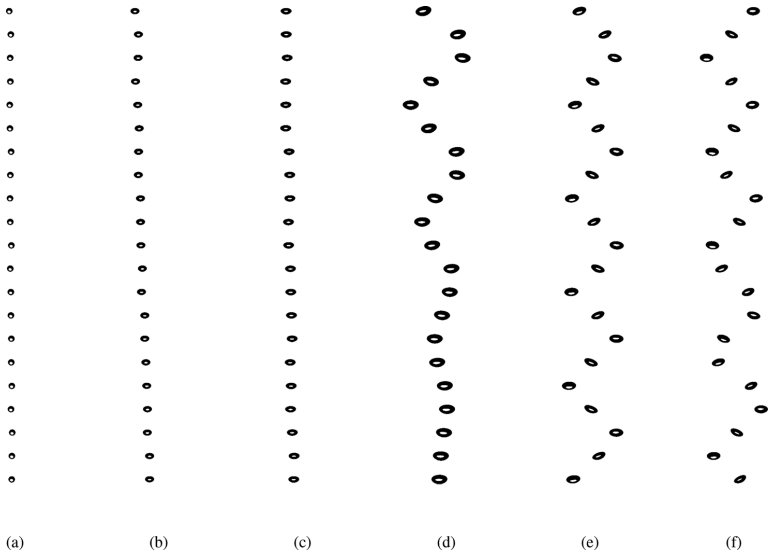

FIG. 19. Trajectory of various bubble sizes; (a) $d_b = 0.76$, (b) $d_b = 1.14$, (c) $d_b = 1.31$, (d) $d_b = 1.56$, (e) $d_b = 1.65$, and (f) $d_b = 1.75$ mm. Multimedia views: https://doi.org/10.1063/5.0061581.1; https://doi.org/10.1063/5.0061581.2; https://doi.org/10.1063/5.0061581.3; https://doi.org/10.1063/5.0061581.4; https://doi.org/10.1063/5.0061581.5; https://doi.org/10.1063/5.0061581.6

presented in Table V and Eqs. (4)–(6) in Sec. II. In Fig. 18(a), the data are correlated as a function of the Eötvös number. The bubble aspect ratio is seen to be overestimated by all the selected expressions for Eö ≤ 0.3, where the correlation by Wellek *et al.*[50] overestimates over the entire region. For $0.3 < \text{Eö} < 0.5$, the correlation proposed by Okawa *et al.*[19] serves as an upper boundary for the bubble aspect ratio, while the correlation of Sanada *et al.*[22]—as a lower boundary. Expressing the bubble aspect ratio in terms of the Weber number, the experimental data in Fig. 18(b) are less scattered compared to the data in Fig. 18(a). Except from the high values of the bubble aspect ratio around We $=3$, the correlation by Moore[49] gives a fairly good estimate of the bubble aspect ratio. Note that these high values of the bubble aspect ratio correspond to the high terminal velocities discussed in Sec. VII A. For Weber numbers We > 1 in Fig. 18(b), the correlations by Taylor and Acrivos[57] and Wellek *et al.*,[50] in addition to the approximated correlation by Moore,[49] are seen to overpredict the experimental data.

In Fig. 18(c), the bubble aspect ratio is expressed as function of the Tadaki number. For increasing Tadaki numbers, the correlation by Vakhrushev and Efremov,[52] given by Eq. (6), overestimates the data. The correlation by Tadaki and Maeda[51] in Eq. (5) clearly fails to predict the bubble aspect ratio in Fig. 18(c).

D. Bubble trajectory

Binarized image sequences of the bubble trajectories for bubbles with $d_b = 0.76$ to $d_b = 1.75$ mm are shown in Fig. 19 (Multimedia view). The time interval between two consecutive images in Fig. 19 is 50 ms. Note that the optical resolution employed is not equal for all the illustrations in Fig. 19. The spherical and ellipsoidal bubbles in Figs. 19(a)–19(c) rise in rectilinear paths. The bubble diameter at which path oscillations start to develop has been observed to vary in the present study, as discussed in Sec. VII A. Considering the influence

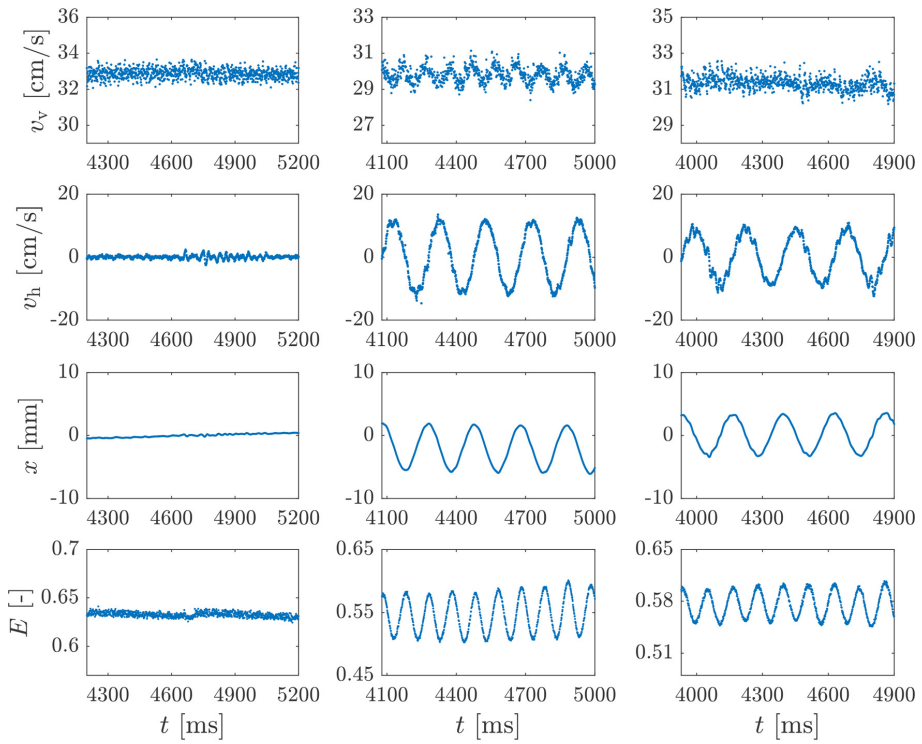

FIG. 20. Horizontal (v_h) and vertical (v_v) bubble velocity components, horizontal bubble position (x), and bubble aspect ratio (E) for a bubble with the following volume equivalent diameter and trajectory; (a) $d_b = 1.22$, rectilinear, (b) $d_b = 1.77$, zigzag, and (c) $d_b = 1.46$ mm, helical.

of the bubble formation method, a range in the bubble diameter of which path oscillations are initiated is to be expected. As the bubble diameter increases due to reduced hydrostatic pressure over the column height, the bubble in Fig. 19(d) reaches the onset to path oscillations during the ascent. The bubble motion changes from a rectilinear to an oscillating rise path. The path oscillations continue to develop as the bubble diameter further increases, as seen in Figs. 19(e) and 19(f). The frequency and amplitude of the path oscillations are dependent on the bubble diameter.

Analyzing the bubble velocity components and the horizontal bubble displacement (x-position), different rise paths can be distinguished based on the 2 D images. For a bubble rising with a rectilinear trajectory, as in Fig. 20(a), the path analysis is straightforward. The horizontal bubble velocity component, v_h, is zero or constant, and the vertical component, v_v, is flat. With no path oscillations, the deviation from the rise centerline is zero. In some cases, a steady movement from the centerline is observed. As noted by Celata *et al.*,[20] based on a force balance, this can only be explained by the action of a lift force. Being close to spherical, the bubble in Fig. 20(a) shows no bubble shape oscillations. Hence, the bubble aspect ratio is close to constant. A slightly steady decrease is observed, which reflects the increase in size due to the reduction in hydrostatic pressure.

In the study of Celata *et al.*[21] on the effect of injection method and liquid purity, single bubbles were studied from two directions by use of four mirrors and a single high-speed camera. Comparing the bubble data from single- and double-image acquisition, Celata *et al.*[21] found the largest deviation to be in contaminated water, with a maximum difference in the determined volume equivalent bubble diameter of approximately 2.3%. In pure water, the maximum difference in calculated bubble diameter was 0.3%. Celata *et al.*[21] differentiated between a zigzag and a helical rise path based on the position and velocity components of the two projections. The observations of the velocity components and the bubble position in the present study are in accordance with the analysis of Celata *et al.*[21] In Fig. 20(b), a bubble rising in a zigzag path is shown. v_v reaches a maximum when x is at its maximum or minimum, i.e., when the bubble changes the horizontal direction. When the bubble is at the center, i.e., $x = 0$, v_v reaches a minimum value and the horizontal velocity component, v_h, is at a maximum. v_v is seen to oscillate with twice the frequency of v_h and x. It is not possible to distinguish between a zigzag and helical trajectory based on the evaluation of v_h and x from 2D images. In both cases, oscillations are observed in v_h and x. Evaluating helical rising bubbles, Celata *et al.*[21] observed v_v to be close to constant, contrary to the oscillating component for a zigzag rise path. Celata *et al.*[21] noted that for a helical rising bubble, v_h and x will oscillate in and out of phase of 90°. Analyzing the bubble in Fig. 20(c), v_v is seen to be close to constant, where v_h and x are oscillating out of phase close to 90°. It can be concluded that the bubble in Fig. 20(c) takes a helical rise path.

The bubble aspect ratio, which is strongly correlated with the bubble velocity, is seen to oscillate for both the zigzag and helical trajectory.

E. Statistical treatment

Continuous data acquisition of a single bubble over a longer spatial distance may be extremely time-demanding. Statistical accuracy is often related to a high number of experimental repetitions. To limit the number of experimental events, while ensuring a high level of accuracy, the standard deviation and the confidence interval of a measured quantity could be evaluated for an increased number of executions. Figure 21 shows the terminal velocity vs the number of experimental events for bubbles with a mean diameter $d_b = 1.34$ mm. The standard deviation is seen to be small and approaching a constant value after only five bubble rise events. As the confidence interval only depends on the standard deviation and the number of experimental events, a decrease in the confidence interval is to be expected when the standard deviation approaches a constant value. The decrease is then depending on the factor $(N-1)^{-1/2}$, which has a minor effect on the confidence interval as $(N-1)^{-1/2} = 0.23$ and $(N-1)^{-1/2} = 0.19$ for $N = 20$ and $N = 30$, respectively. Thus, the value of operating hours vs the small effect on the confidence level by performing additional experiments should be considered. Evaluating all the experimental events, the number of necessary bubble rise events is found to be 10–15.

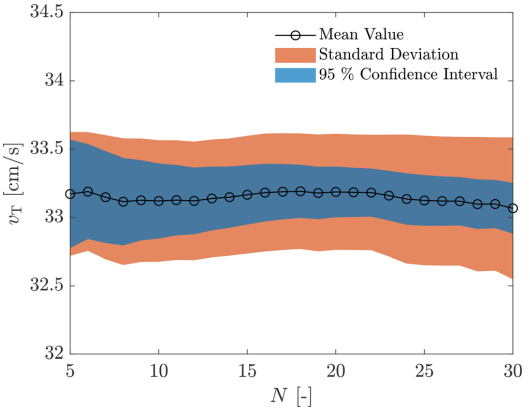

FIG. 21. Terminal velocity vs number of bubble rise events for bubbles with mean diameter $d_b = 1.34$ mm, including the standard deviation and the 95% confidence interval.

VIII. CONCLUDING REMARKS

Single air bubbles rising in a vertical column containing stagnant de-ionized water have been evaluated based on an image analysis technique. The implementation of two high-speed cameras on a linear unit drive allowed for continuous evaluation of the bubble velocity, size, and trajectory as the bubbles ascend through the column. Glass needles were employed for bubble formation of which the inner diameter never exceeded that of the volume equivalent diameter of the produced bubble. Hence, all the bubbles were injected with initially large shape deformations. For comparable bubble size, the measured terminal velocities coincide with the higher terminal velocities reported in the literature. This confirms earlier observations by Tomiyama *et al.*,[18] which stated that initially large shape deformations will result in higher

terminal velocities. The statistically significant terminal velocities obtained in this work are less scattered compared to the existing data presented in the literature.

Regarding the bubble trajectory, bubbles with a volume equivalent diameter of $d_b < 1.3$ mm, are observed to rise in a rectilinear path. In some cases, the bubbles rise in a rectilinear path with a steady movement from the centerline. The presence of a novel lift force in the initial axisymmetric configuration has been proposed in the literature. A symmetry breaking bifurcation which could explain such behavior has been mentioned in the review by Shi and Rzehak.[58] Path oscillations are seen to be initiated for bubbles in the size range $d_b \in [1.3, 1.56]$ mm. For bubbles rising with path oscillations, the instantaneous bubble velocity and bubble aspect ratio are inversely correlated. This means that when the bubble velocity is high, the bubble aspect ratio is low, and vice versa. Due to the bubble volume expansion with reduced hydrostatic pressure along the column height, the movement in the horizontal direction increases for bubbles taking an oscillating rise path. A transition from an initially rectilinear rise path to a zigzag or a helical is observed for several bubble events, reaching an onset to oscillations during rise due to the increasing bubble volume.

The existing correlations for the terminal velocity are validated against the experimental data obtained in this work. The best prediction of the experimental data is given by the correlation proposed by Tomiyama *et al.*[18] Correlated in terms of dimensionless groups, the bubble aspect ratio is well predicted when correlated as function of the Weber number. The best prediction was given by the correlation suggested by Moore.[49]

A thorough statistical analysis has been presented. The random uncertainties in the experimental data have been calculated by the propagation of error formula and the standard deviation of the mean. The two methods gave approximately the same values for the standard deviation. The statistical significance of the experimental data has been quantified. For the terminal velocity, the percentage deviation from the mean is in the range of [0.3, 4]%. The percentage deviation from the mean bubble diameter ranges from [0.1, 1]%.

The number of experimental events necessary to obtain high precision data has been evaluated using a 95% confidence interval. In this work, high statistical precision is obtained after 10–15 bubble rise events. Considering time efficiency, increasing the number of experimental repetitions to increase the accuracy of the data is not desirable. Covering a wider bubble size range of high precision bubble data, explicitly reporting on the bubble formation method, should be prioritized.

In summary, the statistically significant terminal velocity data obtained in this work show a small scatter compared to existing data in the literature. The bubbles, which were produced with initial large shape deformations, coincide with the higher terminal velocities reported in the literature. The continuous tracking of the bubbles over a tall vertical column allows for studying the effect of hydrostatic pressure on the bubble motion and size. Several bubbles initially rising in a rectilinear rise path were observed to initiate path oscillations as the bubble size increased due to reduced hydrostatic pressure. A thorough statistical analysis has been presented where the experimental uncertainties have been calculated based on different statistical methods. Important parameters involved in the image analysis have been evaluated, and the importance of the choice of threshold value used in the binarization of the raw images has been illustrated and quantified. The presented statistical analysis can benefit future work on single bubbles, as it could serve as a basis to increase the statistical accuracy of the experimental data.

APPENDIX A: STATISTICAL ANALYSIS OF TERMINAL VELOCITY CORRELATIONS

The correlations for the terminal velocity presented in Tables III and IV in Sec. II have been evaluated against the experimental data obtained in this work. In the following, the equations employed to statistically evaluate the predictability of the correlations are given.

The relative error between the experimental and the predicted terminal velocity is calculated by

$$e = \frac{v_{exp} - v_{cal}}{v_{cal}}, \tag{A1}$$

where v_{exp} and v_{cal} are the experimental and model predicted values, respectively.

The standard deviation of the error is

$$\sigma_e = \sqrt{\frac{\sum_{i=1}^{M} (e_i - \epsilon)^2}{M - 1}}, \tag{A2}$$

where M is the number of measurements (averaged values of N individual bubble rise events) and ϵ is the mean error of e:

$$\epsilon = \frac{1}{M} \sum_{i=1}^{M} e_i. \tag{A3}$$

The correlation factor $c \in [-1, 1]$ is given by

$$c = \frac{\mathrm{Cov}(e, d)}{\sigma_e \sigma_d} = \frac{\sum_{i=1}^{M} (e_i - \epsilon)(d_{b,i} - \overline{d_b})}{\sqrt{\sum_{i=1}^{M} (e_i - \epsilon)^2} \sqrt{\sum_{i=1}^{M} (d_{b,i} - \overline{d_b})^2}}, \tag{A4}$$

where σ_d and $\overline{d_b}$ are the standard deviation and the mean value of the bubble diameter, respectively.

$\mathrm{Cov}(e, d)$ is the covariance of e and d,

$$\mathrm{Cov}(e, d) = \frac{\sum_{i=1}^{M} (e_i - \epsilon)(d_{b,i} - \overline{d_b})}{M - 1}. \tag{A5}$$

Figure 22 shows the ratio between the estimated and measured terminal velocity as function of the Eötvös number.

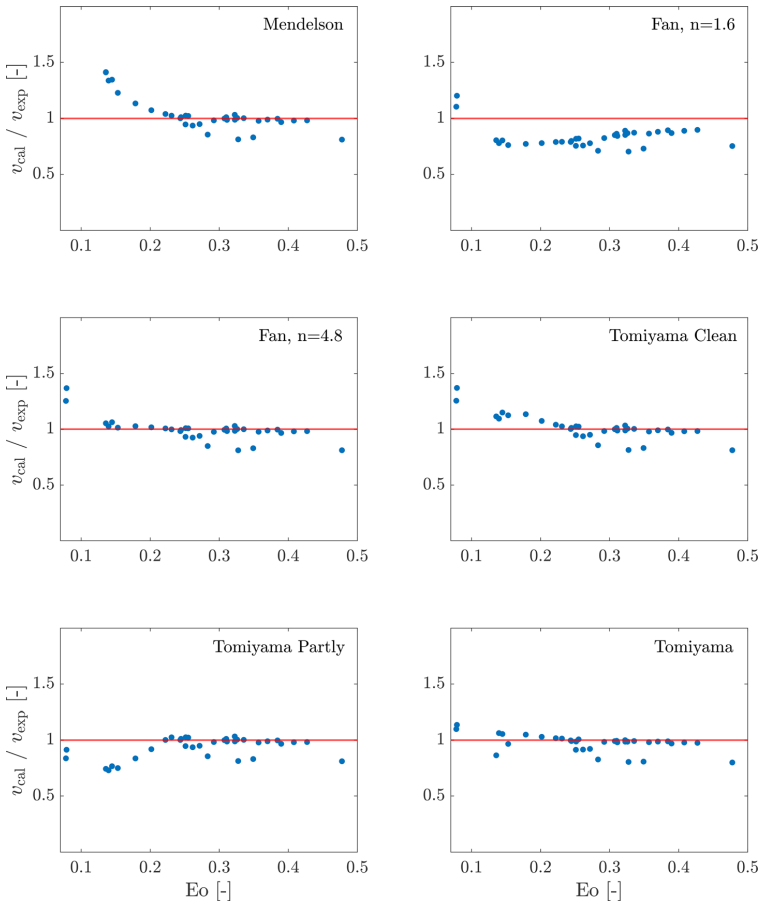

FIG. 22. a) Ratio of the predicted and measured terminal velocity as function of Eötvös number (see correlations in Tables III and IV).

APPENDIX B: STATISTICAL ANALYSIS—REPEAT OF MEASUREMENTS

The mean, $\bar{x}$, and the sample standard deviation, S, can be calculated by the general formulas[55]

$$\bar{x} = \frac{\sum_{i=1}^{N} x_i}{N}, \tag{B1}$$

$$S = \left(\frac{\sum_{i=1}^{N} (x_i - \bar{x})^2}{N-1} \right)^{1/2}, \tag{B2}$$

where x_i is the specific quantity calculated for a single bubble event, and N denotes the number of bubble rise events.

The standard deviation of the mean is given by Eq. (B3):

$$\bar{S} = \frac{S}{\sqrt{N}}. \tag{B3}$$

The $1 - \alpha$ confidence interval for the true mean, μ, can be calculated by Eq. (B4).

$$\bar{x} \pm t_{n-1,\alpha/2} \bar{S}, \tag{B4}$$

where $t_{n-1,\alpha/2}$ denotes the size of the confidence interval.

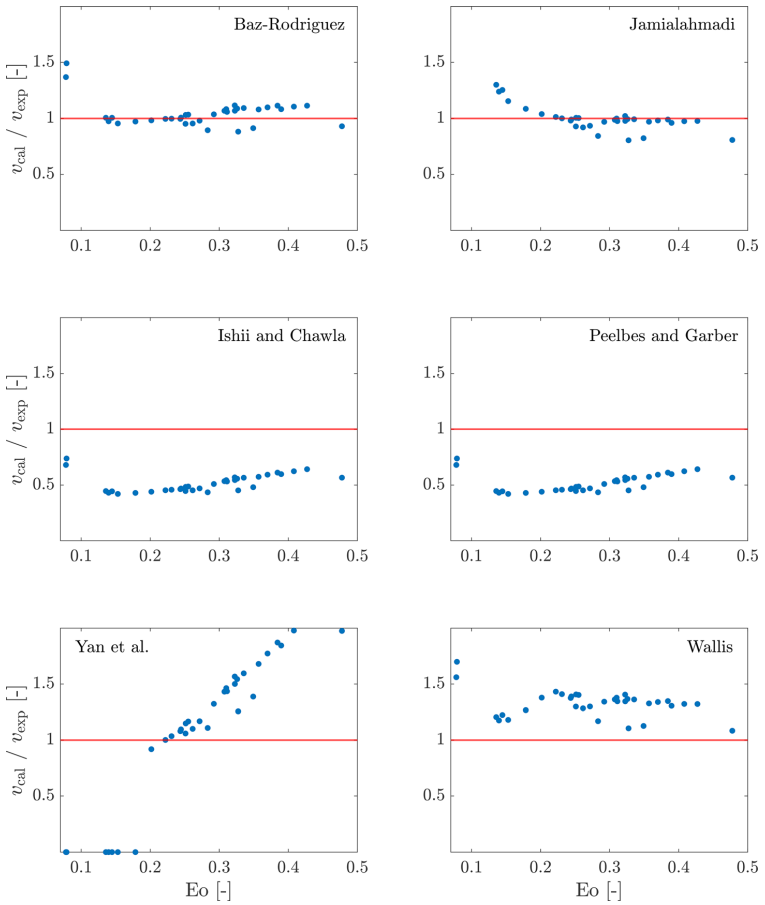

FIG. 22. b) Ratio of the predicted and measured terminal velocity as function of Eötvös number (see correlations in Tables III and IV).

APPENDIX C: STATISTICAL ANALYSIS—PROPAGATION OF ERRORS

The partial derivatives applied to calculate the uncertainty in the terminal velocity are given by

$$\frac{\partial v_b}{\partial P_{ybar,k+1}} = \frac{h_{\mathrm{cal,m}}}{h_{\mathrm{cal,px}}}\frac{1}{\Delta t}, \tag{C1}$$

$$\frac{\partial v_b}{\partial h_{\mathrm{cal,m}}} = \frac{1}{h_{\mathrm{cal,px}}}\frac{\Delta P_{\mathrm{ybar}} - \Delta P_{\mathrm{yb}}}{\Delta t}, \tag{C2}$$

$$\frac{\partial v_b}{\partial h_{\mathrm{cal,px}}} = -\frac{h_{\mathrm{cal,m}}}{h^2_{\mathrm{cal,px}}}\frac{\Delta P_{\mathrm{ybar}} - \Delta P_{\mathrm{yb}}}{\Delta t}, \tag{C3}$$

$$\frac{\partial v_b}{\partial \Delta t} = -\frac{h_{\mathrm{cal,m}}}{h_{\mathrm{cal,px}}}\frac{\Delta P_{\mathrm{ybar}} - \Delta P_{\mathrm{yb}}}{\Delta t^2}. \tag{C4}$$

In addition, $\partial v_b/\partial P_{\mathrm{ybar,k+1}} = -\partial v_b/\partial P_{\mathrm{ybar,k}} = -\partial v_b/\partial P_{\mathrm{yb,k+1}} = \partial v_b/\partial P_{\mathrm{yb,k}}$.

The partial derivatives used to calculate the uncertainty in the bubble diameter are given by

$$\frac{\partial d_b}{\partial A} = \frac{1}{3}B^2\left(\frac{h_{cal,m}}{h_{cal,px}}\right)^3\left[\left(\frac{h_{cal,m}}{h_{cal,px}}\right)^3 AB^2\right]^{-2/3}, \tag{C5}$$

$$\frac{\partial d_b}{\partial B} = \frac{2}{3}AB\left(\frac{h_{cal,m}}{h_{cal,px}}\right)^3\left[\left(\frac{h_{cal,m}}{h_{cal,px}}\right)^3 AB^2\right]^{-2/3}, \tag{C6}$$

$$\frac{\partial d_b}{\partial h_{cal,m}} = \frac{h_{cal,m}^2}{h_{cal,px}^3} AB^2 \left[\left(\frac{h_{cal,m}}{h_{cal,px}} \right)^3 AB^2 \right]^{-2/3}, \quad \text{(C7)}$$

$$\frac{\partial d_b}{\partial h_{cal,px}} = -\frac{h_{cal,m}^3}{h_{cal,px}^4} AB^2 \left[\left(\frac{h_{cal,m}}{h_{cal,px}} \right)^3 AB^2 \right]^{-2/3}. \quad \text{(C8)}$$

DATA AVAILABILITY

The data that support the findings of this study are available from the corresponding author upon reasonable request.

REFERENCES

[1]B. H. Hjertager, "Computational fluid dynamics (CFD) analysis of multiphase reactors," Trends Chem. Eng. **4**, 45–92 (1998).
[2]H. A. Jakobsen, "Modeling of vertical bubble-driven flows," Ind. Eng. Chem. Res. **36**, 4052–4074 (1997).
[3]H. A. Jakobsen, *Chemical Reactor Modeling: Multiphase Reactive Flows*, 2nd ed. (Springer, Berlin, 2014), Vol. 1.
[4]P. M. Doran, *Bioprocess Engineering Principles*, 2nd ed. (Elsevier Ltd., 2013).
[5]V. Cappello, C. Plais, C. Vial, and F. Augier, "Bubble size and liquid-side mass transfer coefficient measurements in aerated stirred tank reactors with non-Newtonian liquids," Chem. Eng. Sci. **211**, 115280 (2020).
[6]R. T. Lahey, Jr., "The analysis of phase separation and phase distribution phenomena using two-fluid models," Nucl. Eng. Des. **122**, 17–40 (1990).
[7]R. T. Lahey, Jr., "The simulation of multidimensional multiphase flows," Nucl. Eng. Des. **235**, 1043–1060 (2005).
[8]T. Haas, C. Schubert, M. Eickhoff, and H. Pfeifer, "A review of bubble dynamics in liquid metals," Metals **11**, 664–646 (2021).
[9]G. Stokes, "On the effect of the internal friction of fluids on the motion of pendulums," Trans. Cambridge Philos. Soc. **9**, 8–27 (1851).
[10]V. Levich, *Physicochemical Hydrodynamics* (Prentice-Hall, Englewood Cliffs, NJ, 1962); cited in Ref. 36.
[11]J. Hadamard, "Mouvement permanent lent d'une sphere liquide et visqueuse dans un liquide visqueux," C. R. Acad. Sci. Paris **152**, 1735–1738 (1911).
[12]W. Rybczynski, "Über die fortschreitende bewegung einer flüssigen kugel in einem zähen medium," Bull. Int. Acad. Sci. Cracovie **1**, 40–46 (1911).
[13]F. Peebles and H. Garber, "Studies on the motion of gas bubbles in liquids," Chem. Eng. Sci. **49**, 88–97 (1953).
[14]W. Haberman and R. Morton, "An experimental study of bubbles moving in liquids," Trans. Am. Soc. Civil Eng. **121**, 227–250 (1956).
[15]W. Haberman and R. Morton, "An experimental investigation of the drag and shape of air bubbles rising in various liquids," Trans. Am. Soc. Civil Eng. **802**, 227–250 (1953).
[16]H. Mendelson, "The prediction of bubble terminal velocities from wave theory," AIChE J. **13**, 250–253 (1967).
[17]A. Tomiyama, I. Kataoka, I. Zun, and T. Sakaguchi, "Drag coefficients of single bubbles under normal and micro gravity conditions," JSME Int. J. **41**, 472–479 (1998).
[18]A. Tomiyama, G. Celata, S. Hosokawa, and S. Yoshida, "Terminal velocity of single bubbles in surface tension force dominant regime," Int. J. Multiphase Flow **28**, 1497–1519 (2002).
[19]T. Okawa, T. Tanaka, I. Kataoka, and M. Mori, "Temperature effect on single bubble rise characteristics in stagnant distilled water," Int. J. Heat Mass Transfer **46**, 903–931 (2003).
[20]G. Celata, F. D'Annibale, P. D. Marco, G. Memoli, and A. Tomiyama, "Measurements of rising velocity of a small bubble in a stagnant fluid in one- and two-component systems," Exp. Therm. Fluid Sci. **31**, 609–623 (2007).
[21]G. Celata, M. Cumo, F. D'Annibale, P. D. Marco, A. Tomiyama, and C. Zovini, "Effect of gas injection mode and purity of liquid on bubble rising in two-component systems," Exp. Therm. Fluid Sci. **31**, 37–53 (2006).
[22]T. Sanada, K. Sugihara, M. Shirota, and M. Watanabe, "Motion and drag of a single bubble in a super-purified water," Fluid Dyn. Res. **40**, 534–545 (2008).
[23]S. Baz-Rodrígues, A. Aguilar-Corona, and A. Soria, "Rising velocity for single bubbles in pure liquids," Rev. Mex. Ing. Quím. **11**, 269–278 (2012).
[24]L. Liu, H. Yan, G. Zhao, and J. Zhuang, "Experimental studies on the terminal velocity of air bubbles in water and glycerol aqueous solution," Exp. Therm. Fluid Sci. **78**, 254–265 (2016).
[25]L. Liu, H. Yan, and G. Zhao, "Experimental studies on the shape and motion of air bubbles in viscous liquids," Exp. Therm. Fluid Sci. **62**, 109–121 (2015).
[26]X. Yan, Y. Jia, L. Wang, and Y. Cao, "Drag coefficient fluctuation prediction of a single bubble rising in water," Chem. Eng. J. **316**, 553–562 (2017).
[27]R. M. Davies and G. Taylor, "The mechanics of large bubbles rising through extended liquids and through liquids in tubes," Proc. R. Soc. London A **200**, 375–390 (1950).
[28]R. Clift, J. Grace, and M. Weber, *Bubbles, Drops, and Particles* (Academic Press, NY, 1978).
[29]N. Aybers and A. Tapucu, "The motion of gas bubbles rising through stagnant liquid," Wärme- und Stoffübertragung **2**, 118–128 (1969).
[30]S. Alves, S. Orvalho, and J. Vasconcelos, "Effect of bubble contamination on rise velocity and mass transfer," Chem. Eng. Sci. **60**, 1–9 (2005).
[31]P. Duineveld, "The rise velocity and shape of bubbles in pure water at high Reynolds number," J. Fluid Mech. **292**, 325–332 (1995).
[32]M. Wu and M. Gharib, "Experimental studies on the shape and path of small air bubbles rising in clean water," Phys. Fluids **14**, 49–52 (2002).
[33]D. Merker, L. Böhm, M. Oberger, P. Klüfers, and M. Kraume, "Mass transfer in reactive bubbly flows—A single bubble study," Chem. Eng. Technol. **40**, 1391–1399 (2017).
[34]M. Ishii and T. Chawla, Local drag laws in dispersed two-phase flow, Report No. ANL-79-105, 1979.
[35]J. Solsvik, "Lagrangian modeling of mass transfer from a single bubble rising in a stagnant liquid," Chem. Eng. Sci. **190**, 370–383 (2018).
[36]L. Fan and K. Tsuchiya, *Bubble Wake Dynamics in Liquids and Liquid-Solid Suspensions* (Butterworth-Heinemann, 1990).
[37]R. M. Griffith, "The effect of surfactants on the terminal velocity of drops and bubbles," Chem. Eng. Sci. **17**, 1057–1070 (1962).
[38]A. Frumkin and V. Levich, "On surfactants and interfacial motion," Zh. Fiz. Khim. **21**, 1183–1204 (1947); cited in Ref. 37.
[39]P. Saffman, "On the rise of small air bubbles in water," J. Fluid Mech. **1**, 249–275 (1956); cited in Ref. 40.
[40]K. Ellingsen and F. Risso, "On the rise of an ellipsoidal bubble in water: Oscillatory paths and liquid-induced velocity," J. Fluid Mech. **440**, 235–268 (2001).
[41]T. Bryn, "Speed of rise of air bubbles in liquids," Report No. 132, David Taylor Model Basin, 1949; cited in Ref. 28.
[42]A. Gorodetskaya, "The rate of rise of bubbles in water and aqueous solutions at great Reynolds numbers," Zh. Fiz. Khim. **23**, 71–77 (1949); cited in Ref. 28.
[43]R. M. Davies and G. I. Taylor, "The mechanics of large bubbles rising through extended liquids in tubes," Proc. R. Soc. A **200**, 375–390 (1950); cited in Ref. 28.
[44]R. L. Datta, D. H. Napier, and D. M. Newitt, "The properties and behaviour of gas bubbles formed at a circular orifice," Trans. Inst. Chem. Eng. **28**, 14–26 (1950); cited in Ref. 28.
[45]M. Jamialahmadi and H. Müller-Steinhagen, "Effect of superficial gas velocity on bubble size, terminal bubble rise velocity and gas hold-up in bubble columns," Dev. Chem. Eng. **1**, 16–31 (2008).
[46]R. Mei and J. F. Klausner, "Unsteady force on a spherical bubble at finite Reynolds number with small fluctuations in the free-stream velocity," Phys. Fluids A **4**, 63–70 (1992).
[47]L. Schiller and Z. Naumann, "A drag coefficient correlation," Z. Ver. Dtsch. Ing. **77**, 318–323 (1935).
[48]A. Tomiyama, A. Yoshida, and S. Hosokawa, "Surface tension force dominant regime of single bubbles rising through stagnant liquids," on *CD-ROM of 4th UK-Japan Seminar on Multiphase Flow, Bury St. Edmunds, UK* (2001), pp. 1–6; cited in Ref. 21.
[49]D. Moore, "The rise of a gas bubble in a viscous liquid," J. Fluid Mech. **6**, 113–130 (1959).
[50]R. Wellek, A. Agrawal, and A. Skelland, "Shape of liquid drops moving in liquid media," AIChE J. **12**, 854–862 (1966).
[51]T. Tadaki and S. Maeda, "On the shape and velocity of single air bubbles rising in various liquids," Chem. Eng. **25**, 254–264 (1961); cited in Ref. 20.

[52]I. Vakhrushev, G. Efremov *et al.*, "Interpolation formula for computing the velocities of single gas bubbles in liquids," Chem. Technol. Fuels Oils **6**, 376–379 (1970); cited in Ref. 28.
[53]C. C. M. E. Al-Mualla and D. Bull, *Video Coding for Mobile Communications* (Academic Press, 2001).
[54]N. Otsu, "A treshold selection method from gray-level histograms," IEEE Trans. Syst., Man Cybern. **9**, 62–66 (1979).
[55]J. Taylor, *An Introduction to Error Analysis* (University Science Books, 1997).
[56]W. Navidi, *Statistics for Engineers and Scientists*, 2nd ed. (McGraw-Hill International Edition, 2008).
[57]T. Taylor and A. Acrivos, "On the deformation and drag of a falling viscous drop at low Reynolds number," J. Fluid Mech. **18**, 466–476 (1964).
[58]P. Shi and R. Rzehak, "Lift forces on solid spherical particles in unbounded flows," Chem. Eng. Sci. **208**, 115145 (2019).

4.2 Paper II: Interfacial Mass Transfer from Single Bubbles

Kure, Ida Kristine; Jakobsen, Hugo Atle; Solsvik, Jannike. Experimental Study of Interfacial Mass Transfer from Single CO2 Bubbles Ascending in Stagnant Water.

This paper is submitted for publication and is therefore not included.

4.3 Paper III: Interfacial Mass Transfer in Bubble Swarms

Chemical Engineering Science 277 (2023) 118828

Contents lists available at ScienceDirect

Chemical Engineering Science

journal homepage: www.elsevier.com/locate/ces

Interface mass transfer and properties of bubbly flows in a column with Newtonian and non-Newtonian liquids

Ida K. Kure *, Hugo A. Jakobsen, Jannike Solsvik *

Department of Chemical Engineering, Norwegian University of Science and Technology (NTNU), N-7491 Trondheim, Norway

ARTICLE INFO

Keywords:
Bubble column
Mass transfer
Bubble clusters
Rheology
Shadow imaging
Image analysis
Bubble size

ABSTRACT

The mass transfer of gas–liquid systems is commonly reported through the volumetric mass transfer coefficient, k_La, which is a function of several complex phenomena. To optimize the rate of mass transfer, increased knowledge about the individual effects of the interfacial area, a, and the liquid-side mass transfer coefficient, k_L, on k_La is necessary. In this study, k_La was measured by monitoring the dissolved oxygen concentration in a bubble column. The bubble flows were recorded by a photographic method and the images were analyzed by means of artificial neural network to determine the bubble size. The effects of rheology, superficial gas velocity, and gas sparger design were analyzed. k_L decreased with an increase in the superficial gas velocity and with an increase in the viscosity. The relative change in a was much larger compared to the relative change in k_L, and hence, for the investigated operational conditions and liquid solutions, the change in k_La was mainly attributed to the change in a. Bubble clusters were formed in the non-Newtonian solutions but for the given operating conditions and liquid solutions, the bubble cluster formation did not have a prominent effect on the mass transfer.

1. Introduction

Interfacial mass transfer is an important phenomenon influencing a variety of industrial processes involving gas-liquid or gas-liquid-solid interactions, e.g., distillation, waste-water treatment, and chemical and biochemical reactors. Optimizing these processes requires accurate knowledge and data about the transfer of mass across the phase boundaries.

The rate of mass transfer is proportional to the concentration difference between the phases, where the proportionality constant is the volumetric mass transfer coefficient, k_La. Existing works on gas-liquid mass transfer have mainly focused on determining k_La in bubble swarms (Akita and Yoshida, 1973; Muroyama et al., 2013; Scargiali et al., 2010; Vandu et al., 2004; Zednikova et al., 2018). Complex phenomena are involved in the liquid-side mass transfer coefficient, k_L, and the interfacial area, a. The individual effect of k_L and a on the mass transfer cannot easily be predicted when lumped into the combined coefficient of k_La. Relatively few studies exist where k_L and a have been individually determined in bubble columns (Akita and Yoshida, 1974; Bouaifi et al., 2001; Eckenfelder and Barnhart, 1961; Jeng et al., 1986; Kawase and Moo-Young, 1990; Koide et al., 1985; Miller, 1983; Sastaravet et al., 2020; Vasconcelos et al., 2003). Relevant studies on k_L and a in bubble columns where the latter is determined using a photographic method (Bouaifi et al., 2001; Koide et al., 1985; Sastaravet et al., 2020; Vasconcelos et al., 2003) are summarized in the following.

Koide et al. (1985) and Vasconcelos et al. (2003) studied the influence of anti-foaming agents on k_La, k_L, and a. Koide et al. (1985) performed experiments in water and aqueous solutions of alcohols, while the work of Vasconcelos et al. (2003) was restricted to water. Both Koide et al. (1985) and Vasconcelos et al. (2003) found that k_La and k_L decreased with presence of anti-foaming agents. Koide et al. (1985) observed that k_L decreased and the gas hold-up, α_G, increased with presence of surfactants (n-alcohols). Furthermore, α_G decreased with presence of anti-foaming agents. Bubble size distributions were not provided in the studies of Vasconcelos et al. (2003) and Koide et al. (1985). Sastaravet et al. (2020) investigated the effect of solid particles on bubble hydrodynamics and mass transfer enhancement in tap water. k_La increased with increasing superficial gas velocity, u_s, for all conditions, where the presence of solid particles enhanced k_La. k_L decreased with an increase in u_s ($u_s \in [0.26, 1.53]$ cm/s) both with and without solid particles. The bubble sizes with solid particles were reported smaller than without particles (~ 22–27% on average). However,

* Corresponding authors.
E-mail addresses: ida.k.kure@ntnu.no (I.K. Kure), jannike.solsvik@ntnu.no (J. Solsvik).

https://doi.org/10.1016/j.ces.2023.118828
Received 19 September 2022; Received in revised form 17 November 2022; Accepted 29 April 2023
Available online 8 May 2023

in none of the studies the bubble size distributions from which the average bubble diameters were calculated were provided. Considering the splitting of $k_L a$ into k_L and a, it is desirable to have a narrow bubble size distribution from which the mean bubble diameter is calculated. A narrow bubble size distribution increases the accuracy of the influence of a on $k_L a$. Furthermore, in mass transfer studies where k_L is calculated from $k_L a$ and a, reducing the uncertainty in a reduces the uncertainty in k_L. Therefore, when studying the individual effects of k_L and a on $k_L a$, the information of bubble size distributions is necessary. Bouaifi et al. (2001) measured k_L in tap water where air was dispersed through spargers of various designs (membrane, porous plate, and perforated plate). $k_L a$ increased with increasing u_s at all the operating conditions. k_L was independent of the specific power consumption which was related to the gas pressure drop – a function of u_s, the sparger pressure drop, the liquid density, gravity, and tank liquid height. Bubble size distributions for the different spargers were provided, where the size distributions ranged from 1.5–6.5 mm and 1.5–6.5 mm for the porous plate and membrane, respectively, and the size distribution ranged from 1.5–11.5 for the perforated plate. For the membrane, approximately 80% of the bubble sizes were within the 3.5–4.5 mm size range.

Despite the analysis of the individual parameters of k_L and a, the experimental data obtained by Koide et al. (1985), Vasconcelos et al. (2003), Sastaravet et al. (2020), and Bouaifi et al. (2001) are limited to Newtonian solutions. In bioprocesses, e.g., in fermentation, the viscosity of the fermentation fluids is affected by the presence of cells, substrates, and products (Doran, 2013). A variety of fermentation processes involve materials that exhibit non-Newtonian behavior (Badino et al., 1976; Blanch and Bhavaraju, 1976), e.g., culture broths with suspended cells and extracellular polysaccharides (Doran, 2013). The non-Newtonian fluids commonly found in bioprocesses are pseudoplastic, Bingham plastic, and Casson plastic (Doran, 2013). Motivated by industrial application, the study of the individual contributions of k_L and a to $k_L a$ should be extended from Newtonian solutions to viscous Newtonian and non-Newtonian solutions.

Augier and Raimundo (2021) studied the effect of rheology on mass transfer and bubble size in bubbly flows in the heterogeneous regime ($u_s \in [3, 30]$ cm/s). k_L, a, and local gas volume fraction were measured in non-Newtonian solutions (carboxymethyl cellulose (CMC) and xanthan gum (XG)). The gas was dispersed by a perforated plate which was chosen similar to that of Gemello et al. (2018), which enabled generation of bubbles in water that were close to their initial size. An in-situ probe (referred to as cross-correlation method) was applied to measure the bubble size and the local gas volume fraction. The differences in the measured bubble size between the solutions were governed by the rheology and not u_s. Except in water, where u_s had a strong effect on k_L, the rheology of the solutions explained the differences in the measured k_L. $k_L a$ and the local gas volume fraction were governed by both the rheology and u_s. The summarized results by Augier and Raimundo (2021) are based on radially averaged values of the bubble size and the local gas volume fraction. For $u_s > 3$ cm/s, the bubble diameter varied with the radial position. Bubble size distributions were not provided, and with a variation in the bubble diameter and the local gas volume with the radial position it is challenging to evaluate the accuracy in k_L when k_L is calculated from a and $k_L a$.

Martínez-Mercado et al. (2007) and Vélez-Cordero and Zenit (2011) developed experimental set-ups which allowed for production of close to mono-sized (narrow bubble size distribution) bubbles. The experimental set-ups were used for studies on bubbly flows in Newtonian (Martínez-Mercado et al. (2007), Vélez-Cordero and Zenit (2011)) and non-Newtonian (Vélez-Cordero and Zenit (2011), Vélez-Cordero et al. (2012)) solutions. With the ability of creating mono-sized bubbles, the design of the experimental set-ups has thus a potential to be further used for accurate mass transfer studies where $k_L a$ is split into k_L and a. Martínez-Mercado et al. (2007) measured the gas and liquid velocities in water and water/glycerol solutions, where the gas was introduced by an array of capillaries which created a mono-sized bubbly flow. The measurements were conducted for bubble Reynolds numbers from 10 to 500. The mean bubble velocity decreased with increasing α_G. For very dilute flows, the measured mean bubble velocity deviated largely from the velocity of a single isolated bubble. Vélez-Cordero and Zenit (2011) studied bubbly flows in the homogeneous regime ($u_s \in [0.09, 0.6]$ cm/s), using XG and glycerol/water solutions. The bubble column was similar to that used by Martínez-Mercado et al. (2007), where sets of capillary banks were designed to create mono-sized bubbles. Bubble clusters (aggregates of bubbles) were only formed in the shear-thinning liquids, where the clusters grew with increased gas volume fraction. Compared to single bubbles, the mean bubble velocity of the clusters increased. During bubble ascent, the bubble clusters had a dynamic structure, rising in the center and descending on the exterior part of the cluster. In some of the shear-thinning solutions, only the smallest bubbles formed clusters. Vélez-Cordero et al. (2012) studied the properties of bubbly flows in elastic fluids with approximately constant viscosity. The bubble column was similar to that by Martínez-Mercado et al. (2007), and the capillary banks were similar to those used by Vélez-Cordero and Zenit (2011). The bubble dispersion changed as function of the bubble size. For smaller bubble diameters, large vertical bubble clusters were formed. The larger bubbles, on the other hand, ascended in a dispersed manner. Although mass transfer analyzes were not performed, Vélez-Cordero et al. (2012) suggested that the formation of small bubbles may not be optimal to achieve high mass transfer rates in visco-elastic flows due to the formation of bubble clusters. Hence, larger bubble sizes could be more convenient for the mass transfer. A next step in the investigations of bubbly flows by Martínez-Mercado et al. (2007); Vélez-Cordero and Zenit (2011), and Vélez-Cordero et al. (2012) is to include mass transfer studies.

The objective of this work was to study the effect of liquid rheology and operating conditions on the mass transfer in a bubble column which enabled the generation of mono-sized bubbles. Due to the complex phenomena involved in $k_L a$, it was of desire to evaluate the individual effects of k_L and a. When splitting $k_L a$ into k_L and a, d_b should be based on a narrow bubble size distribution. A column and sparger design similar to those described by Vélez-Cordero and Zenit (2011) were thus applied to enable production of bubbles with a narrow bubble size distribution. For each sparger used in the present work, bubble size distributions were provided at different u_s and liquid solutions. The oxygen concentration and the bubble sizes were obtained using in situ dissolved oxygen (DO) probes and a high-speed camera. An artificial neural network (ANN) was used in the image processing procedure to determine the bubble sizes with a small statistical uncertainty. The individual effects of k_L and a on $k_L a$ were studied for $u_s \in [0.07, 0.47]$ cm/s. Bubble clusters can be seen in fluids represented in the bioprocess industry. The existing literature on bubble clusters mainly focuses on bubble cluster formation and bubble cluster velocity (Vélez-Cordero and Zenit, 2011). With the increasing interest for bioprocess industry, it is crucial to establish understanding of the mass transfer from bubble clusters for optimal process performance. In this work, the effects of bubble clusters on $k_L a$ and flow dynamics were investigated.

2. Materials and methods

2.1. Experimental setup

The bubble experiments were carried out in a vertical rectangular column with dimensions $180 \times 10 \times 5$ cm^3, as illustrated in Fig. 2.1. The column was made of stainless steel except from the two widest walls which were made of soda-lime glass. The column was mounted to a gas chamber with dimensions $11 \times 10 \times 5$ cm^3 from where the gas phase was dispersed by a capillary bank. Different mean bubble sizes were generated using three capillary banks which were made of stainless steel, noted here as N1, N2, and N3, and which differed in the number of capillaries and their inner diameter. The capillary banks, illustrated in Fig. 2.2 (a), were designed similar to those in the work by

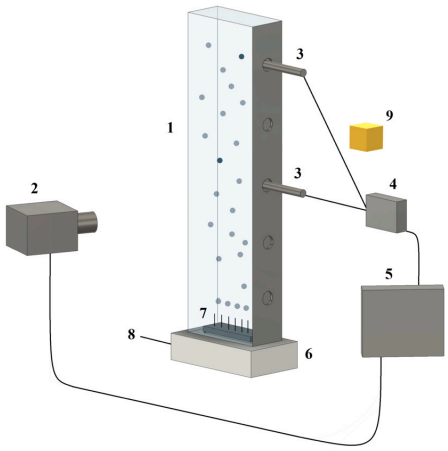

Fig. 2.1. Experimental facility composed of 1) liquid column, 2) camera, 3) oxygen probes, 4) transmitter, 5) computer, 6) gas chamber, 7) capillary bank, 8) gas supply, 9) illumination.

Table 2.1
Design parameters of the capillary banks. $D_{cap,u}$ and $D_{cap,l}$ are the inner diameter of the upper and lower capillaries, respectively. N and L are the number and length of the capillaries, respectively. ΔL_{cap} is the distance between the capillaries.

Capillary bank	$D_{cap,u}$ [mm]	$D_{cap,l}$ [mm]	N [-]	L [cm]	ΔL_{cap} [cm]
N1	1.6	0.48	16	8.9	1.2
N2	0.6	0.25	27	8.5	0.9
N3	0.13	0.13	43	7.0	0.6

Vélez-Cordero and Zenit (2011), where the inner diameters of the capillaries were selected by balancing the buoyancy and surface tension forces. The capillary bank configurations used in this work are shown in Fig. 2.2 (b-d) and the design parameters are given in Table 2.1. The geometrical ratios in Fig. 2.2 (b-d) correspond to the physical ratios. The capillaries were glued to the metal plates. For capillary banks N1 and N2, the metal plates had two sets of capillaries where the capillaries on the topside of the plates had a different inner diameter than the ones on the underside. For capillary bank N3, the inner diameter of the capillaries on the topside and underside was the same. The design of the capillary banks ensured sufficient hydrostatic resistance to produce individual bubbles and avoid the generation of gas jets. The gas volume flow rate, Q, was controlled by a flow-meter (ALICAT SCIENTIFIC MC-2slpm), and u_s was in the range of 0.07 cm/s to 0.47 cm/s ($u_s = Q/A$, where A is the cross sectional area of the bubble column). Table 2.2 provides the investigated flow conditions. All analyzes of the bubble column were conducted under ambient temperature and pressure (22 $\pm$1 °C and 1 atm). The DO concentration was monitored by three probes (METTLER TOLEDO InPro6860i). The DO probes were inserted into the column through the side walls in such a way that they did not affect the fluid dynamics. The DO probes were inserted at two heights and on both side walls of the column to observe any effects of the measurement position. The column was disassembled and cleaned with deionized water after each experimental day. The capillary banks were cleaned after each experimental day by inserting them into a container with a water–ethanol solution. The container was then put into an ultrasonic bath and left for 20 minutes.

Data on the bubble size distribution and the mean bubble size were acquired using a high-speed camera (Photron FASTCAM MINI AX100) and a lens (Tamron SP 90mm F2.8 Di VC USD Macro), known as shadow imaging technique. The frame rate was adjusted to the desired objective; 50 frames per second (fps) when recording images for measuring the bubble size, and 500 fps when recording images for analyzing the bubble flow dynamics. The camera-to-column position was varied to obtain both high-resolution and low-resolution images, where the former were used to determine the bubble size and the latter for study of the flow fields. The camera-to-column distances were 47 cm and 147 cm for the high-resolution and the low-resolution images, respectively. Diffusion paper was attached to the column wall opposing the camera and a light-emitting diode (LED) was located 90° to the column and reflected by a panel. The resolution of the camera was 1024×1024 px^2 (pixels^2). The geometrical calibration between px and length scale was obtained as the average from the acquired images of a ruler placed in front and back of the column.

2.2. Liquid solutions

Table 2.3 summarizes the physical properties of the solutions. Deionized water and glycerol/water were used as Newtonian solutions. 0.04 M $MgSO_4$ (Magnesium sulfate heptahydrate, ACS reagent, $\geq$ 98%, Sigma Aldrich) was introduced in all the solutions to prevent coalescence (Lessard and Zieminski, 1971). To obtain a shear-thinning behavior with negligible elastic properties, solutions consisting of a mixture of XG, glycerol, and water were selected. The percentages of XG and glycerol solutions in Table 2.3 are given in weight terms and volume terms, respectively. The non-Newtonian solutions were prepared by dissolving XG (from Xanthomonas campestris, Sigma Aldrich) in water (preheated to 50 °C) under mechanical stirring for 60 minutes. While stirring the solution, the container was sealed with aluminum foil to keep the temperature close to 50 °C. Then the $MgSO_4$ was introduced and kept under stirring for 15 minutes. Finally, glycerol ($\geq$ 97%, TECHNICAL, VWR Chemicals) was added. The solutions were stirred for 24 h, after which they were held at rest for additional 24 h. The resting time was necessary to let the entrapped bubbles ascend and leave the liquid.

Samples were collected each experimental day for measuring the surface tension, σ, density, ρ, and the apparent viscosity, μ_a, of the solutions. The surface tension was measured by a tensiometer (Sigma 701, Biolin Scientific, Sweden), using the Du Noüy ring method. The samples were stirred, and entrapped bubbles removed before the surface tension was measured. To measure the liquid density a density meter (DMA^{TM} 5000 M, Anton Paar GmbH, Austria) was employed. The apparent viscosity was measured by a rheometer (Physica MCR 301, Anton Paar GmbH, Austria) using a cup geometry. Before viscosity measurements, the samples were left at rest for a sufficient time to remove small bubbles trapped in the solutions. A shear rate in the range of $0.1 - 1000$ s^{-1} was applied to measure the shear-thinning behavior of the XG-solutions. The viscosity as function of shear rate is plotted in Fig. 2.3. The apparent viscosity of the non-Newtonian solutions can be characterized well with the Power-law model (Ostwald-de Waele) (Irgens, 2014):

$$\mu_a = K\dot{\gamma}^{n-1} \tag{1}$$

where K is the consistency index [Pa·s^n], n the power law index [-], and $\dot{\gamma}$ the shear rate [s^{-1}].

2.3. Volumetric mass transfer coefficient

k_La was estimated using the dynamic gas-in method (Garcia-Ochoa and Gomez, 2009). The liquid phase was flushed with nitrogen gas until the DO concentration was less than 10%. Clean compressed air was introduced, and the DO concentration was monitored until the air concentration in the liquid phase, C_L, was >70%. According to Doran (2013), the dynamics of the oxygen probe can be neglected if the probe response time, τ_p, is less than the characteristic time of mass transfer, i.e., $\tau_f = 1/(k_La)$. The probe time constant was measured for all the probes and found negligible in all the solutions. Assuming perfect mix-

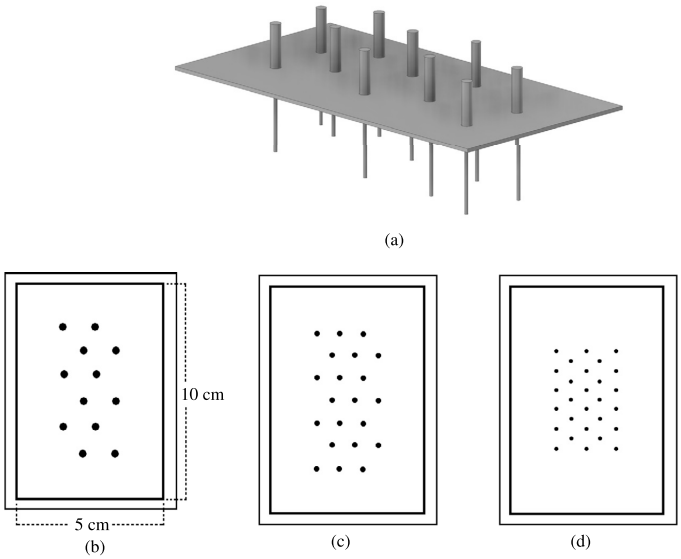

Fig. 2.2. (a) scheme of a capillary bank, and (b-d) capillary bank configurations: (b) N1, (c) N2, (d) N3.

Table 2.2
Investigated flow conditions (u_s and Q) in the liquid solutions.

	Capillary bank	Water	Glycerol/water	0.02% XG	0.1% XG
u_s	N1	[0.29, 0.4, 0.47]	[0.4, 0.47]	[0.4, 0.47]	[0.4, 0.47]
	N2	[0.07, 0.12, 0.2, 0.29, 0.4, 0.47]	[0.07, 0.29, 0.47]	[0.07, 0.47]	[0.07, 0.29, 0.47]
	N3	[0.07, 0.12, 0.2, 0.29, 0.4, 0.47]	[0.07, 0.29, 0.47]	[0.07, 0.47]	[0.07, 0.29, 0.47]
Q	N1	[0.86, 1.19, 1.42]	[1.19, 1.42]	[1.19, 1.42]	[1.19, 1.42]
	N2	[0.22, 0.35, 0.61, 0.86, 1.19, 1.42]	[0.22, 0.86, 1.42]	[0.22, 1.42]	[0.22, 0.86, 1.42]
	N3	[0.22, 0.35, 0.61, 0.86, 1.19, 1.42]	[0.22, 0.86, 1.42]	[0.22, 1.42]	[0.22, 0.86, 1.42]

Table 2.3
Physical properties of the solutions.

Solution	ρ [kg/m^3]	μ_a [mPa·s^n]	σ [mN/m]	n [-]	K [mPa·s^n]
Water	1000	1.0	72	1	-
83% glycerol/water	1226	120	63.8	1	-
0.02% XG, 75% glycerol/water	1209	...	63.2	0.856	134.2
0.1% XG, 60% glycerol/water	1173	...	64.2	0.532	411.8

ing in both phases, the rate of change of the oxygen concentration can be expressed by equation (2) as (Garcia-Ochoa and Gomez, 2009):

$$\frac{dC_L}{dt} = k_L a(C^* - C_L) \tag{2}$$

where C^* denotes the DO saturation concentration [%].

Integrating equation (2), the following linear relation is obtained:

$$\ln\left(\frac{C^* - C}{C^* - C_{t=0}}\right) = -k_L a \cdot t \tag{3}$$

where t denotes the time, and $C_{t=0}$ the DO concentration at time $t = 0$.

When the gas is switched from nitrogen to air, the incoming air mixes with the existing nitrogen until all the excess gas from the deoxygenation step is flushed out. During this process, the change of gas composition influences the measured oxygen concentration. $k_L a$ is estimated as the slope of a linear line by plotting $\ln\left(\frac{C^* - C}{C^* - C_{t=0}}\right)$ against t (in MATLAB R2021b, MathWorks, USA). $k_L a$ was estimated in the range of 30–70% oxygen concentration. The measurements were repeated three times for each operational condition. $k_L a$ was calculated as the average from the three probes applied in the set-up and for three repetitions of measurements such that an averaged $k_L a$ value for a specific bubble column condition is based on 9 independent measurements.

2.4. Bubble size and flow measurements

The number of bubbles necessary to achieve statistical significance of the bubble size data was ensured by recording a total number of 1000 images per experiment. The recorded images were processed by an image analysis algorithm using ANN, developed by SOPAT Gmbh (Berlin, Germany). The ANN algorithm was trained to recognize and distinguish between different scenarios; single bubbles, doublets, triplets, or clusters of bubbles. Further training of the algorithm is necessary for precise detection of the bubble clusters, hence, in this work the ANN algorithm has been used to determine a for bubbles that do not form part of a cluster. Fig. 2.4 illustrates the image acquisition and bubble detec-

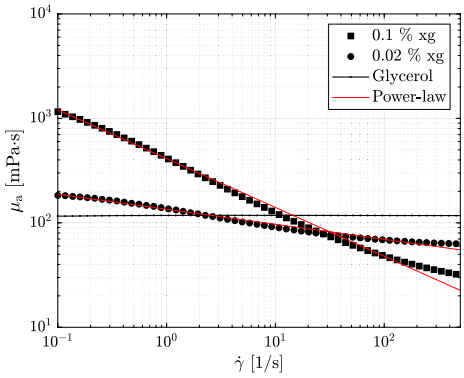

Fig. 2.3. Viscosity as function of shear rate, including the Power-law model (Irgens, 2014). The plot is presented on a logarithmic scale.

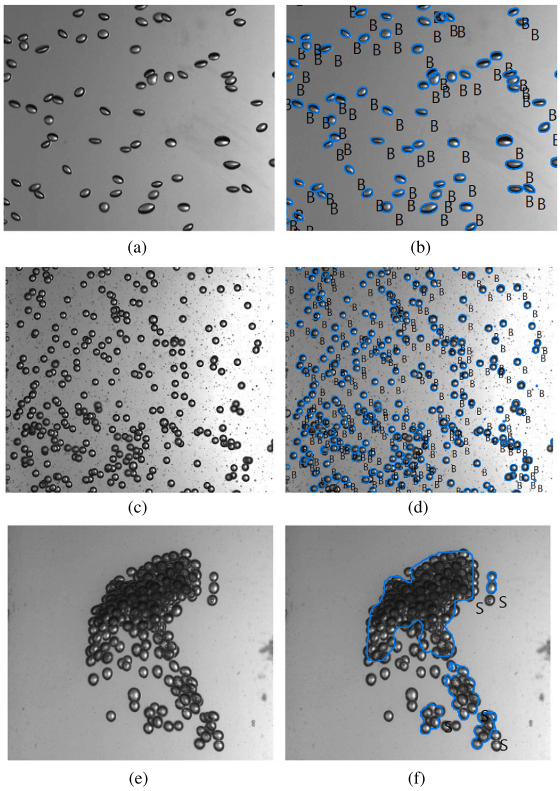

Fig. 2.4. Image acquisition and bubble detection of system (a-b) water, (c-d) glycerol/water, and (e-f) 0.1% XG. The first column shows the raw images and the second column shows the processed images. The images have been cropped and are not shown in their original sizes.

tion performed by the image analysis software. Blue borders mark the boundaries of the detected bubbles by the ANN algorithm.

In the two-dimensional plane, the Feret diameter, d_F, is based on the distance between two parallel lines that restrict a particle, in this case a bubble (Emmerich et al., 2019). Fig. 2.5 illustrates the principle of the Feret diameter using a caliper where its two parallel pins restrict

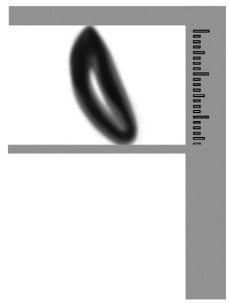

Fig. 2.5. A caliper with two parallel pins which restrict the bubble of an image.

the bubble. In such, for non-spherical bubbles, d_F depends upon the orientation of the bubble in the caliper. In the algorithm applied, 16 values of d_F are measured upon rotating the bubble in equidistantly steps between 0° and 180°. From these 16 d_F-values, the average Feret diameter, $d_{F,mean}$ is computed.

The equivalent bubble diameter, d, is estimated from $d_{F,mean}$ as:

$$d = \left(\frac{4A}{\pi}\right)^{1/2} \tag{4}$$

$$A = \frac{\pi}{4} d_{F,mean}^2 \tag{5}$$

where A denotes the side-viewed projected bubble area.

The bubbles in a bubble column are unavoidably produced with various sizes. The distribution in bubble size can be small or large depending on the sparger design, operational conditions, and fluid properties. The various bubble sizes constitute a size distribution which can be characterized in terms of a histogram. A mean bubble size is commonly computed from the bubble size distribution and applied in analyzes and calculations of mass transfer. The Sauter mean diameter, d_b, is commonly used to characterize the mean bubble size:

$$d_b = \frac{\sum_{i=1}^{N_p} d_i^3}{\sum_{i=1}^{N_p} d_i^2} \tag{6}$$

where N_p denotes the total number of bubbles, and i the bubble index number.

A sensitivity analysis was performed to evaluate the evolution of d_b versus the number of measured bubbles, n. Fig. 2.6 shows sensitivity plots for the cases of water and glycerol/water. For every new measured bubble size (blue dots), d_b was recalculated (red dots). As seen from Fig. 2.6, d_b converged rapidly for all the operational conditions ($\sim$ 5000 bubbles for water and $\sim$ 20000 bubbles for glycerol/water were sufficient to achieve the steady bubble diameter).

2.5. Liquid mass transfer coefficient

The gas hold-up was calculated by measuring the change in liquid height due to the presence of gas. With the gas present, sufficient time was given to reach a steady state before measuring the liquid height. α_G can be related as $\alpha_G = \Delta H/H$, where H denotes the liquid level without gas ($H = 136 \pm 2$ cm in the present experiments), and ΔH the height difference resulting from the dispersed gas (Vandu et al., 2004). When d_b and α_G are known, the interfacial area can be calculated by equation (7) (Jakobsen, 2014):

$$a = \frac{6\alpha_G}{d_b} \tag{7}$$

The liquid-side mass transfer coefficient can thus be calculated by equation (8):

$$k_L = k_L a \left(\frac{6\alpha_G}{d_b}\right)^{-1} \tag{8}$$

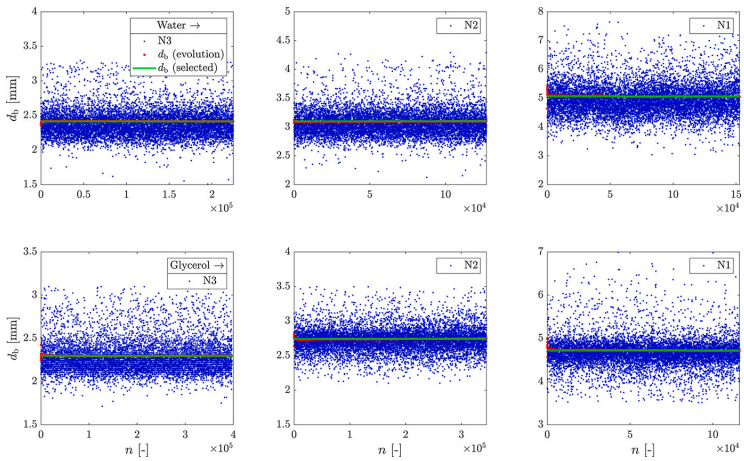

Fig. 2.6. Evolution of the calculated Sauter mean diameter (red marks) as function of the number of measured bubbles in water and glycerol/water, where $u_s = 0.07$ cm/s for capillary banks N2 and N3, and $u_s = 0.40$ cm/s for capillary bank N1. The green line marks the selected diameter.

3. Results and discussion

3.1. Bubbly flow dynamics

Figs. 3.1, 3.2, and 3.3, illustrate the bubble formation by the capillary banks in water, glycerol/water, and 0.1% XG, respectively. Fig. 3.1 shows formation of mono-sized bubbles in water by the capillary banks. Capillary banks N3 and N2 in glycerol/water (Figs. 3.2 (a-b)) and capillary bank N3 in 0.1% XG (Fig. 3.3 (a)) produce mono-sized bubbles which densely ascend in the same path close to the capillaries. In glycerol, the bubbles produced by capillary banks N3 and N2 are homogeneously dispersed across the column cross-section after approximately 20 – 30 cm. Figs. 3.4 (b) and 3.5 (b) illustrate the homogeneous dispersion in glycerol acquired at a column height of approximately 110 cm. Due to the shear-thinning behavior in 0.1% XG, a bubble produced by capillary bank N3 continues to ascend in the same path as the previous bubble along the column height. That is, a successive bubble will experience a lower viscosity and hence take this path. Fig. 3.6 illustrates the flow pattern of bubbles in the non-Newtonian solutions which ascend in the same path independent of the vertical position in the bubble column. The bubbles produced by capillary bank N1 in glycerol/water (Fig. 3.2 (c)) and capillary banks N2 and N1 in 0.1% XG (Figs. 3.3 (b-c) do not ascend in dense path close to the capillaries. In 0.1% XG, however, the bubbles produced by capillary banks N2 and N1 are affected by the shear-thinning behavior which causes the bubbles to ascend in the same path and form bubbles clusters higher up in the bubble column, as illustrated in Figs. A.1-A.3 in Appendix A.

The bubble flows are significantly different in the Newtonian and non-Newtonian solutions, as illustrated in Figs. 3.4 and 3.5, where capillary bank N3 was selected for the illustration. The bubbles in water and glycerol/water are homogeneously dispersed for all three capillary banks and at all investigated u_s in the interval of 0.07 – 0.47 cm/s. In 0.02% XG, however, the bubble flow pattern depends on the capillary bank and u_s. In 0.02% XG, capillary banks N1 and N2 produce homogeneously dispersed bubbles at all u_s. On the other hand, capillary bank N3 in 0.02% XG produces homogeneously dispersed bubbles at the highest gas velocity $u_s = 0.47$ cm/s (Fig. 3.5 (c)), while bubble clusters are formed at the lowest gas velocity $u_s = 0.07$ cm/s (Fig. 3.4 (c)). In 0.1% XG, bubble clusters are formed for all three capillary banks and at all investigated u_s; Figs. 3.4 (d) and 3.5 (d) show the bubble clusters formed by N3 at $u_s = 0.07$ cm/s and $u_s = 0.47$ cm/s, respectively. Increasing u_s in 0.1% XG leads to increased formation of single bubbles in addition to the bubble clusters, as shown by Figs. 3.4 (d) and 3.5 (d). Furthermore, an increase in u_s increases the liquid circulation where single bubbles are down-flowing on the opposite site of the uprising bubble clusters. Downflowing bubbles on opposite side of bubble clusters are illustrated for capillary bank N3 in 0.02% XG at $u_s = 0.07$ cm/s in Fig. 3.6 (b). The bubble size of the single bubbles appears to be approximately

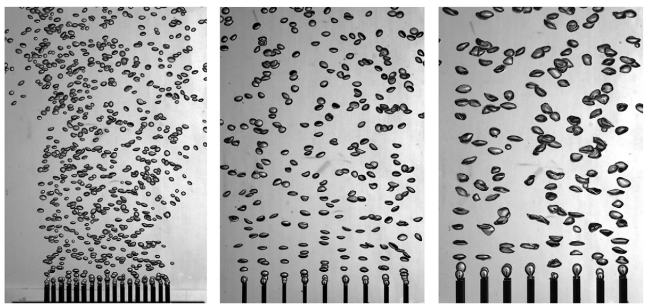

Fig. 3.1. Bubble formation in water by capillary bank (a) N3, (b) N2, and (c) N1, where $u_s = 0.2$ cm/s for capillary banks N2 and N3, and $u_s = 0.40$ cm/s for capillary bank N1. The images represent a physical size of (a) 11×8 cm^2, and (b-c) 12×8 cm^2.

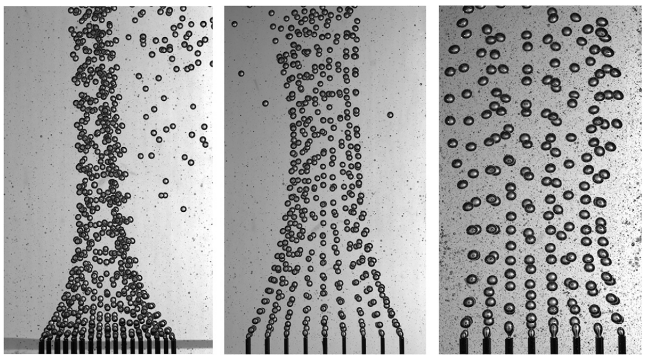

(a) (b) (c)

Fig. 3.2. Bubble formation in glycerol/water by capillary bank (a) N3, (b) N2, and (c) N1, where $u_s = 0.13$ cm/s for capillary banks N2 and N3, and $u_s = 0.40$ cm/s for capillary bank N1. The images represent a physical size of (a) 12×7 cm^2, and (b-c) 15×9 cm^2.

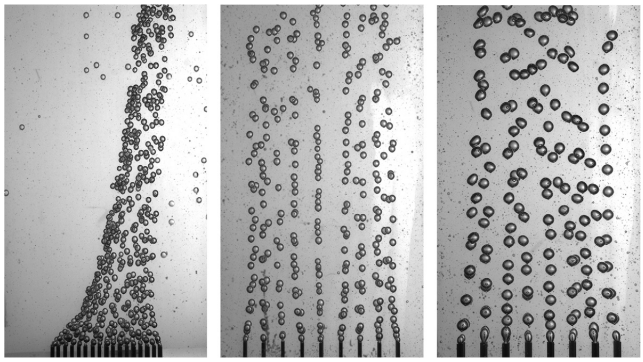

(a) (b) (c)

Fig. 3.3. Bubble formation in 0.1% XG by capillary bank (a) N3, (b) N2, and (c) N1, where $u_s = 0.13$ cm/s for capillary banks N2 and N3, and $u_s = 0.40$ cm/s for capillary bank N1. The images represent a physical size of 15×9 cm^2.

the same as those forming clusters. Section 3.2 presents plots of the bubble diameter of the single bubbles formed in the non-Newtonian solutions.

In 0.1% XG and 0.02% XG, a bubble takes the same path as the previous bubble released from the same capillary due to the shear-thinning effect. Fig. 3.6 illustrates the shear-thinning effect on the bubble flow field for capillary banks N2 and N3 in 0.1% XG and 0.02% XG at $u_s = 0.07$ cm/s. For capillary bank N3 at $u_s = 0.07$ cm/s in 0.1% XG (Fig. 3.6 (a)), the bubbles leaving the capillary bank are rising in the same path as the former bubbles before forming bubble clusters higher up in the column. While rising, the bubble clusters have a dynamic structure with the centered bubbles rising and the exterior bubbles descending continuously. The bubbles are changing position within the cluster as the cluster ascends, break up, and form new clusters, and hence the gas–liquid-interface is continuously renewed. Similar dynamic behavior was observed by Vélez-Cordero and Zenit (2011). The dynamic behavior of the clusters is attempted illustrated through the various cluster structures present in Fig. 3.6 (a). Comparing Figs. 3.6 (a) and (b), the bubble clusters produced by capillary bank N3 in 0.1% XG have denser structures compared to 0.02% XG, i.e., the number of bubbles forming a bubble cluster is higher and the number of single bubbles is lower in 0.1% XG. No bubble clusters are formed by capillary bank N2 at $u_s = 0.07$ cm/s in 0.02% XG (Fig. 3.6 (c)), where the bubbles ascend in a less dense path due to the design of the capillary bank. Appendix A provides additional images of the bubble clusters formed in 0.1% XG by the three capillary banks.

3.2. Sauter mean diameter

Fig. 3.7 (a) shows the influence of u_s on d_b in water. d_b produced by capillary bank N3 in water is approximately constant for $u_s \in [0.07, 0.29]$ cm/s, whereas increases with a further increase in u_s. The opposite trend is observed for capillary bank N2, where d_b increases for $u_s \in [0.07, 0.29]$ cm/s, after which d_b is constant. d_b in glycerol/water increases linearly with u_s for all the capillary banks in Fig. 3.7 (b). Capillary bank N1 produces bubbles with similar d_b in water and glycerol/water at $u_s \in [0.4, 0.47]$ cm/s. The standard deviations of d_b presented in Fig. 3.7 are minor and not visible with the scale of the figure. The uncertainties in the measurement methods, potentially resulting in systematic errors, are difficult to measure. Hence, the standard deviations of d_b, α_G, and $k_L a$ are based on the repeat of measurements.

Fig. 3.8 presents d_b for the individual bubbles (not considering the cluster size) in the non-Newtonian solutions. As in the Newtonian cases, d_b in 0.02% XG and 0.1% XG increases with an increase in u_s. d_b of the individual bubbles produced in 0.1% XG is slightly larger than that produced in glycerol/water. The bubbles produced in 0.02% XG, however, are more similar in size to those obtained in glycerol/water. Based on the trend in the data for d_b in water, glycerol/water, 0.1% XG, and 0.02% XG, it is evident that d_b is influenced by the viscosity of the solutions.

Figs. 3.9 and 3.10 show bubble size distributions at different u_s for water and glycerol/water, respectively. The bubble size distributions

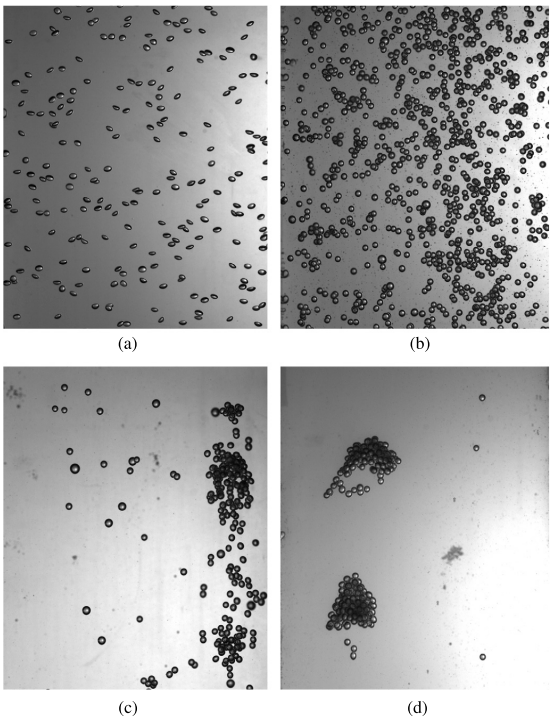

Fig. 3.4. Bubbly flow obtained with capillary bank N3 and $u_s = 0.07$ cm/s in (a) water, (b) glycerol/water, (c) 0.02% XG, and (d) 0.1% XG. The images are recorded with slightly different spatial resolutions. The images are acquired at column height of approximately 110 cm.

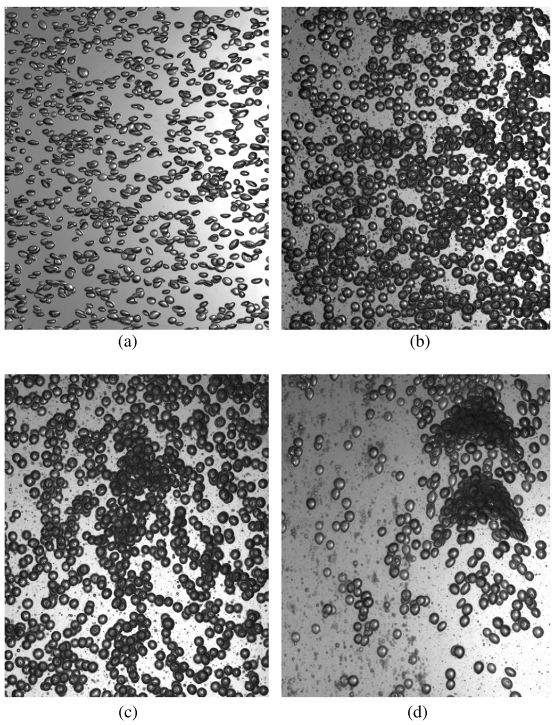

Fig. 3.5. Bubbly flow obtained with capillary bank N3 and $u_s = 0.47$ cm/s in (a) water, (b) glycerol/water, (c) 0.02% XG, and (d) 0.1% XG. The images are recorded with slightly different spatial resolutions. The images are acquired at column height of approximately 110 cm.

are distributions of d (mean Feret diameter) from which d_b (Sauter mean diameter) is calculated. The density distribution function, q, represents the number of bubbles in a defined bubble diameter class. The blue bar denotes the arithmetic mean, and the red bar the d_b of the respective bubble size distribution. As previously mentioned, a narrow bubble size distribution is desirable as it increases the certainty in the interpreted effect of a on $k_L a$. With a broad bubble size distribution, it is not possible to characterize how the various bubble sizes in the size distribution contribute to $k_L a$. Hence, having a wide bubble size distribution increases the uncertainty of the interpreted effect of a on $k_L a$.

Table 3.1 presents the maximum and minimum standard deviations of the bubble size distributions in water and glycerol/water, and the maximum and minimum number of bubbles within ±0.5 mm of the arithmetic mean in water and glycerol/water. The values presented in Table 3.1 correspond to the bubble size distributions in Figs. 3.9 and 3.10. The smallest standard deviations for capillary banks N3 and N2 in Table 3.1 are obtained for $u_s = 0.07$ cm/s in both water and glycerol/water. The smallest standard deviations for capillary bank N1 are obtained for $u_s = 0.29$ cm/s and $u_s = 0.4$ cm/s in water and glycerol/water, respectively. The standard deviations increase with an increase in u_s for all the capillary banks independent of the liquid solutions. The high percentages of bubbles within ±0.5 mm of the arithmetic means in Table 3.1 (b) give a quantitative validation of the ability of the capillary banks to produce mono-sized bubbles.

Table 3.2 provides an overview of the determined d_b in the different liquid solutions.

Table 3.1
(a) Maximum and minimum standard deviations of the bubble size distributions in water and glycerol/water for the various capillary banks and u_s, and (b) maximum and minimum number of bubbles within ±0.5 mm of the arithmetic mean in water and glycerol/water for the various capillary banks and u_s.

		Water		Glycerol/water	
		min	max	min	max
(a)	N3	9%	13%	8%	10%
	N2	7%	11%	7%	9%
	N1	10%	12%	7%	7%
(b)	N3	90%	97%	90%	98%
	N2	90%	97%	90%	99%
	N1	78%	84%	91%	93%

3.3. Gas hold-up and interfacial area

Fig. 3.11 illustrates the effect of liquid properties and u_s on α_G. Comparing the Newtonian solutions in Figs. 3.11 (a-b), α_G obtained by capillary banks N2 and N3 in glycerol/water is approximately the double of that found in water. The higher viscosity of glycerol/water increases the drag force acting on the bubbles and results in a reduced bubble rise velocity (increased residence time) and thus an increase in α_G. α_G in 0.1% XG is considerably lower than α_G in glycerol/water. This can be explained by the presence of bubble clusters which have a larger rise velocity (lower residence time) and hence reduces α_G. In 0.02% XG, bubble clusters are only obtained with capillary bank N3 at the low-

Table 3.2
d_b produced by the capillary banks in the liquid solutions.

	Capillary bank	Water	Glycerol/water	0.02% XG	0.1% XG
d_b	N1	[4.9, 5.0, 5.3]	[4.7, 4.9, 5.2]	[5.0, 5.2]	[5.5, 5.6]
	N2	[3.1, 3.2, 3.3, 3.5, 3.6]	[2.8, 3.3, 3.8]	[2.9, 4.1]	[3.3, 4.1, 4.6]
	N3	[2.4, 2.5, 2.8, 2.9]	[2.3, 3.1, 3.5]	[2.5, 3.4]	[2.7, 3.4, 3.9]

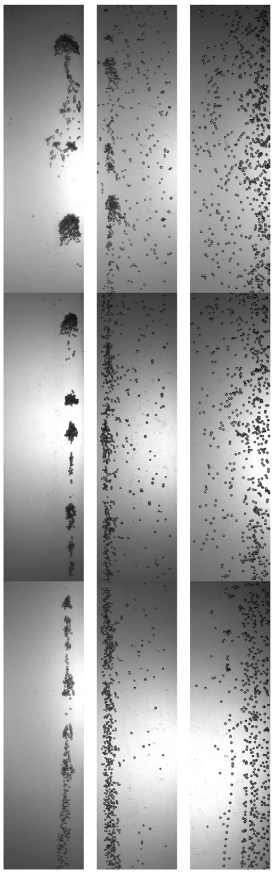

Fig. 3.6. Bubble flow field at $u_s = 0.07$ cm/s in (a) 0.1% XG using capillary bank N3, (b) 0.02% XG using capillary bank N3, and (c) 0.02% XG using capillary bank N2. The images taken in the lower-, mid-, and upper part of the bubble column have been concatenated. The column height and width presented in the images are of size 100×9 cm^2.

est u_s, where the number of bubbles constituting a cluster is lower and the number of single bubbles is higher compared to 0.1% XG. α_G is thus larger in 0.02% XG compared to 0.1% XG. α_G obtained with capillary bank N1 in glycerol/water and 0.02% XG are significantly lower than those obtained with capillary banks N2 and N3. In glycerol/water and 0.02% XG, the bubbles produced by capillary bank N1 are larger than those produced by capillary banks N2 and N3 (for the respective solutions) and thus have a larger rise velocity and lower residence time. Some coalescence is observed for capillary bank N1 in glycerol/water which leads to formation of cap bubbles. The number of cap bubbles, however, is low and the bubble flow is dominated by mono-sized bubbles.

The uncertainty in a can be calculated from the propagation of the error formula (Navidi, 2008):

$$(\delta a)^2 = \left(\frac{\partial a}{\partial \alpha_G}\delta\alpha_G\right)^2 + \left(\frac{\partial a}{\partial d_b}\delta d_b\right)^2 \tag{9}$$

$$= \left(\frac{6}{d_b}\delta\alpha_G\right)^2 + \left(\frac{-6\alpha_G}{d_b^2}\delta d_b\right)^2 \tag{10}$$

where δa denotes the uncertainty in a, $\delta\alpha_G$ the uncertainty in α_G, and δd_b the uncertainty in d_b.

Fig. 3.12 (a) shows an increase in a with an increase in u_s for all the capillary banks in water. a increases as a result of the larger increase in α_G relative to d_b with an increase in u_s. α_G obtained in water is close to equal for the capillary banks, and the largest and smallest a are therefore obtained by the smallest and largest bubbles, respectively. For capillary banks N2 and N3 in glycerol/water (Fig. 3.12 (b)), a increases with an increase in u_s, where the smallest and largest bubbles lead to higher and lower a, respectively. The low a obtained by capillary bank N1 in glycerol/water can be explained by the corresponding small α_G and large d_b. a obtained with capillary banks N2 and N3 in 0.02% XG (Fig. 3.12 (c)) is lower compared to glycerol/water due to the larger d_b and smaller α_G. The variation in d_b produced by capillary bank N1 at $u_s \in [0.4, 0.47]$ cm/s in water, glycerol/water, and 0.02% XG is within the uncertainty in d_b, and hence d_b is concluded to be independent of the solutions for the given u_s. Furthermore, α_G obtained by capillary bank N1 is equal for glycerol/water and 0.02% XG, and thus the obtained a is equal for glycerol/water and 0.02% XG.

3.4. Volumetric mass transfer coefficient

Fig. 3.13 presents k_La as a function of u_s for the different liquid solutions. In water (Fig. 3.13 (a)), k_La increases with increasing u_s for all the capillary banks. The highest k_La is obtained by capillary bank N3, producing the smallest bubbles with the largest a. By contrast, the lowest k_La is achieved with capillary bank N1, producing the largest bubbles with the smallest a. Increasing the liquid viscosity negatively affects the rate of mass transfer. As shown in Fig. 3.13, k_La obtained in water is more than a factor of ten larger than that obtained in 0.1% XG, 0.02% XG, and glycerol/water. k_La obtained in 0.02% XG and 0.1% XG is larger compared to that obtained in glycerol/water for all $u_s > 0.07$ cm/s. As it was shown in Fig. 2.3, the viscosities of 0.1% XG and 0.02% XG decrease below that of glycerol/water for $\dot{\gamma}$ of 2 s^{-1} and 10 s^{-1}, respectively. To relate the shear rate to u_s, Nishikawa et al. (1977) proposed the correlation $\dot{\gamma} = 100u_s^{1/2}$ for $u_s < 4$ cm/s and at the center of the bubble column. The correlation by Nishikawa et al. (1977) was derived based on fitting heat transfer coefficients measured in Newtonian and non-Newtonian solutions. For the u_s-values in the present study, their correlation results in $\dot{\gamma} \in [27, 67]$ s^{-1}. Schumpe and Deckwer (1987) proposed the correlation $\dot{\gamma} = 2800u_s$, which was derived based on fitting values of k_La in Newtonian and non-Newtonian solutions (e.g., XG) for $u_s > 2$ cm/s. Using the correlation by Schumpe and Deckwer (1987) for the present study results in $\dot{\gamma} \in [2, 13]$ s^{-1}. The estimations of $\dot{\gamma}$ in the present bubble column are rough estimates as the systems and operating conditions used by Nishikawa et al. (1977) and Schumpe and Deckwer (1987) are different from the present set-up. However, the estimations indicate that the viscosities of the non-Newtonian solutions are decreasing below that of glycerol/water, which reduce the resistance to mass transfer and can explain the larger values of k_La for the non-Newtonian

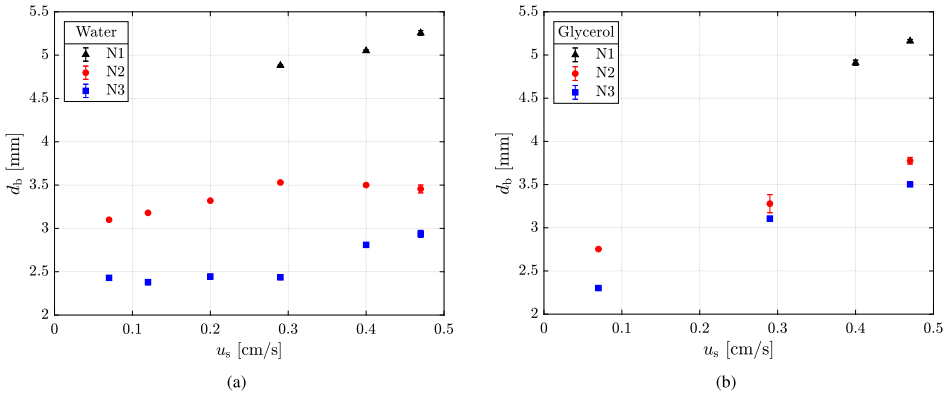

Fig. 3.7. Bubble diameter as function of superficial gas velocity in (a) water and (b) glycerol/water.

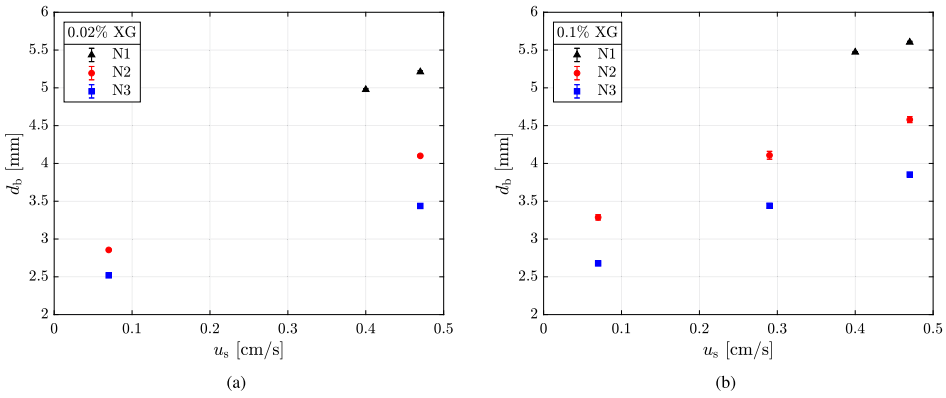

Fig. 3.8. Bubble diameter of single bubbles as function of superficial gas velocity in (a) 0.02% XG and (b) 0.1% XG.

solutions compared to glycerol/water. The rate of change of the oxygen concentration in equation (2) is calculated based on the assumption of homogeneous bubble flow. Thus, the computed k_La values in the non-Newtonian solutions are associated with larger uncertainty because the formation of bubble clusters means that the assumption of homogeneous flow is weakened.

For $u_s = 0.07$ cm/s and $u_s = 0.29$ cm/s in 0.1% XG (Fig. 3.13 (d)), the k_La achieved with capillary bank N2 is larger compared to that achieved by capillary bank N3. However, for $u_s = 0.47$ cm/s in 0.1% XG (Fig. 3.13 (d)), the k_La obtained by capillary bank N3 is larger compared to that by capillary bank N2. Increasing u_s from 0.29 cm/s to 0.47 cm/s in 0.1% XG resulted in an increase in the number of bubbles present as individual bubbles in addition to the bubble clusters. Fig. 3.8 (b) shows that the individual bubbles produced by capillary bank N3 are smaller compared to those produced by capillary bank N2. With the same α_G (Fig. 3.11 (d)), by only considering the individual bubbles in the bubble column with capillary bank N3, the measured a-value is larger compared to that obtained with capillary bank N2. This has a positive effect on k_La.

The clusters were expected to negatively influence the mass transfer because many of the bubbles in a cluster are prevented from being well exposed to the surrounding liquid. However, as previously mentioned, the bubble clusters in the shear-thinning solutions are highly dynamic. That is, the interchange of bubble position and the bubble cluster collisions are observed to be highly prominent. The dynamic characteristics of the flow may have had a positive effect on the mass transfer and may explain why the mass transfer in XG was relatively high compared to the homogeneous dispersed flow in glycerol/water. At a shear rate of 2 (s^{-1}), the viscosities of 0.02% XG and 0.1% XG are approximately equal. k_La obtained in 0.1% XG is higher than that obtained in 0.02% XG. The bubble clusters are mainly formed in 0.1% XG, and hence the dynamic characteristics of the flow due to the bubble clusters may explain the larger k_La obtained in 0.1% XG compared to that obtained in 0.02% XG.

The largest standard deviations of k_La in 0.1% XG were 3%, 5%, and 4% for capillary banks N3, N2, and N1, respectively. For 0.02% XG, the largest standard deviations were 4%, 3%, and 3% for capillary banks N3, N2, and N1, respectively.

3.5. Liquid mass transfer coefficient

k_L in water is shown by Fig. 3.14 (a) to decrease with an increase in u_s. Table 3.3 provides the relative change in k_L for the capillary banks in water, glycerol/water, and 0.02% XG. The relative change in a in water is 143%, 149%, and 54% for capillary banks N3, N2, and N1, respectively. With increasing u_s in water, the decrease in k_L is much smaller than the increase in a, and the change in k_La is mainly caused by a. In glycerol/water (Fig. 3.14 (b)), k_L decreases with an increase in u_s. For capillary banks N3 and N2 in glycerol/water, k_L mainly decreases between $u_s = 0.07$ cm/s and $u_s = 0.29$ cm/s, where the relative change is 43% and 47%, respectively. Between $u_s = 0.29$ cm/s and $u_s = 0.47$ cm/s, the relative change in k_L is 14% for capillary bank N3 and 6% for capillary bank N2. The relative change in a for capillary banks N3 and N2 in glycerol/water (110% and 122%, respectively) is much larger than that

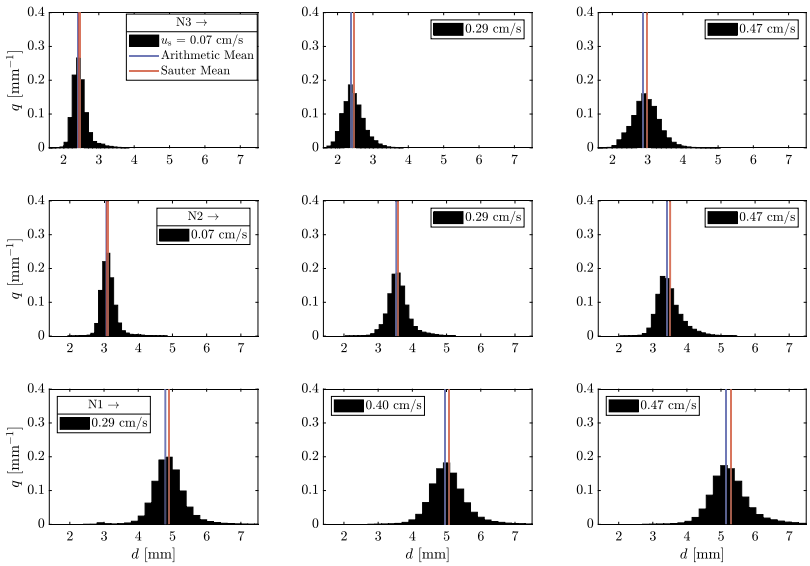

Fig. 3.9. Bubble size distributions in water where $u_s = [0.07, 0.29, 0.47]$ cm/s for capillary bank N3 (top row) and capillary bank N2 (middle row), and $u_s = [0.29, 0.4, 0.47]$ cm/s for capillary bank N1 (bottom row).

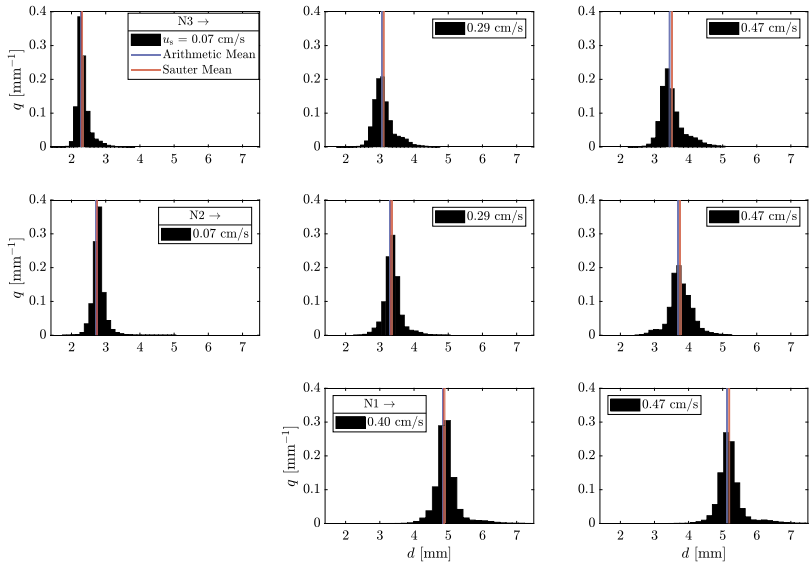

Fig. 3.10. Bubble size distributions in glycerol/water where $u_s = [0.07, 0.29, 0.47]$ cm/s for capillary bank N3 (top row) and capillary bank N2 (middle row), and $u_s = [0.4, 0.47]$ cm/s for capillary bank N1 (bottom row).

of k_L, and thus the change in $k_L a$ is mainly attributed to a. In 0.02% XG, k_L decreases with an increase in u_s for capillary banks N3 and N2. Bubble clusters are formed for capillary bank N3 at $u_s = 0.07$ cm/s and may influence the value. For capillary banks N3 and N2, the increase in a (relative change is 110% and 122%, respectively) is much larger than the decrease in k_L, and a is thus mainly causing the change in $k_L a$. For capillary bank N1 in 0.02% XG, k_L at $u_s = 0.4$ cm/s is within the standard deviation of k_L at $u_s = 0.47$ cm/s. The change in a (relative change of 9%) for capillary bank N1 in 0.02% XG causes a slight increase in $k_L a$.

The uncertainty in k_L can be calculated by the propagation of the error formula:

$$(\delta k_L)^2 = \left(\frac{\partial k_L}{\partial k_L a}\delta k_L a\right)^2 + \left(\frac{\partial k_L}{\partial a}\delta a\right)^2 \tag{11}$$

$$= \left(\frac{1}{a}\delta k_L a\right)^2 + \left(\frac{-k_L a}{a^2}\delta a\right)^2 \tag{12}$$

where δk_L denotes the uncertainty in k_L, $\delta k_L a$ the uncertainty in $k_L a$, and δa the uncertainty in a.

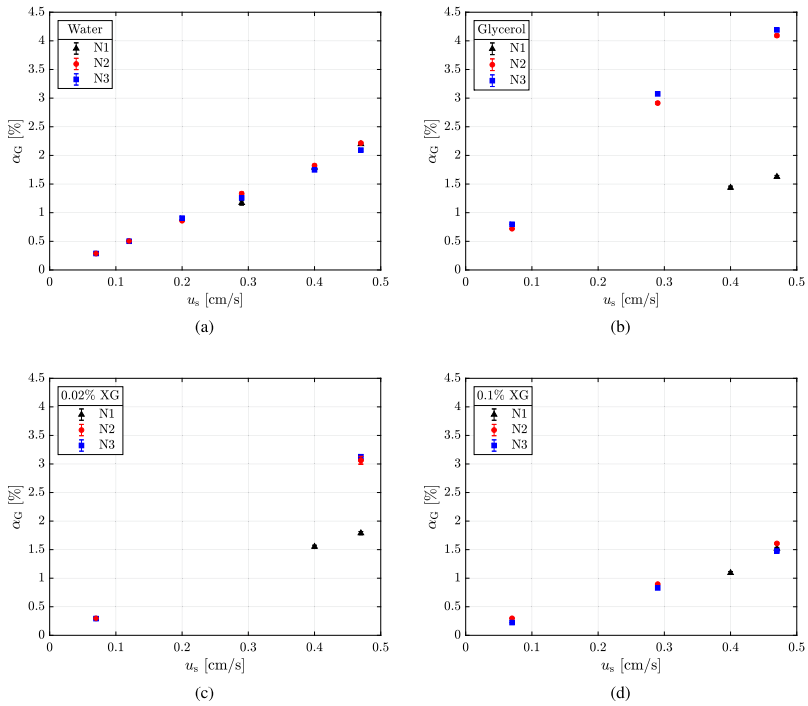

Fig. 3.11. Gas hold-up as function of superficial gas velocity in (a) water, (b) glycerol/water, (c) 0.02% XG, and (d) 0.1% XG.

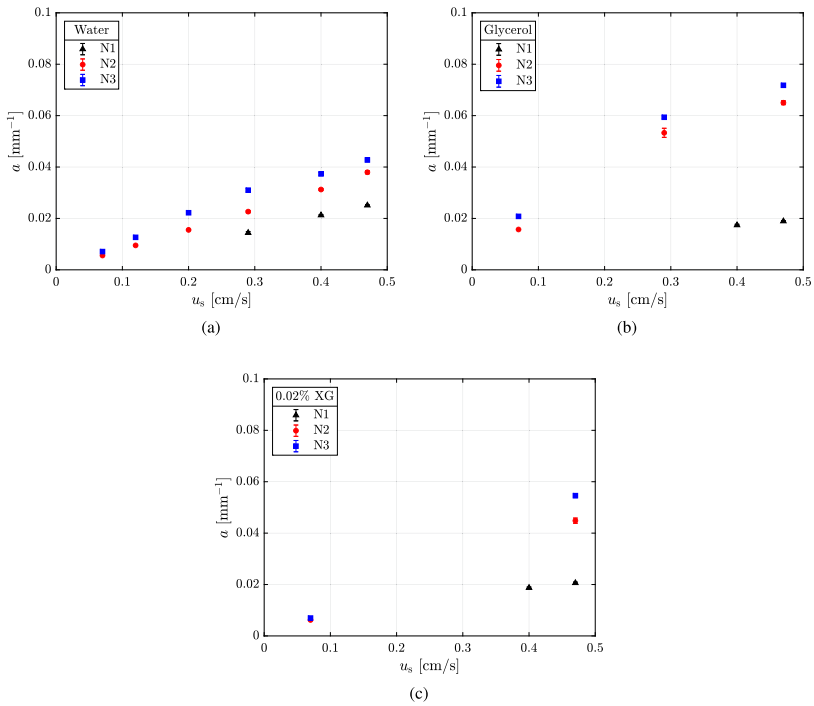

Fig. 3.12. Interfacial area as function of superficial gas velocity in (a) water, (b) glycerol/water, and (c) 0.02% XG.

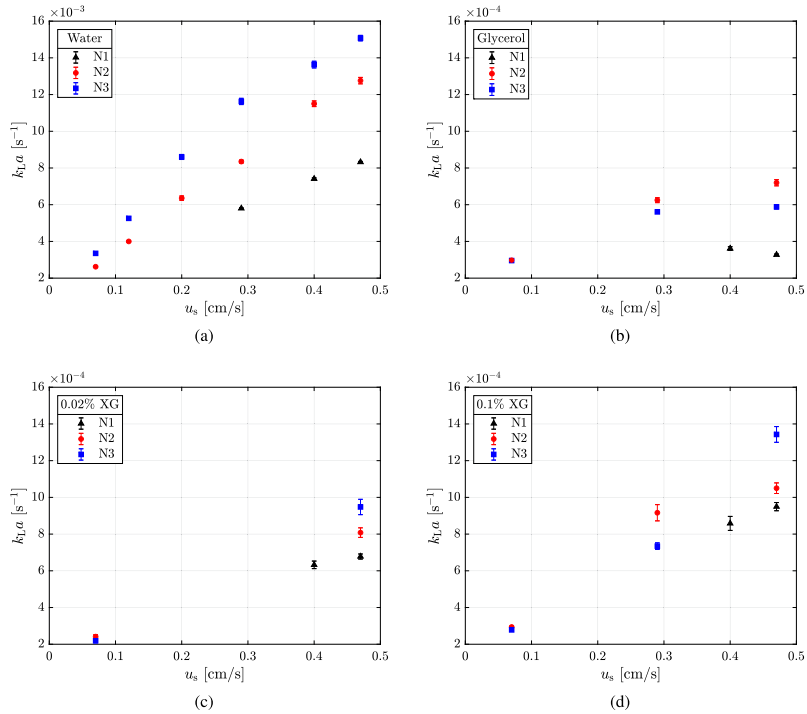

Fig. 3.13. Volumetric mass transfer coefficient as function of superficial gas velocity in (a) water, (b) glycerol/water, (c) 0.02% XG, and (d) 0.1% XG.

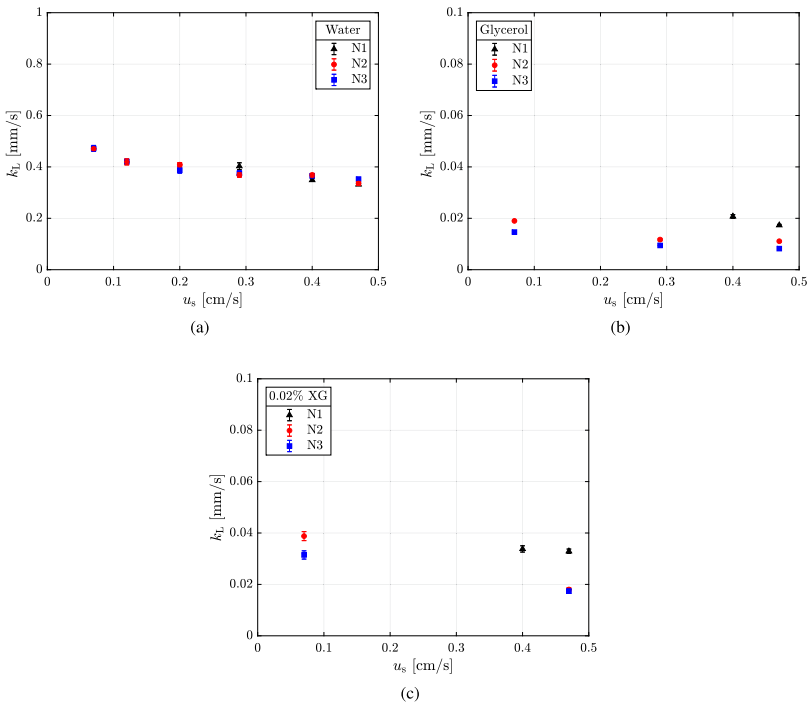

Fig. 3.14. Liquid-side mass transfer coefficient as function of superficial gas velocity in (a) water, (b) glycerol/water, and (c) 0.02% XG.

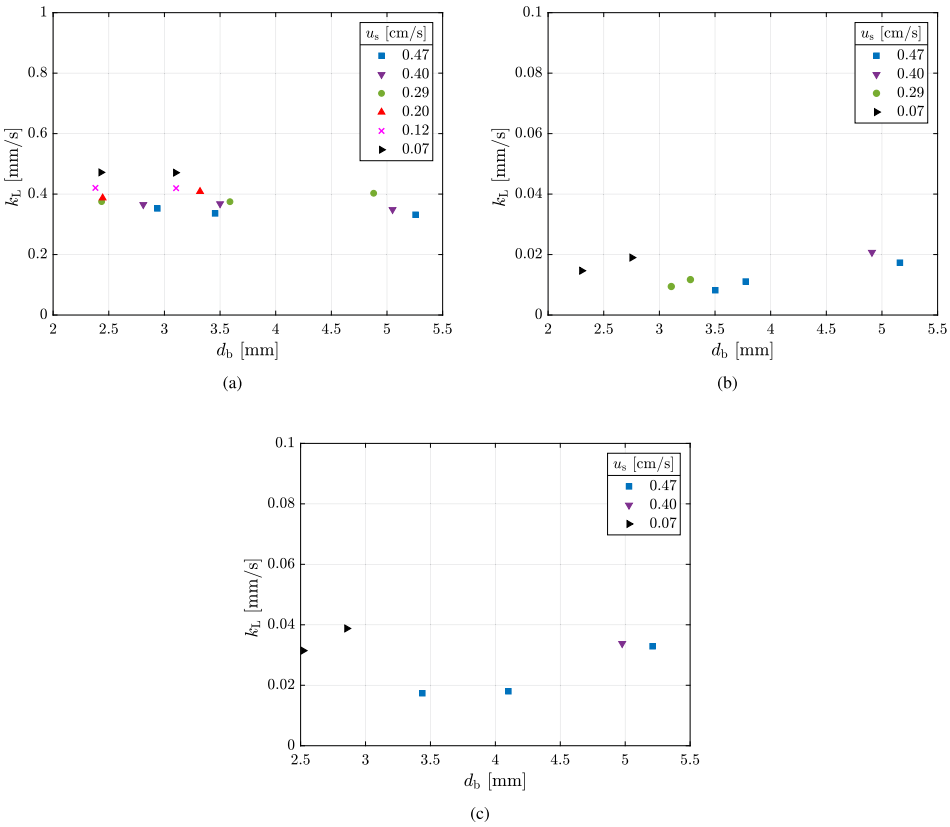

Fig. 3.15. Liquid-side mass transfer coefficient as function of bubble diameter in (a) water, (b) glycerol/water, and (c) 0.02% XG.

Table 3.3
Relative change in k_L. The relative change is here defined as $(p_{s,1} - p_{s,2})/(p_{s,1} + p_{s,2})/2$, where $p_{s,1}$ is the value of k_L at $u_s = 0.07$ cm/s for capillary banks N3 and N2, and $u_s = 0.4$ cm/s for capillary bank N1, and $p_{s,2}$ is the value of k_L at $u_s = 0.47$ cm/s.

	Water	Glycerol/water	0.02% XG
N3	29%	56%	58%
N2	33%	53%	73%
N1	19%	18%	3%

The largest standard deviations in 0.02% XG are 5% for capillary bank N3, 5% for capillary bank N2, and 4% for capillary bank N1.

k_L is shown as function of d_b in Fig. 3.15. At a given u_s in water, k_L is independent of d_b (Fig. 3.15 (a)). In glycerol/water and 0.02% XG, k_L increases with an increase in d_b at a given u_s.

4. Concluding remarks

Despite the extensive research on mass transfer in bubble columns, most of the studies are performed in Newtonian solutions, where the volumetric mass transfer coefficient $k_L a$ is determined. Only a limited number of experimental studies in Newtonian solutions exist where the individual contributions of k_L and a to $k_L a$ have been examined, and the number of studies in non-Newtonian solutions is even more limited. Motivated by industrial application such as bioprocesses, in which the fluids commonly show non-Newtonian behavior, the individual contributions of k_L and a on $k_L a$ should be further extended to viscous Newtonian and non-Newtonian solutions to increase the understanding of the complex mechanisms involved.

In this study, mass transfer and bubble hydrodynamics in Newtonian and non-Newtonian solutions were investigated in a bubble column. $k_L a$ was calculated from measurements of the local DO concentration. a was calculated based on d_b and α_G. k_L was estimated by combining $k_L a$ and a. The effects of operating conditions and liquid rheology on the mass transfer and bubble hydrodynamics were evaluated. The data from this work contributes to the experimental data necessary in developing and validating multiphase models. The main findings can be summarized as:

- The designs of the capillary banks enabled production of bubbles with a narrow bubble size distribution.

- α_G and a increased with u_s. For capillary bank N1, a was independent of the viscosity. The formation of bubble clusters reduced the residence time, hence the lowest α_G was obtained in 0.1% XG.
- $k_L a$ increased with increasing u_s and was negatively affected by the viscosity. The formation of bubble clusters did not have a prominent effect on $k_L a$. This may be explained by the highly dynamic bubble clusters of which the interchange of bubble position and cluster collisions are highly prominent. Furthermore, the dynamic flow characteristics may affect the apparent viscosity of the shear-thinning liquid in the vicinity of the bubble clusters more prominent because the bubble clusters have a higher rise velocity than small and individual bubbles. The influence of the complex dynamic flow characteristics of the bubble clusters on the mass transfer is still not fully understood, and further work on the mechanisms involved is necessary.
- The relative change in k_L was much lower than the relative change in a in water, glycerol/water, and 0.02% XG. For the investigated operational conditions and liquid solutions, the change in $k_L a$ was mainly attributed to a.
- At a given u_s, k_L was independent of d_b in water, whereas k_L increased with an increase in d_b in glycerol/water and 0.02% XG.

CRediT authorship contribution statement

Ida K. Kure: Conceptualization, Data curation, Formal analysis, Investigation, Methodology, Software, Writing – original draft. **Hugo A. Jakobsen:** Conceptualization, Supervision, Writing – review & editing. **Jannike Solsvik:** Conceptualization, Supervision, Writing – review & editing.

Declaration of competing interest

The authors declare that they have no known competing financial interests or personal relationships that could have appeared to influence the work reported in this paper.

Data availability

Data will be made available on request.

Appendix A

Figs. A.1-A.3 present different flow patterns obtained with the capillary banks, operated at various gas flow rates in 0.1% XG. The images are captured at different u_s to show the impact of the gas flow rates on the cluster shapes and formation of individual bubbles. Figs. A.1 (a-c) and A.2 (a-c) show the tendency of a horizontal orientation of the bubble clusters for $u_s = 0.07$ cm/s. When u_s increases, a vertical orientation is observed in Figs. A.1 (d-j) and A.2 (d-j) to dominate the bubble clusters. The number of individual bubbles formed in addition to the bubble clusters increases when u_s increases for all the capillary banks.

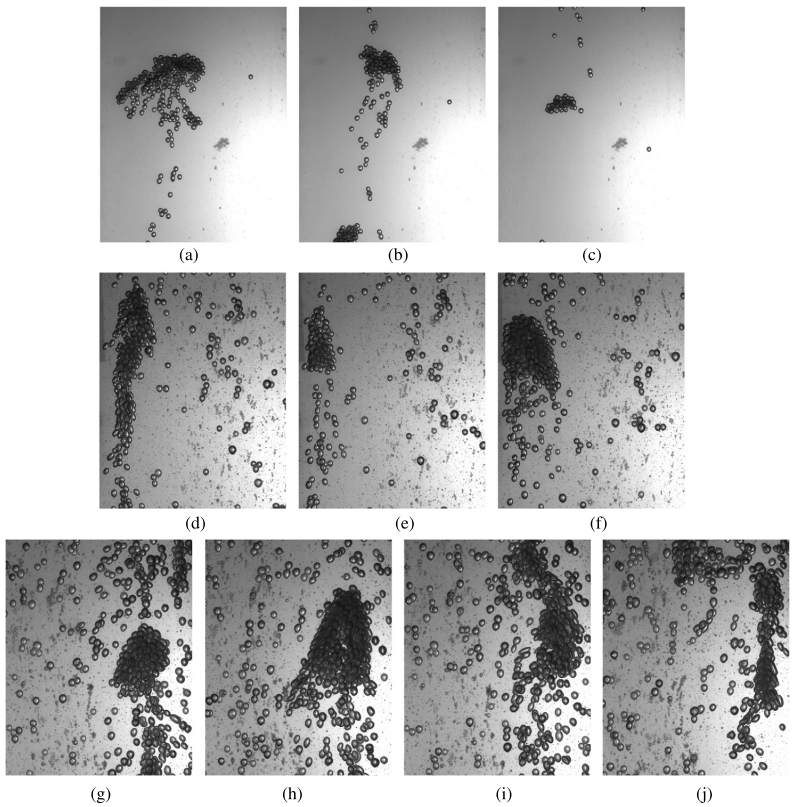

Fig. A.1. Bubble cluster shapes produced with capillary bank N3 in 0.1% XG at: (a-c) $u_s = 0.07$ cm/s, (d-f) $u_s = 0.29$ cm/s, and (g-j) $u_s = 0.47$ cm/s.

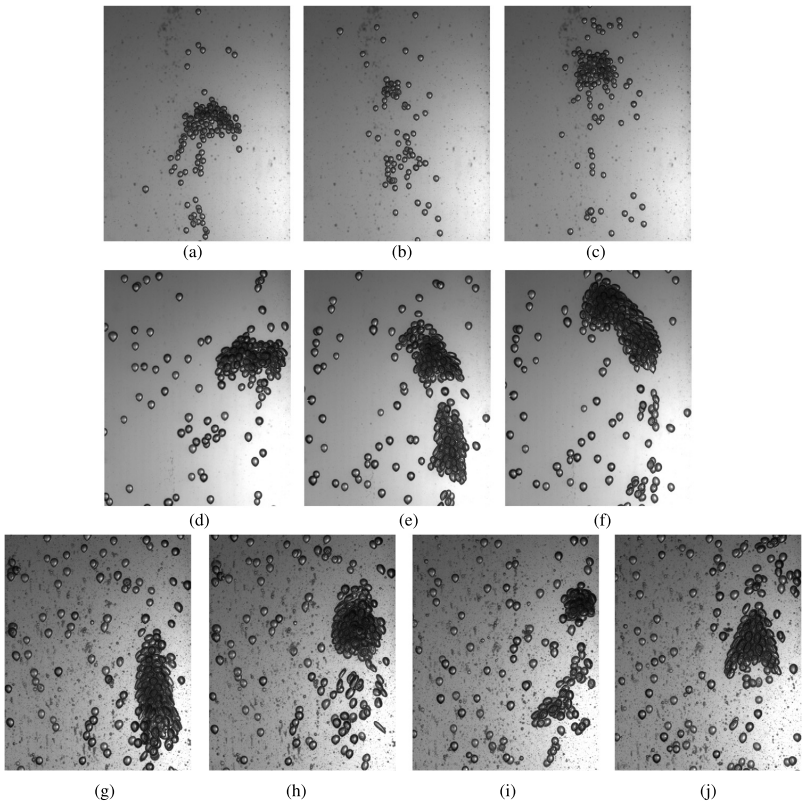

Fig. A.2. Bubble cluster shapes produced with capillary bank N2 in 0.1% XG at: (a-c) $u_s = 0.07$ cm/s, (d-f) $u_s = 0.29$ cm/s, and (g-j) $u_s = 0.47$ cm/s.

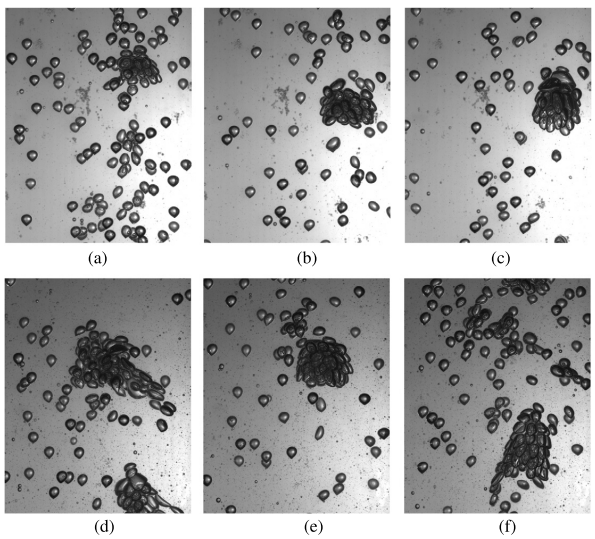

Fig. A.3. Bubble cluster shapes produced with capillary bank N1 in 0.1% XG at: (a-c) $u_s = 0.4$ cm/s, and (d-f) $u_s = 0.47$ cm/s.

References

Akita, K., Yoshida, F., 1973. Gas holdup and volumetric mass transfer coefficient in bubble columns. Ind. Eng. Chem. Process Des. Dev. 12, 76–80.

Akita, K., Yoshida, F., 1974. Bubble size, interfacial area, and liquid-phase mass transfer coefficient in bubble columns. Ind. Eng. Chem. Process Des. Dev. 13, 84–91.

Augier, F., Raimundo, P.M., 2021. Effect of rheology on mass transfer and bubble sizes in a bubble column operated in the heterogeneous regime. Can. J. Chem. Eng. 99, 1177–1185.

Badino, A., Facciotti, M., Schmidell, W., 1976. Volumetric mass transfer coefficients (k_La) in batch cultivations involving non-Newtonian broths. Biotechnol. Bioeng. 18, 745–790.

Blanch, H., Bhavaraju, S., 1976. Non-Newtonian fermentation broths: rheology and mass transfer. Biotechnol. Bioeng. 18, 745–790.

Bouaifi, M., Hebrard, G., Bastoul, D., Roustan, M., 2001. A comparative study of gas hold-up, bubble size, interfacial area and mass transfer coefficients in stirred gas–liquid reactors and bubble columns. Chem. Eng. Process. 40, 97–111.

Doran, P.M., 2013. Bioprocess Engineering Principles, 2nd edition. Elsevier Ltd.

Eckenfelder Jr., W.W., Barnhart, E.L., 1961. The effect of organic substances on the transfer of oxygen from air bubbles in water. A. I. Ch. E. Journal 7, 631–634.

Emmerich, J., Tang, Q., Wang, Y., Neubauer, P., Junne, S., Maaß, S., 2019. Optical inline analysis and monitoring of particle size and shape distributions for multiple applications: scientific and industrial relevance. Chin. J. Chem. Eng. 27, 257–277.

Garcia-Ochoa, F., Gomez, E., 2009. Bioreactor scale-up and oxygen transfer rate in microbial processes: an overview. Biotechnol. Adv. 27, 153–176.

Gemello, L., Plais, C., Augier, F., Cloupet, A., Marchisio, D., 2018. Hydrodynamics and bubble size in bubble columns: effects of contaminants and spargers. Chem. Eng. Sci. 184, 93–102.

Irgens, F., 2014. Rheology and Non-Newtonian Fluids. Springer.

Jakobsen, H.A., 2014. Chemical Reactor Modeling: Multiphase Reactive Flows, 2nd ed. Springer, Berlin.

Jeng, J.J., Maa, J.R., Yang, Y.M., 1986. Surface effects and mass transfer in bubble column. Ind. Eng. Chem. Process Des. Dev. 25, 974–978.

Kawase, Y., Moo-Young, M., 1990. The effect of antifoam agents on mass transfer in bioreactors. Bioprocess Eng. 5, 169–173.

Koide, K., Yamazoe, S., Harada, S., 1985. Effects of surface-active substances on gas holdup and gas-liquid mass transfer in bubble column. J. Chem. Eng. Jpn. 18, 287–292.

Lessard, R., Zieminski, S., 1971. Bubble coalescence and gas transfer in aqueous electrolytic solutions. Ind. Eng. Chem. Fundam. 10, 260–269.

Martínez-Mercado, J., Palacios-Morales, C.A., Zenit, R., 2007. Measurement of pseudoturbulence intensity in monodispersed bubbly liquids for $10 < Re < 50$. Phys. Fluids 19.

Miller, D.N., 1983. Interfacial area, bubble coalescence and mass transfer in bubble column reactors. AIChE J. 29, 312–319.

Muroyama, K., Imai, K., Oka, Y., Hayashi, J., 2013. Mass transfer properties in a bubbles column associated with micro-bubble dispersions. Chem. Eng. Sci. 100, 464–473.

Navidi, W., 2008. Statistics for Engineers and Scientists, 2nd ed. McGraw-Hill International Edition.

Nishikawa, M., Kato, H., Hashimoto, K., 1977. Heat transfer in aerated tower filled with non-Newtonian liquid. Ind. Eng. Chem. Process Des. Dev. 16, 133–137.

Sastaravet, P., Bun, S., Wongwailikhit, K., Chawaloesphonsiya, N., Fujii, M., Painmanakul, P., 2020. Relative effect of additional solid media on bubble hydrodynamics in bubble column and airlift reactors towards mass transfer enhancement. Processes 8.

Scargiali, F., Busciglio, A., Grisafi, F., Brucato, A., 2010. Simplified dynamic pressure method for k_La measurement in aerated bioreactors. Chem. Eng. J. 49, 165–172.

Schumpe, A., Deckwer, W.-D., 1987. Viscous media in tower bioreactors: hydrodynamic characteristics and mass transfer properties. Bioprocess Eng. 2, 79–94.

Vandu, C., Koop, K., Krishna, R., 2004. Volumetric mass transfer coefficient in a slurry bubble column operating in the heterogeneous flow regime. Chem. Eng. Sci. 59, 5417–5423.

Vasconcelos, J.M.T., Rodrigues, J.M.L., Orvalho, S.C.P., Alves, S.S., Mendes, R.L., Reis, A., 2003. Effect of contaminants on mass transfer coefficients in bubble column and air lift contactors. Chem. Eng. Sci. 58, 1431–1440.

Vélez-Cordero, J.R., Zenit, R., 2011. Bubble cluster formation in shear-thinning inelastic bubbly columns. J. Non-Newton. Fluid Mech. 166, 32–41.

Vélez-Cordero, J.R., Sámano, D., Zenit, R., 2012. Study of the properties of bubbly flows in Borger-type fluids. J. Non-Newton. Fluid Mech. 175–176, 1–9.

Zednikova, M., Orvalho, S., Fialova, M., Ruzicka, M.C., 2018. Measurement of volumetric mass transfer coefficient in bubble columns. Chem. Eng. 2.

Chapter 5

Concluding Remarks and Suggestions for Further Work

5.1 Concluding Remarks

Industrial processes concerning gas–liquid or gas–liquid–solid interactions are often governed by the interfacial mass transfer taking place between the relevant phases. To increase the process performance it is thus crucial to optimize the interfacial mass transfer, e.g., by wisely selecting the reactor design for the specific process. While the phenomena of interfacial mass transfer have been widely studied, the physical and mechanical factors influencing the interfacial mass transfer are still not fully understood. The objective of this work was to enhance the understanding of the interfacial mass transfer phenomena by experimentally investigating single bubbles and bubble swarms.

Single Bubble Experiments

In the first part of the work, an experimental facility was designed and constructed for studying the interfacial mass transfer from single bubbles rising in stagnant liquid. Two high-speed cameras mounted on a sliding movable platform enabled continuous recording of the transient bubble size and velocity during the bubble ascent. To contribute to state-of-the-art, the work provided a detailed description of the control system of the dynamic facility. Prior to the interfacial mass transfer experiments, the bubble hydrodynamics were investigated for single air bubbles rising in stagnant air saturated water. Here, the effects of bubble size and trajectory on the terminal velocity were assessed. The terminal velocity data obtained in this work agreed with literature data obtained in ultra-pure systems and where the bubbles were produced with large initial shape deformations. These results demonstrated the functionality of the experimental facility for studies on single bubble interfacial mass transfer in a pure system. However, while the concept of

producing and tracking an individual bubble is simple, the execution was found to be very challenging and time consuming mainly due to following reasons:

- Producing individual bubbles of diameter < 1 mm was challenging. Furthermore, producing bubbles within a specific size range was time consuming as each glass needle was handmade and unique, and thus several glass needles with different inner diameter had to be employed to cover the size range.

- Adapting the velocity of the sliding movable platform (on which the two high-speed cameras were mounted) to the velocity of the bubble was challenging due to the mechanical delay in the sliding platform. The mechanical delay caused a time delay in the adaption of the sliding platform to the velocity of the bubble. This was particularly challenging in the bubble acceleration phase, just after the bubble–needle detachment, which resulted in the bubbles frequently moving out of the physical space captured by the camera. To avoid that the bubbles moved out of the camera frame in the acceleration phase, a signal was sent to the sliding platform prior to the bubble injection. In the acceleration phase, the bubbles moved in and out of the camera frame within approximately $0.04 - 0.07$ s, and thus timing the signal to the sliding platform prior to the bubble injection required several attempts and was time consuming. Furthermore, the mechanical delay caused several bubbles to move out of the camera frame during the ascent as the bubble diameter and thus velocity changed due to the interfacial mass transfer and hydrostatic pressure gradient. Thus, several attempts were required to capture and track the bubbles along the tall vertical column. In future studies, it is therefore recommended to use a sliding movable platform with fine mechanics to avoid mechanical delays.

In the interfacial mass transfer study, single CO_2 bubbles were injected into stagnant deionized water. Bubbles in the diameter range of $d_\mathrm{b} \in [0.7 - 3.0]$ mm were investigated. An expression for k_L was derived in a Lagrangian framework and was computed from the measured quantities of bubble surface area, bubble volume, vertical position in the column, and their time derivatives. A Lagrangian model description was used with various k_L-correlations to perform numerical simulations of the change in bubble volume during the bubble rise. The main findings from the single bubble interfacial mass transfer study are:

- k_L was a function of the initial bubble diameter and the bubble–liquid exposure time.

- A maximum value of k_L was obtained for bubbles with initial diameter in the size range of $2.1 - 2.3$ mm.
- For bubbles with a mean diameter ≤ 2.8 mm, the mean k_L decreased with decreasing mean bubble diameter. Here, the mean d_b and k_L were calculated as average values from t=0 to the time k_L attained a steady value.
- The k_L-correlations used in the Lagrangian model gave very different simulation results and failed to accurately predict the experimentally observed change in bubble volume with respect to time. The fundamental principles of interfacial mass transfer, even in simple systems such as single bubbles rising in stagnant liquid, are not fully understood, and new k_L-models must be derived based on new experimental data such as those in this work.

Bubble Swarm Experiments

In the second part of this work, the interfacial mass transfer of bubble swarms was studied in liquids exhibiting Newtonian and non-Newtonian rheological behavior. The study included the effects of bubble size, liquid rheology, sparger design, and gas flow rate on the interfacial mass transfer. Furthermore, it was of interest to study the influence of bubble cluster formation on the interfacial mass transfer, as this to the authors' knowledge, has not been experimentally examined prior to this work. The images recorded by a high-speed camera were processed by an image analysis algorithm using ANN, which allowed for evaluation of large data-sets. Training the ANN with a large set of recorded images (which covered the different liquid solutions and gas volume fractions) resulted in a high bubble detection rate by the ANN. For the systems where the gas phase was dispersed as single bubbles, the ANN calculated the bubble size with a high statistical accuracy. For the systems including bubble clusters, further training of the ANN is necessary for the image algorithm to successfully determine the size of the different bubble clusters. The designs of the gas spargers enabled formation of bubbles with a narrow bubble size distribution and avoid formation of gas jets. Producing bubbles with a narrow bubble size distribution increased the certainty in the interpreted effect of a on k_La. The main findings from the interfacial mass transfer study from bubble swarms are:

- For the liquid solutions and operating conditions, the change in k_La was mainly attributed to the change in a.
- k_L was found to depend on the viscosity and superficial gas velocity, where

k_L decreased with an increase in the viscosity and with an increase in the superficial gas velocity.

- For a given superficial gas velocity, k_L was independent of d_b in water ($d_b \in [2.4, 5.3]$ mm), whereas k_L increased with an increase in d_b in glycerol/water ($d_b \in [2.3, 5.2]$ mm) and 0.02% Xanthan gum ($d_b \in [2.5, 5.2]$ mm).
- Bubble clusters were formed in the non-Newtonian solutions, but for the operating conditions and liquid solutions in this study, the bubble cluster formation did not have a prominent effect on the interfacial mass transfer.

5.2 Suggestions for Further Work

In this dissertation, the interfacial mass transfer phenomena for single bubbles are studied in a low viscous Newtonian liquid, whereas the bubble swarm investigations include both Newtonian and non-Newtonian liquids. The experimental results for k_L obtained with the single bubble system and the bubble swarm system can thus be compared for the low viscous Newtonian liquids only. Future experiments are therefore recommended to consider single bubble studies in viscous Newtonian and non-Newtonian liquids. Furthermore, while several studies have investigated the interfacial mass transfer from single bubbles in contaminated systems (Koide et al., 1974, 1976; Hosoda et al., 2014; Aoki et al., 2015, 2017; Hori et al., 2017), these studies have focused on bubbles with $d_b > 5$ mm. It is suggested to study k_L for single bubbles rising in stagnant contaminated liquid for the bubble diameter range investigated in this dissertation ($0.7 - 3.0$ mm). Comparison of k_L-data for single bubbles in the size range of $d_b \in [0.7, 3.0]$ mm obtained in stagnant contaminated liquid with the results from the pure system in this dissertation, may lead to a greater understanding of the cause of the time effect on k_L.

A next step in understanding the effects of bubble cluster formation on interfacial mass transfer, is to examine k_L and a in the non-Newtonian solutions where bubble clusters are present. The image analysis algorithm employed in this work should be further developed to sufficiently detect the bubble clusters and estimate their size. This will allow for computation of a, and hence k_L can be determined from the measured quantities of $k_L a$ and a.

The global gas hold-up in the bubble swarm experiments is estimated by visually observing the height difference resulting from the dispersed gas. The standard deviation of the gas hold-up was calculated from the repeat of measurements and found to be small in this work. However, the calculated standard deviation does

not give a quantitative measure of the uncertainty in the measurement method itself. It is therefore recommended to introduce other methods for measuring the gas hold-up, e.g., using an optical probe such as in the work of Augier and Raimundo (2021). Furthermore, while the dynamic method offers a straight forward method for measuring $k_{\mathrm{L}}a$, it has limitations due to the assumptions of well mixed liquid phase, negligible probe response time, and that the gas phase dynamics can be ignored (Doran, 2013). Considering an alternative measurement method for $k_{\mathrm{L}}a$ is recommended in future work, especially considering the bubble cluster dynamics observed in this work.

Connecting the interfacial mass transfer mechanisms between single bubbles and bubble swarms is challenging and causes difficulties in improving the mass transfer efficiency based on empirical mass transfer correlations (Bao et al., 2020). To improve the understanding of the complex behavior of interfacial mass transfer and bubble dynamics, it is essential to combine both experimentation and simulation. The following methods are commonly employed for simulating the bubble dynamics on a microscopic level (single bubble behavior): volume of fluid (VOF) method, the level set method, coupled VOF and level set method, and the phase field method (Yan et al., 2023; Soligo et al., 2021). At a macroscopic level (bubble population behavior), the bubble dynamics of bubble swarms are commonly investigated through the population balance method (PBM) (Yan et al., 2023; Solsvik and Jakobsen, 2015). The simulation of gas–liquid interfacial mass transfer may be challenging for several reasons, e.g., long computational time, and huge computational requisition for simulations of industrial devices (Bao et al., 2020). Furthermore, in the classical reactor models (Eulerian framework), k_{L} is implemented as a constant function of time. From the single bubble interfacial mass transfer results in this dissertation, where k_{L} decreased as function of time and approached a value close to zero, it is evident that the implementation of the experimentally determined Lagrangian k_{L} (single bubble experiments) will be different from the experimentally determined Eulerian k_{L} (bubble swarm experiments). The single bubble experiments in this work are studied in laminar flow, whereas the flow field in the bubble swarm experiments is not laminar. In the bubble swarm experiments, there are interactions between the bubbles, liquid circulation, and the bubble hydrodynamics may differ largely from a single bubble in laminar flow. Such flow dynamics are likely to affect the k_{L}-value. Further investigations are required to elucidate how the results from single bubble investigations can be utilized to further improve the models for k_{L} to be used in reactor models derived in Eulerian framework.

Bibliography

United Nations, Climate action and synergies, 2023. URL: https://sdgs.un.org/topics/climate-action-synergies.

Intergovernmental Panel on Climate Change, Reports, 2023. URL: https://www.ipcc.ch/reports/.

United Nations, The 17 goals, 2023. URL: https://sdgs.un.org/goals.

K. Akita, F. Yoshida, Gas holdup and volumetric mass transfer coefficient in bubble columns, Industrial and Engineering Chemistry Process Design and Development 12 (1973) 76–80.

C. Vandu, K. Koop, R. Krishna, Volumetric mass transfer coefficient in a slurry bubble column operating in the heterogeneous flow regime, Chemical Engineering Science 59 (2004) 5417–5423.

F. Scargiali, A. Busciglio, F. Grisafi, A. Brucato, Simplified dynamic pressure method for k_La measurement in aerated bioreactors, Chemical Engineering Journal 49 (2010) 165–172.

K. Muroyama, K. Imai, Y. Oka, J. Hayashi, Mass transfer properties in a bubbles column associated with micro-bubble dispersions, Chemical Engineering Science 100 (2013) 464–473.

M. Zednikova, S. Orvalho, M. Fialova, M. C. Ruzicka, Measurement of volumetric mass transfer coefficient in bubble columns, ChemEngineering 2 (2018).

P. M. Doran, Bioprocess Engineering Principles, 2nd ed., Elsevier Ltd, 2013.

A. Badino, M. Facciotti, W. Schmidell, Volumetric mass transfer coefficients (k_La) in batch cultivations involving non-newtonian broths, Biotechnology and Bioengineering 18 (1976) 745–790.

H. Blanch, S. Bhavaraju, Non-newtonian fermentation broths: Rheology and mass transfer, Biotechnology and Bioengineering 18 (1976) 745–790.

J. M. T. Vasconcelos, J. M. L. Rodrigues, S. C. P. Orvalho, S. S. Alves, R. L. Mendes,

A. Reis, Effect of contaminants on mass transfer coefficients in bubble column and air lift contactors, Chemical Engineering Science 58 (2003) 1431–1440.

P. Sastaravet, S. Bun, K. Wongwailikhit, N. Chawaloesphonsiya, M. Fujii, P. Painmanakul, Relative effect of additional solid media on bubble hydrodynamics in bubble column and airlift reactors towards mass transfer enhancement, Processes 8 (2020).

M. Bouaifi, G. Hebrard, D. Bastoul, M. Roustan, A comparative study of gas hold-up, bubble size, interfacial area and mass transfer coefficients in stirred gas–liquid reactors and bubble columns, Chemical Engineering and Processing 40 (2001) 97–111.

F. Augier, P. M. Raimundo, Effect of rheology on mass transfer and bubble sizes in a bubble column operated in the heterogeneous regime, The Canadian Journal of Chemical Engineering 99 (2021) 1177–1185.

J. R. Vélez-Cordero, R. Zenit, Bubble cluster formation in shear-thinning inelastic bubbly columns, Journal of Non-Newtonian Fluid Mechanics 166 (2011) 32–41.

J. R. Vélez-Cordero, D. Sámano, R. Zenit, Study of the properties of bubbly flows in borger-type fluids, Journal of Non-Newtonian Fluid Mechanics 175-176 (2012) 1–9.

M. Baird, J. Davidson, Gas absorption by large rising bubbels, Chemical Engineering Science 17 (1962) 87–93.

F. Bischof, M. Sommerfeld, F. Durst, The determination of mass transfer rates from individual small bubbles, Chemical Engineering Science 46 (1991) 3115–3121.

F. Deindoerfer, A. Humphrey, Mass transfer from individual gas bubbles, Industrial and Chemical Engineering 53 (1961) 755–759.

P. Calderbank, A. Lochiel, Mass transfer coefficients, velocities and shapes of carbon dioxide bubbles in free rise through distilled water, Chemical Engineering Science 19 (1964) 485–503.

S. Zieminski, D. Raymond, Experimental study of the behavior of single bubbles, Chemical Engineering Science 23 (1968) 17–28.

S. Hosoda, S. Abe, S. Hosokawa, A. Tomiyama, Mass transfer from a bubble in a vertical pipe, International Journal of Heat and Mass Transfer 69 (2014) 215–222.

J. Aoki, K. Hayashi, A. Tomiyama, Mass transfer from single carbon dioxide bubbles

in contaminated water in a vertical pipe, International Journal of Heat and Mass Transfer 83 (2015) 652–658.

J. M. T. Vasconcelos, S. P. Orvalho, S. S. Alves, Gas-–liquid mass transfer to single bubbles: Effect of surface contamination, AIChE Journal 48 (2002) 1145–1154.

J. E. Olsen, D. Dunnebier, E. Davies, P. Skjetne, J. Morud, Mass transfer between bubbles and seawater, Chemical Engineering Science 161 (2017) 308–315.

E. Cussler, Diffusion, Mass Transfer in Fluid Systems, 2nd ed., Cambridge University Press, 1997.

H. A. Jakobsen, Chemical Reactor Modeling: Multiphase Reactive Flows, 2nd ed., Springer, Berlin, 2014.

W. Whitmand, J. Keats, Rates of absorption and heat transfer between gases and liquids, The Journal of Industrial and Engineering Chemistry 14 (1922) 186–191.

R. Higbie, The rate of absorption of a pure gas into a still liquid during a short time of exposure, Trans. Am. Inst. Chem. Eng. 31 (1935) 365–389.

P. Danckwerts, Significance of liquid-film coefficients in gas adsorption, Engineering and Process Development 43 (1951) 1460–1467.

R. Bird, W. Stewart, E. Lightfoot, Transport phenomena, Wiley, New York (1960).

I. Stamatiou, F. Muller, Determination of mass transfer resistances in trickle bed reactors, Chemical Engineering Journal 377 (2019) 119808.

A. Fick, Ueber diffusion, Annalen der Physik 170 (1855) 59–86. doi:https://doi.org/10.1002/andp.18551700105.

N. Fröessling, Über die verdunstung fallender tropfen, Gerlans Beitage Geophysik 52 (1938) 170–216.

P. H. Calderbank, M. B. Moo-Young, The continuous phase heat and mass-transfer properties of dispersions, Chemical Engineering Science 16 (1961) 39–54.

F. Garner, R. Suckling, Mass transfer from a soluble solid sphere, A.I.Ch.E. Journal 4 (1958) 114–124.

R. Clift, J. Grace, M. Weber, Bubbles, drops, and particles, Academic Press, San Diego (1978). Cited in (Olsen et al., 2017).

H. Brauer, Particle/fluid transport processes, Fortschritte der Verfahrenstechnik (1979).

J. Solsvik, Lagrangian modeling of mass transfer from a single bubble rising in stagnant liquid, Chemical Engineering Science 190 (2018) 370–383.

M. Bouaifi, M. Roustan, Bubble size and mass transfer coefficients in dual- impeller agitated reactors, The Canadian Journal of Chemical Engineering 76 (1998) 390.

S. Alves, C. Maia, J. Vasconcelos, Gas–liquid mass transfer coefficient in stirred tanks interpreted through bubble contamination kinetics, Chemical Engineering and Processing 43 (2004) 823–830.

V. Linek, M. Kordac, T. Moucha, Mechanism of mass transfer from bubbles in dispersions part ii: Mass transfer coefficients in stirred gas–liquid reactor and bubble column, Chemical Engineering and Processing 44 (2005) 121–130.

V. Cappello, C. Plais, C. Vial, F. Augier, Bubble size and liquid-side mass transfer coefficient measurements in aerated stirred tank reactors with non-newtonian liquids, Chemical Engineering Science 211 (2020).

H. Ali, J. Solsvik, Axial distributions of bubble–liquid mass transfer coefficient in laboratory-scale stirred tank with viscous Newtonian and non-Newtonian fluids, Physics of Fluids 32 (2020).

H. Ali, J. Solsvik, Bubble hydrodynamics and mass transfer in stirred tank with non-Newtonian fluids: Scale-up from laboratory to pilot-scale, Physics of Fluids 33 (2021).

I. Kure, H. Jakobsen, J. Solsvik, Interface mass transfer and properties of bubbly flows in a column with Newtonian and non-Newtonian liquids, Chemical Engineering Science 277 (2023) 118828.

K. Koide, S. Yamazoe, S. Harada, Effects of surface-active substances on gas holdup and gas–liquid mass transfer in bubble column, Journal of Chemical Engineering of Japan 18 (1985) 287–292.

M. Motarjemi, G. Jameson, Mass transfer from very small bubbles – the optimum bubble size for aeration, Chemical Engineering Science 33 (1978) 1415–1423.

D. Merker, L. Böhm, M. Oberger, P. Klüfers, M. Kraume, Mass transfer in reactive bubbly flows – a single bubble study, Chemical Engineering Technology 40 (2017) 1391–1399.

S. Alves, J. Vasconcelos, S. Orvalho, Mass transfer to clean bubbles at lowturbulent energy dissipation, Chemical Engineering and Processing 61 (2006) 1334–1337.

J. Leonard, G. Houghton, Mass transfer and velocity of rise phenomena for single bubbles, Chemical Engineering Science 18 (1963) 133–142.

G. Garbarini, C. Tien, Mass transfer from single gas bubbles – a comparative study on experimental methods, The Canadian Journal of Chemical Engineering 47 (1969) 35–41.

I. Kure, H. A. Jakobsen, N. L. Forgia, J. Solsvik, Experimental investigation of single bubbles rising in stagnant liquid: Statistical analysis and image processing, Physics of Fluids 33 (2021).

W. Nock, S. Heaven, C. Banks, Mass transfer and gas–liquid interface properties of single CO_2 bubbles rising in tap water, Chemical Engineering Science 140 (2015) 171–178.

Y. Hori, K. Hayashi, S. Hosokawa, A. Tomiyama, Mass transfer from single carbon-dioxide bubbles in electrolyte aqueous solutions in vertical pipes, International Journal of Heat and Mass Transfer 115 (2017) 663–671.

Y. Bao, J. Jia, S. Tong, Z. Gao, Z. Cai, A review on single bubble gas–liquid mass transfer, Chinese Journal of Chemical Engineering 28 (2020) 2707–2722.

G. Kong, K. Buist, E. Peters, J. Kuipers, Dual emission lif technique for ph and concentration field measurement around a rising bubble, Experimental Thermal and Fluid Science 93 (2018) 186–194.

J. Francois, N. Dietrich, P. Guiraud, A. Cockx, Direct measurement of mass transfer around a single bubble by micro-PLIFI, Chemical Engineering Science 66 (2011) 3328–3338.

T. Saito, M. Toriu, Effects of a bubble and the surrounding liquid motions on the instantaneous mass transfer across the gas–liquid interface, Chemical Engineering Journal 265 (2015) 164–175.

LaVision, Laser induced fluorescence, 2023. Url: https://www.lavision.de/en/techniques/lif-plif/, accessed 2023-08-08.

F. Garcia-Ochoa, E. Gomez, Bioreactor scale-up and oxygen transfer rate in microbial processes: An overview, Biotechnology Advances 27 (2009) 153–176.

P. Gogate, A. Pandit, Survey of measurement for gas—liquid mass transfer coefficient in bioreactors, Biochemical Engineering Journal 4 (1999) 7–15.

V. Linek, P. Benes, V. Vacek, Dynamic pressure method for k_La measurement in large-scale bioreactors, Biotechnology and Bioengineering 33 (1989) 1406–1412.

V. Linek, P. Benes, J. Sinkule, T. Moucha, Non-ideal pressure step method for k_La measurement, Chemical Engineering Science 48 (1993) 1593–1599.

M. Fujasová, V. Linek, T. Moucha, Mass transfer correlations for multiple-impeller gas-–liquid contactors. analysis of the effect of axial dispersion in gas and liquid phases on "local" k_La values measured by the dynamic pressure method in individual stages of the vessel, Chemical Engineering Science 62 (2007) 1650–1669.

F. Garcia-Ochoa, E. Gomez, V. Santos, J. Merchuk, Oxygen uptake rate in microbial processes: An overview, Biochemical Engineering Journal 49 (2010) 289–307.

R. Chhabra, J. Richardson, Non-Newtonian Flow and Applied Rheology, 2nd ed., Springer, 2008.

F. Irgens, Rheology and Non-Newtonian Fluids, Springer, Cham, 2014.

A. de Waele, Viscometry and plastometry, J. Oil Color Chem. Assoc. 6 (1923) 33–88.

W. Ostwald, Ueber die geschwindigkeitsfunktion der viskosität disperser systeme, i. Kolloid Z. 36 (1925) 99–117.

P. Carreau, Rheological equations from molecular network theories (1968). PhD thesis, UW, Madison.

K. Yasuda, Investigation of the analogies between viscometric and linear viscoelastic properties of polystyrene fluids (1979). PhD thesis, MIT, Cambridge.

K. Koide, Y. Orito, Y. Hara, Mass transfer from single bubbles in Newtonian liquids, Chemical Engineering Science 29 (1974) 417–425.

K. Koide, T. Hayashi, K. Sumino, S. Iwamoto, Mass transfer from single bubbles in aqueous solutions of surfactants, Chemical Engineering Science 31 (1976) 963–967.

J. Aoki, Y. Hori, K. Hayashi, S. Hosokawa, A. Tomiyama, Mass transfer from single carbon dioxide bubbles in alcohol aqueous solutions in vertical pipes, International Journal of Heat and Mass Transfer 108 (2017) 1991–2001.

S. Yan, X. Wang, L. Zhu, X. Zhang, Z. Luo, Mechanisms and modeling of bubble dynamic behaviors and mass transfer under gravity: a review, Chemical Engineering Science 277 (2023) 118854.

G. Soligo, A. Roccon, A. Soldati, Turbulent flows with drops and bubbles: what numerical simulations can tell us – free scolar lecture, Journal of Fluids Engineering 143 (2021) 080801.

J. Solsvik, H. Jakobsen, The foundation of the population balance equation: a review, Journal of Dispersion Science and Technology 36 (2015) 510–520.

ISBN 978-82-326-7540-1 (printed ver.)
ISBN 978-82-326-7539-5 (electronic ver.)
ISSN 1503-8181 (printed ver.)
ISSN 2703-8084 (online ver.)

NTNU

Norwegian University of
Science and Technology